Improved hadronic measurements and spectral sums on the lattice

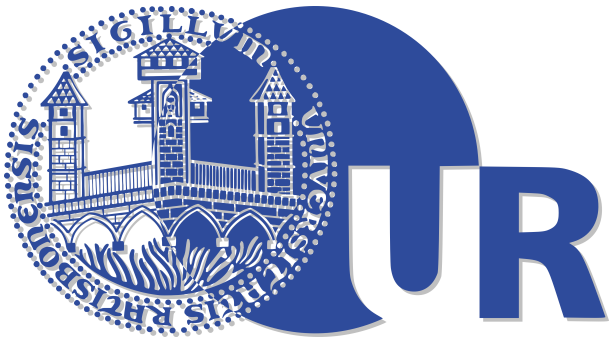

Dissertation

zur Erlangung des Doktorgrades
der Naturwissenschaften (Dr. rer. nat.)
der naturwissenschaftlichen Fakultät II - Physik
der Universität Regensburg

vorgelegt von
Christian Hagen
aus Friesheim

Mai 2008

Promotionsgesuch eingereicht am: 14. Mai 2008

Die Arbeit wurde angeleitet von: Prof. Dr. A. Schäfer

Das Kolloquium fand am 10. Juli 2008 statt.

Prüfungsausschuss:	Vorsitzender:	Prof. Dr. F.J. Gießibl
	1. Gutachter:	Prof. Dr. A. Schäfer
	2. Gutachter:	Prof. Dr. V. Braun
	weiterer Prüfer:	Prof. Dr. M. Brack

Contents

Chapter 1

Introduction

Quantum Chromodynamics, or QCD, is the only candidate theory for describing the strong interaction between elementary particles. It is a non-Abelian gauge theory with gauge group $SU(3)$. Its gauge fields, the gluons, which interact with the color charged quarks, also carry color charges. A consequence of this fact is the self-interaction of gluons which makes QCD a highly non-linear theory. For processes with large momentum transfers, the coupling strength α_S of QCD becomes weak, allowing for a perturbative expansion in this small parameter. The decrease of the coupling strength for high energies is called asymptotic freedom and its discoverers, Gross, Politzer and Wilczek, received the Nobel Prize in 2004. However, at low energies, the coupling grows stronger and perturbation theory is no longer applicable. In that situation other methods have to be used to have a well-defined theoretical description of the strong interaction.

One of these methods[1] is lattice QCD. It provides a systematic approach for evaluating observables in QCD. The lattice discretization of a small hypercubic volume of Euclidean space-time, sometimes called femto-universe, is hereby used as a regularization scheme. It provides an infrared cut-off, because of its finite extent (periodic lattice), and an ultraviolet one, because of the finite lattice spacing. An important advantage of the lattice regularization is the fact that the resulting expressions can be evaluated numerically on computers. The accuracy of such calculations crucially depends on the available computer resources. Fortunately, Moore's law [1] predicts an approximately exponential growth of the performance of computers. For that reason and because of lots of algorithmic advances, lattice QCD simulations have reached a level of accuracy that allows for a sophisticated extraction of important physical quantities from first principles. Such quantities are, for example, the hadron spectrum, form factors and structure functions, and parameters like low energy constants, that are used as input for an effective theoretical description of QCD, called Chiral Perturbation

[1] There are also other methods like QCD sum rules or qualitative descriptions via models.

Theory. It also allows us to study phenomena like spontaneous breaking of chiral symmetry and confinement, that are not yet completely understood.

Outline

We begin in Chapter 2 with a short recapitulation of QCD in the continuum. Afterwards, we discretize the fermionic part of the QCD action. The discretization is not unique. One can exploit this ambiguity and derive a number of different fermion formulations, some of which have smaller discretization effects. However we concentrate on those lattice fermion actions which are used in our studies. In Section 2.3, the gauge fields are introduced, like in the continuum, by requiring local gauge invariance of the fermion action. Also for the lattice gauge action, there exists a certain ambiguity for its formulation, which can be used to reduce discretization effects. After this we address some issues connected to chiral symmetry on the lattice. We end the chapter with an overview of some technical details of lattice QCD simulations.

One of the most important tasks in lattice QCD is the reproduction of hadron spectra from first principles. While it is well understood how to obtain the mass of the lowest lying state in a given hadron channel, the extraction of excited states still is a great challenge. In Chapter 3, we explain how to extract ground state masses of hadrons from two-point correlation functions, which can be calculated on the lattice. For masses of the excited states, however, improved techniques have to be used. For the variational method, which we use in our calculations and describe in Section 3.2, a rich basis of interpolating operators, i.e., lattice discretized operators with the quantum numbers of the desired state, is needed. For that purpose, we consider quarks with different spatial wavefunctions, including some that mimic orbital excitations. We explain how such interpolators can be constructed and then focus on the results of our calculation for ground and excited states of light mesons.

For many applications in lattice QCD ordinary quark propagators, i.e., propagators which connect the quark field at a single location on the lattice to all other sites, are sufficient. But often it is advantageous to have propagators that connect each site on the lattice to all the others, so-called all-to-all propagators. An exact calculation of these objects is not feasible, not even with the latest generation of supercomputers. However, one can at least estimate them. In Chapter 4, we present a new technique, which relies on domain decomposition of the lattice in combination with the Schur complement, to improve such estimates. After deriving the necessary equations, we present a number of possible applications for our method. One of them, the static-light hadron spectrum, we explore in more detail. The results we obtain can be used as a basis for further simulations in the field of B-physics. This area of physics has received great attention, since it

is one of the places where first hints for physics beyond the standard model may be found.

The phenomenology in QCD is governed by two marvelous features: Confinement and spontaneous breaking of chiral symmetry.

One believes that the confinement of colored sources originates from the self-interaction of gluons. This means that colored objects (quarks and gluons) are always arranged in such a way in bound states that the overall state is color neutral, i.e., it is not possible to observe free colored objects. Many mechanisms for confinement have been conjectured but nobody has been able to prove confinement in a mathematical rigorous way.

For massless quarks QCD has a global chiral symmetry, which is, via Noether's theorem, connected to a conserved current. In nature this symmetry is broken in two ways: On the one side, it is broken explicitly by the masses of the quarks. But since the masses of the lightest flavors are much smaller than the typical energy scales in QCD, one would think that at least for them a remnant of the symmetry should have survived. However, this is not the case. Chiral symmetry is not manifest in nature, but is believed to be spontaneously broken. Chiral symmetry breaking has, e.g., the consequence that pions, which are interpreted as the corresponding (Pseudo-)Goldstone bosons, are nearly massless.

Chiral symmetry breaking and confinement are phenomena of QCD at low temperatures. When the temperature is increased above a critical value, the theory becomes deconfined and chiral symmetry is restored. The temperature, at which this phase transition happens, is approximately the same at least for zero baryon density. Therefore, a connection has been conjectured but not yet proven. Since they are both non-perturbative effects, lattice QCD provides a perfect framework to study these phenomena and to probably find a relation between them.

The breaking of chiral symmetry can be studied by looking at the corresponding order parameter, the chiral condensate. It can be expressed in terms of the eigenvalues of the Dirac operator. In QCD without fermions, i.e., in a pure Yang-Mills theory, confinement can be understood as the breaking of the center symmetry of the gauge group. Also for this an order parameter can be formulated, the Polyakov loop. It has been shown that one can express it in terms of the eigenvalues of the Dirac operator, too. Going one step further we define a new order parameter, the dressed Polyakov loop. Also this quantity can be written as a spectral sum of the Dirac eigenvalues. But more important is the fact that it is directly related to the chiral condensate. A numerical investigation of these spectral sums is the subject of Chapter 5. In this way, we at least find a formal connection between the order parameters of chiral symmetry breaking and confinement in pure Yang-Mills theory.

Chapter 2

QCD on the lattice

In this chapter we give an overview of how a continuum gauge theory is discretized on the lattice using the example of QCD. Here we only address the basics. More details can be found in textbooks [2, 3, 4, 5] or the references given in the text.

We start with a brief recapitulation of the continuum action for quarks and gluons, where we address the most important properties of these fields. Then we show how to discretize the fermion fields which live on the *sites* of the lattice. We find that a naive discretization will lead to the so-called *fermion doubling problem*, the appearance of additional unphysical degrees of freedom. To solve this problem Kogut and Susskind proposed to redistribute the fermion degrees of freedom over the elementary hypercube of the lattice[1]. However, this does not remove all unwanted degrees of freedom, since four degenerate fermion flavors, so-called tastes, remain. Another way to solve the doubling problem has been proposed by Wilson [6]. He suggested to extend the naive fermion action by adding another term, the so-called *Wilson term*. Although this term solves the doubler problem, it creates a new one, the loss of chiral symmetry, which is a very important property of QCD. Before we discuss this issue in more detail and show how it can be solved to a certain extent by a redefinition of chiral symmetry, we introduce the gauge fields.

Like in the continuum, the gauge fields are introduced by requiring the theory to be invariant under local gauge transformations. One finds that the gauge fields live naturally on the *links* of the lattice, the lines connecting nearest neighboring sites. From these links one can build so-called *plaquettes*, i.e., a closed loop of links around a square with side length a, which denotes the lattice spacing. These plaquettes are then used to construct a first gauge action on the lattice, the so-called *Wilson gauge action* [7]. This action still has large discretization errors. To reduce these errors one has to improve the Wilson gauge action by taking objects into account, that are more complicated than simple plaquettes. These

[1] For this we follow the derivation given in Reference [4]

improvements lead to the *Iwasaki* [8] and *Lüscher-Weisz gauge action* [9], which are used in our calculations.

Nielson and Ninomiya [10] have shown that it is not possible to retain chiral symmetry in the common form on the lattice (*Nielson-Ninomiya No-Go theorem*). A way out of this problem has been proposed by Ginsparg and Wilson in 1982. They replaced the standard condition for chiral symmetry by the so-called *Ginsparg-Wilson (GW-)equation* [11]. Fermion actions satisfying this equation are called *GW-fermions*. *Overlap fermions* [12, 13] are exact GW-fermions, but using them involves the calculation of the sign function of a huge matrix which is numerically very expensive. Thus, one is content with fermions that fulfill the GW-equation only approximately. These fermions are called *approximate GW-fermions*. A very interesting way of implementing approximate chiral fermions has been proposed by Kaplan [14] and later adapted to the lattice by Shamir [15]. These so-called *domain wall fermions* circumvent the No-Go theorem by separating the chiral modes by an artificial fifth dimension. It has been shown that these fermions are closely connected to overlap fermions and that they become the same in the limit of an infinitely large fifth dimension. Other species of approximate chiral fermions are *Fixed Point (FP-)fermions* [16, 17] and *Chirally Improved (CI-)fermions* [18, 19]. The former are obtained by an iterative blocking procedure which takes into account the renormalization group equation. In this way one starts with the continuum theory and all its symmetries and after many iteration steps one arrives at the desired discretization level. Although this scheme allows to retain a lot of the symmetries of the continuum theory, especially chiral symmetry, it can be shown that the resulting lattice action is not ultra-local anymore. Therefore, one usually uses a parametrized version of the action, which is then numerically much cheaper but only approximate chiral. On the other hand, CI-fermions are obtained by performing an expansion of the Dirac operator in terms of products of link variables. Each class of terms comes with a certain coefficient. They are determined by inserting the expansion into the GW-equation.

In the last section of this chapter we address some technical details of lattice QCD simulations. We start with defining the path integral on the lattice and how it can be used to calculate observables. For that purpose we have to integrate out the fermionic degrees of freedom analytically and perform the integration over the gauge fields using *Monte Carlo methods*. Another important ingredient for our calculations is the quark propagator. The calculation of this quantity is described at the end of this chapter.

2.1 QCD in the continuum

Before we discuss QCD on the lattice we want to give a short review of the continuum theory. For a more detailed discussion, the interested reader is referred to standard textbooks like [20, 21].

In the continuum the Lagrangian density, or short Lagrangian, describing N_f flavors of free fermions[2] is given by

$$\mathcal{L}(x) = \sum_{f=1}^{N_f} \bar{\psi}_f(x)(\gamma_\mu \partial_\mu(x) + m_f)\psi_f(x), \tag{2.1}$$

where m_f are the masses of the fermions which are described by the spinors ψ_f and $\bar{\psi}_f$. To account for the fermionic nature of ψ_f and $\bar{\psi}_f$, they cannot be ordinary numbers but are Grassmann variables (see Appendix C). For QCD, we identify these fields with quarks and antiquarks, respectively. One obtains the complete QCD fermion Lagrangian with interaction by performing a local $SU(N_c)$ rotation of the fermion fields

$$\psi_f(x) \longrightarrow \psi'_f(x) = \Lambda(x)\psi_f(x), \tag{2.2}$$
$$\bar{\psi}_f(x) \longrightarrow \bar{\psi}'_f(x) = \bar{\psi}_f(x)\Lambda^\dagger(x), \tag{2.3}$$

with

$$\Lambda(x) = e^{-\theta_a(x)t_a} \in SU(N_c), \tag{2.4}$$

where t_a are the generators of the $su(N_c)$ algebra, and requiring that the action is invariant under this transformation. This is only possible if we replace the ordinary derivative ∂_μ by a covariant derivative

$$D_\mu(x) = \partial_\mu + iA_\mu(x), \tag{2.5}$$

where the additional term transforms as

$$A_\mu(x) \longrightarrow A'_\mu(x) = \Lambda(x)\left(A_\mu(x) + i\partial_\mu\right)\Lambda^\dagger(x). \tag{2.6}$$

Thus, a simultaneous transformation of ψ_f, $\bar{\psi}_f$, and $A_\mu(x)$ leaves the Lagrangian invariant. The gauge fields $A_\mu(x)$ are then interpreted as new physical degrees of freedom. To describe their dynamics, a gauge invariant kinetic term has to be added to the Lagrangian.

[2]Here and in the following we suppress color and Dirac indices to make formulas easier to read.

The only possible choice for such a term is

$$\begin{aligned}\mathcal{L}_{gauge}(x) &= -\frac{1}{2g^2}\mathrm{Tr}\left[F_{\mu\nu}(x)\,F_{\mu\nu}(x)\right] \\ &= -\frac{1}{4g^2}F^a_{\mu\nu}(x)\,F^a_{\mu\nu}(x),\end{aligned} \tag{2.7}$$

where the field strength tensor is defined as

$$\begin{aligned}F_{\mu\nu}(x) &= -i\left[D_\mu(x), D_\nu(x)\right] \\ &= F^a_{\mu\nu}(x)t^a \\ &= [\partial_\mu \tilde{A}^a_\nu(x) - \partial_\nu \tilde{A}^a_\mu(x) - f^{abc}\tilde{A}^b_\mu(x)\tilde{A}^c_\nu(x))]t^a.\end{aligned} \tag{2.8}$$

The fields $A_\mu(x)$, which have been necessary to maintain gauge invariance of the fermion Lagrangian, are given by

$$A_\mu(x) = \tilde{A}^a_\mu(x)t^a = gA^a_\mu(x)t^a, \tag{2.9}$$

where the A^a_μ are the real-valued gauge fields, the t_a are again the generators of the $su(N_c)$-algebra and g is some gauge coupling parameter. The gauge invariance of $\mathcal{L}_{gauge}$ follows directly from (2.7) because $F_{\mu\nu}$ transforms as

$$F_{\mu\nu}(x) \longrightarrow F'_{\mu\nu}(x) = \Lambda(x)\,F_{\mu\nu}(x)\,\Lambda^{-1}(x) \tag{2.10}$$

and the trace is invariant under cyclic permutations.

The total Lagrangian then reads

$$\mathcal{L}(x) = \sum_{f=1}^{N_f}\bar{\psi}^f(x)(\gamma_\mu D_\mu(x) + m_f)\psi^f(x) - \frac{1}{2g^2}\mathrm{Tr}\left[F_{\mu\nu}(x)\,F_{\mu\nu}(x)\right] \tag{2.11}$$

and the corresponding action is defined as

$$S = \int d^4x\mathcal{L}[\bar{\psi}(x), \psi(x), A(x)]. \tag{2.12}$$

For $N_c = 3$, this action describes the propagation of quarks and gluons and their interaction.

This classical field theory can be quantized in a canonical approach by promoting the fields $\bar{\psi}$,ψ, and A_μ to operators and imposing appropriate commutation relations. A different formalism, which will later also be more suitable for the lattice formulation, is quantization by functional methods. In this formalism the expectation value of an observable $\mathcal{O}$ can be expressed as Feynman path integrals

$$\langle\mathcal{O}[\psi, \bar{\psi}, A]\rangle = \frac{1}{Z}\int [d\psi][d\bar{\psi}][dA]\mathcal{O}[\psi, \bar{\psi}, A]\exp(-S[\bar{\psi}, \psi, A]), \tag{2.13}$$

with the partition function

$$Z = \int [d\psi][d\bar{\psi}][dA] \exp(-S[\bar{\psi}, \psi, A]). \tag{2.14}$$

The integration measures are formally defined as

$$\begin{aligned} [d\psi] &= \prod_{f,c,\alpha} \prod_{x \in \mathbb{R}^4} d\psi_{f\,(\alpha,c)}(x), \\ [d\bar{\psi}] &= \prod_{f,c,\alpha} \prod_{x \in \mathbb{R}^4} d\bar{\psi}_{f\,(\alpha,c)}(x), \\ [dA] &= \prod_{a,\mu} \prod_{x \in \mathbb{R}^4} dA^a_\mu(x). \end{aligned} \tag{2.15}$$

Before we show how this continuum quantum field theory can be reformulated on a lattice, we would like to address an additional symmetry of the fermion Lagrangian which is very important for QCD phenomenology, especially in the low energy sector. In the massless case the fermion Lagrangian is invariant under a $U(N_f)_L \otimes U(N_f)_R$ chiral symmetry. However, due to a quantum anomaly the axial $U(1)_A$ symmetry is broken. Thus, the symmetry is reduced to $SU(N_f)_L \otimes SU(N_f)_R \otimes U(1)_B$, where $U(1)_B$ represents the baryon number conservation. For a single flavor this means that the action is invariant under the chiral transformation:

$$\begin{aligned} \psi(x) &\longrightarrow \psi'(x) = e^{i\epsilon\gamma_5}\psi(x), \\ \bar{\psi}(x) &\longrightarrow \bar{\psi}'(x) = \bar{\psi}(x)e^{i\epsilon\gamma_5}, \end{aligned} \tag{2.16}$$

where ϵ is an arbitrary number. The fermion Lagrangian is invariant, since the anti-commutator

$$\{D(m=0), \gamma_5\} = 0, \tag{2.17}$$

where $D(m)$ is the Dirac operator given by

$$\gamma_\mu D_\mu(x) + m. \tag{2.18}$$

Chiral symmetry and its assumed spontaneous breaking has far-reaching consequences for low-energy QCD. It explains for example the light pion masses. They appear as Pseudo-Goldstone bosons after the spontaneous symmetry breaking. This also allows for a description of QCD in the low-energy regime with an effective theory, known as *Chiral Perturbation Theory (χPT)* [22, 23]. In this theory, physical quantities like hadron masses are expressed in terms of a small expansion parameter given by masses of the pseudo-scalar mesons. For technical reasons, which we will discuss later, lattice QCD simulations usually are restricted to unphysically heavy quarks and thus to large pion masses. Results from χPT then allow to extrapolate lattice QCD results to the physical regime of light pions.

2.2 Fermions on the lattice

In order to calculate observables of a quantum field theory in a mathematically well defined way the theory has to be regularized. In the continuum this can be done, e.g., by dimensional regularization, where one goes to "$4-\epsilon$" dimensions to make the integrals well defined and then at the end takes the limit $\epsilon \to 0$. Other possibilities are Pauli-Villars regularization or a momentum cutoff. On the lattice we use a different approach, which also gives a well defined meaning to the path integral (2.13).

In lattice QCD one replaces the continuous four-dimensional space-time by a hypercubic lattice

$$\Lambda_4 = \{x \mid x = a(n_1, n_2, n_3, n_4)^T, n_\mu = 0, 1, \ldots, L_\mu - 1\}, \tag{2.19}$$

where a is the lattice spacing. On the boundary, we continue the lattice periodically in all four directions and so it becomes a 4-torus. Then the considered quantum field theory (in our case QCD) is translated into a lattice-discretized version. One finds that the fermions of the theory (quarks) are living on the lattice points, the so-called *sites*, while the gauge fields (gluons) are placed on the lines connecting the sites. They are called *links*. The latter follows from gauge invariance and will be subject of Section 2.3. A visualization is given in Figure 2.1.

Like in the continuum, fermions have to be represented by Grassmann variables on the lattice. Therefore, the lattice fermions have to obey periodic boundary conditions in spatial direction but antiperiodic ones in time direction, that means

$$\begin{aligned}\psi(aL_1 + x_1, x_2, x_3, x_4) &= +\psi(x_1, x_2, x_3, x_4),\\ \psi(x_1, x_2, x_3, aL_4 + x_4) &= -\psi(x_1, x_2, x_3, x_4).\end{aligned}$$

The reason for this choice of boundary conditions is that in our simulations we are usually dealing with lattice which have only a finite time direction. The temporal extent of our lattice can be reinterpreted as a inverse temperature. To account for this, antiperiodic boundary conditions must be used. For more detailed discussion we refer to Chapter 18 of Reference [4].

The gauge fields, however, are periodic in all four directions.

2.2.1 Naive discretization

When we now look at (2.1) for a single flavor in the non-interacting case, i.e., $D_\mu \to \partial_\mu$, then we can discretize that action in a naive way by

$$S_{ferm}^{naive} = a^4 \sum_{x,y} \bar{\psi}(x) D_{naive}(x, y) \psi(y) \tag{2.20}$$

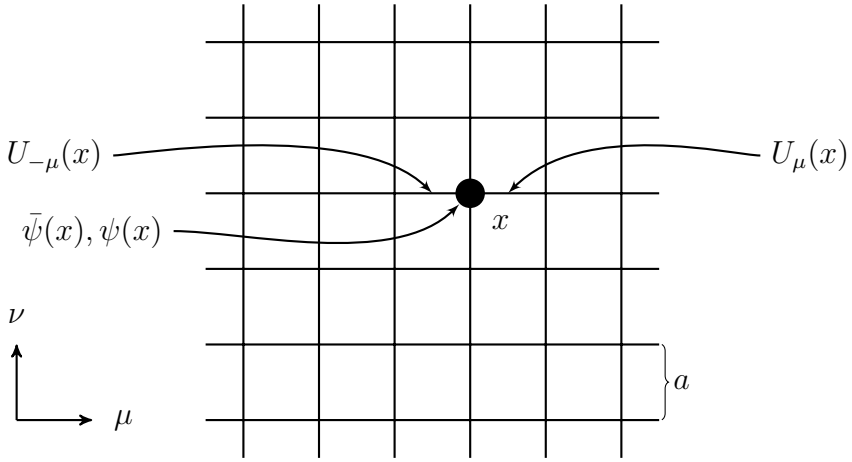

Figure 2.1: On the lattice the fermion fields $\bar{\psi}(x)$ and $\psi(x)$ live on the sites of a hypercubic lattice. The gluonic degrees of freedom, represented by the link variables $U_\mu(x)$, are places on the lines connecting the sites. Here we show the μ-ν-plane of the lattice. The separation of the sites is given by the lattice spacing a.

where the sums run over all lattice points and

$$D_{naive}(x,y) = \sum_{\mu=1}^{4} \gamma_\mu \frac{\delta_{x+a\hat{\mu},y} - \delta_{x-a\hat{\mu},y}}{2a} + m\mathbb{1}\delta_{x,y}. \tag{2.21}$$

is the naive Dirac operator. $\hat{\mu}$ denotes the unit vector in μ-direction. Here we have used the following replacements for our discretization

$$\int d^4x \quad \text{becomes} \quad a^4 \sum_x \qquad \text{and} \tag{2.22}$$

$$\partial_\mu \psi(x) \quad \text{becomes} \quad \frac{\psi(x+a\hat{\mu}) - \psi(x-a\hat{\mu})}{2a}. \tag{2.23}$$

Taking the limit $a \to 0$ we obtain the continuum action again. So everything seems to be fine. But this is not true, because one encounters a problem with this naive discretization, the so-called *fermion doubling problem*.

2.2.2 The fermion doubling problem

The fermion doubling problem becomes apparent when we try to calculate the propagator of our naive Dirac operator in momentum space. We first Fourier

transform the Dirac operator

$$a^8 \sum_{x,y} e^{-ip\cdot x} D_{naive}(x,y) e^{iq\cdot y} \tag{2.24}$$

$$= a^8 \sum_{x} e^{-i(p-q)\cdot x} \left(\sum_{\mu} \gamma_\mu \frac{e^{iq_\mu a} - e^{-iq_\mu a}}{2a} + m\mathbb{1} \right) \tag{2.25}$$

$$= a^4 \, \delta_{p,q} \, V \, \tilde{D}_{naive}(q), \tag{2.26}$$

where $V = L_1 L_2 L_3 L_4$ is the 4-dimensional volume of our lattice and

$$\tilde{D}_{naive}(q) = m\mathbb{1} + \frac{i}{a} \sum_{\mu=1}^{4} \gamma_\mu \sin(q_\mu a). \tag{2.27}$$

When we invert this matrix we obtain the quark propagator in momentum space,

$$\tilde{D}^{-1}_{naive}(q) = \frac{m\mathbb{1} - ia^{-1} \sum_\mu \gamma_\mu \sin(q_\mu a)}{m^2 + a^{-2} \sum_\mu \sin(q_\mu a)^2}, \tag{2.28}$$

which has the correct continuum limit

$$\tilde{D}^{-1}_{naive}(q) = \frac{m\mathbb{1} - ia^{-1} \sum_\mu \gamma_\mu \sin(q_\mu a)}{m^2 + a^{-2} \sum_\mu \sin(q_\mu a)^2} \tag{2.29}$$

$$\xrightarrow{a\to 0} \frac{m\mathbb{1} - i \sum_\mu \gamma_\mu q_\mu}{m^2 + q^2}. \tag{2.30}$$

We also find, that at finite a the propagator has a pole at $q = (0,0,0,0)$, but the problem is that as long as $a \neq 0$ it has many other poles at the edges of the Brillouin zone, namely:

$$\begin{aligned} q = &(\frac{\pi}{a}, 0, 0, 0), (0, \frac{\pi}{a}, 0, 0), \ldots, \\ &(\frac{\pi}{a}, \frac{\pi}{a}, 0, 0), \ldots, \\ &(\frac{\pi}{a}, \frac{\pi}{a}, \frac{\pi}{a}, 0), \ldots, \\ &(\frac{\pi}{a}, \frac{\pi}{a}, \frac{\pi}{a}, \frac{\pi}{a}). \end{aligned} \tag{2.31}$$

These additional 15 poles/fermions are called the *fermion doublers*. That means, for each fermion we want to have, we get 15 additional contributions which are pure lattice artifacts having no continuum analog.

The origin of the fermion doubling problem lies in the use of the (antihermitean) symmetric form of the lattice derivative (2.23). While our lattice spacing is a,

our estimate of the derivative involves twice the lattice scale. By using the right derivative

$$\partial_\mu^R \psi(x) = \frac{\psi(x + a\hat{\mu}) - \psi(x)}{a} \tag{2.32}$$

or left derivative

$$\partial_\mu^L \psi(x) = \frac{\psi(x) - \psi(x - a\hat{\mu})}{a}, \tag{2.33}$$

the fermion doubling problem can be avoided. A detailed analysis however shows that in the presence of interactions the use of the left or right derivative gives rise, for example, to non-covariant contributions to the fermion self energy and vertex function in QED which render the theory non-renormalizable. A detailed discussion of such contributions can be found in [24] and the references therein.

2.2.3 Kogut-Susskind fermions

We have seen in the previous section that a naive discretization leads to unphysical degrees of freedom coming from the corners of the Brillouin zone. The idea of *Kogut-Susskind* or so-called *staggered fermions*[25, 26] is to distribute the fermionic degrees of freedom in such a way over the lattice that the effective lattice spacing for each kind of Grassmann variable is twice the fundamental lattice spacing. This decreases the size of the Brillouin zone and thus removes the doublers. Of coarse this has to be done in such a way that we recover the continuum action in the limit of vanishing lattice spacing with the appropriate number of flavors[3].

The transformation described above can be done by spin-diagonalizing the naively discretized action (2.21). For that purpose, we make a local change of variables

$$\psi(x) = T(x)\chi(x), \tag{2.34}$$

$$\bar{\psi}(x) = \bar{\chi}(x)T^\dagger(x), \tag{2.35}$$

where the transformation matrix $T(x)$ is given by

$$T(x) = \gamma_1^{x_1}\gamma_2^{x_2}\gamma_3^{x_3}\gamma_4^{x_4}. \tag{2.36}$$

It is easy to show that

$$T^\dagger(x)\gamma_\mu T(x + a\hat{\mu}) = \eta_\mu(x)\mathbb{1}, \tag{2.37}$$

where the so-called *staggered phase* $\eta_\mu(x)$ is given by

$$\eta_\mu(x) = (-1)^{x_1+\cdots+x_{\mu-1}} \quad , \quad \eta_1(x) = 1. \tag{2.38}$$

[3]One can show that in d dimensions staggered fermions describe $2^{\frac{d}{2}}$ flavors.

After this transformation the action becomes trivial in the Dirac structure and thus we can restrict ourselves to only one of the terms in the sum over Dirac indices. In this crucial step, we remove twelve of the 16 doublers[4]. The resulting action reads

$$S_{ferm}^{stag} = a^4 \sum_{x,y} \bar{\chi}(x) D^{stag}(x,y) \chi(y), \tag{2.39}$$

where

$$D^{stag} = \frac{1}{2a} \sum_{\mu=1}^{4} \eta_\mu(x) \left[\delta_{x+a\hat{\mu},y} - \delta_{x-a\hat{\mu},y}\right] + m\mathbb{1}\delta_{x,y}, \tag{2.40}$$

is the staggered Dirac operator. It has only one degree of freedom per lattice site, and the only remnants of the Dirac structure are the phases $\eta_\mu(x)$. The four flavors of fermions described by this action are also referred to as *tastes*.

What still needs to be shown is that in the naive continuum limit the staggered action reduces to a free fermion action describing four flavors. For that purpose one needs to combine the χ's within one hypercube in the right way. This reconstruction is shown in Chapter 4.5 of Reference [4].

This kind of formulation has several advantages and disadvantages, which we want to discuss in the following.

The most important advantage is that simulations with staggered fermions are numerically very cheap. In contrast to all other formulations they do not have an explicit Dirac structure which leads to a significant reduction of the number of operations involving the staggered Dirac operator. Staggered fermions, in contrast to Wilson fermions, which we discuss in the next section, preserve a continuous $U(1) \times U(1)$ chiral symmetry. Because of this they can be used to study the spontaneous breaking of chiral symmetry and the associated Goldstone phenomenon on the lattice.

However, staggered fermions have also some drawbacks. As has been stated above they describe four degenerate quark flavors, but for dynamical simulations we want to have $N_f = 2$ or $N_f = 2 + 1$. In order to allow such calculations for staggered fermions so-called "rooting" is used, i.e., in order to create two or one flavors for dynamical simulations one takes the square or fourth root of the staggered Dirac operator, respectively. Up to now there exists no proof that this is a well-defined procedure[5]. Thus all results obtained in this way

[4] In fact all the doublers are removed since that Brillouin zone has been halved in each direction. However, in order to occupy all lattice sites with fermionic degrees of freedom, one has to introduce four different flavors of fermions.

[5] One requirement for the Dirac operator, which one tries to keep is its locality. However, taking the root of a local operator makes it non-local. Apart from this there are probably also other problems concerning the rooting of staggered fermions. For a recent discussion of these issues the interested reader is referred to [27, 28].

are disputable. In addition, this procedure complicates chiral and continuum extrapolations, especially since the order matters, in which the limits are done. One has to first take the continuum limit and then the chiral limit. For technical reasons it is however much easier in lattice QCD simulations to do them the other way round.

The staggered action which has been described is only the simplest one. There exist also more improved ones, for example, the so-called Asqtad action [29, 30, 31].

2.2.4 Wilson fermions

In the last section we have seen that staggered fermions remove doublers by redistributing the fermionic degrees of freedom over the lattice in order to reduce the Brillouin zone. The price we have to pay is that in four dimensions one has to deal with at least four degenerate flavors of fermions, a situation which is not realized in nature.

A different approach to remove the doublers, which we discuss in the following, has been proposed by Wilson [6]. After that we also briefly address an improvement scheme for Wilson fermions, which has been proposed by Sheikholeslami and Wohlert [32] following the improvement scheme of Symanzik.

Wilson fermions

On a lattice with finite lattice spacing a, one is allowed to add higher dimensional terms to the action. For dimensional reasons these additional terms have to be explicitly multiplied by factors of the lattice spacing. In the continuum limit, where a vanishes, also the additional terms vanish and the correct continuum action is retained.

Wilson has exploited this ambiguity by adding a new term to the naive lattice action in order to lift the mass of the doublers by an amount proportional to the inverse lattice spacing and make them vanish in the continuum limit. The fermion action then reads

$$S^W_{ferm} = S^{naive}_{ferm} + r\, S_{new}$$

with the new term

$$\begin{aligned} S_{new} &= a^4 \sum_x \sum_{\mu=1}^{4} \bar{\psi} \frac{\psi(x+a\hat{\mu}) - 2\psi(x) + \psi(x-a\hat{\mu})}{2a} \\ &\rightarrow \frac{a}{2} \int d^4x \bar{\psi}(x) \Delta\psi(x) \stackrel{a\rightarrow 0}{\rightarrow} 0. \end{aligned} \tag{2.41}$$

Usually one chooses $r = 1$. Then the Dirac operator of the Wilson action is given by

$$D^W(x,y) = (m + 4/a)\mathbb{1}\delta_{x,y} - \frac{1}{2a}\sum_{\mu=\pm1}^{\pm4}(\mathbb{1} + \gamma_\mu)\delta_{x+a\hat{\mu},y}, \tag{2.42}$$

where we define

$$\gamma_{-\mu} := -\gamma_\mu. \tag{2.43}$$

Often one introduces a shorthand notation after rescaling the fermion field by a factor $\sqrt{m + 4/a}$. It reads

$$D^W = \mathbb{1} - \kappa H, \tag{2.44}$$

where the hopping parameter κ is related to the bare quark mass via $\kappa = \frac{1}{2(am+4)}$ and H is the hopping term.

We now repeat the same steps as we have done for the naive ansatz, i.e., we Fourier transform D_W. We obtain

$$\tilde{D}^W(p,q) = a^4\delta_{p,q}V\tilde{D}^W(q), \tag{2.45}$$

with

$$\tilde{D}^W(q) = \frac{i}{a}\sum_{\mu=1}^{4}\gamma_\mu \sin(aq_\mu) + \frac{1}{a}\sum_{\mu=1}^{4}\mathbb{1}(1 - \cos(aq_\mu)) + m\mathbb{1}. \tag{2.46}$$

When we expand (2.46) for small q_μ we get $\tilde{D}_W = m\mathbb{1} + i\not{q} + O(a)$, as it should be. But the result for the doublers has changed. In the limit $q_\mu \to \frac{\pi}{a}$, for l components μ, we obtain now

$$\tilde{D}^W(q) \quad = \quad \frac{2l}{a} + O(1) \quad \stackrel{a\to0}{\longrightarrow} \quad \infty. \tag{2.47}$$

This means, that in the continuum limit the doublers become infinitely heavy, and thus can no longer contribute to the dynamics. However, although we have removed the unwanted degrees of freedom in this way, we have to pay a prize for it: The loss of chiral symmetry.

In Equation (2.42) one immediately finds, that Wilson fermions explicitly break exact chiral symmetry even for vanishing quark mass due to the local part of the Wilson term. This has serious consequences, both technically and conceptionally, for simulations with Wilson fermions: Fluctuations of the low-lying eigenvalues of the Dirac operator lead to a huge increase of the numerical efforts of simulations since they can render matrix-vector equations containing the Dirac operator

ill-defined and thus unsolvable. This does not only occur when propagators are calculated but also during the generation of configurations with a Hybrid Monte-Carlo algorithm, leading to so-called exceptional configurations. Even more problematic is the recovery of chiral symmetry in the continuum limit. This can only be achieved by fine tuning the bare quark mass due to additive mass renormalization [33]. Because of the later problem, one usually does not consider the bare quark mass but instead defines

$$m = m_0 - m_c, \tag{2.48}$$

with the critical quark mass m_c. Its value, which is of $O(g_0^2/a)$, has to be determined for each simulation separately and is defined as the quark mass where the mass of the pseudoscalar meson vanishes.

Clover improvement

In 1985, Sheikholeslami and Wohlert [32] have generalized the Symanzik improvement program to lattice fermion fields. Similar to Lüscher and Weisz, they have added higher dimensional operators to the naive lattice fermion action. Through symmetry considerations and by using the equations of motion this set of operators is reduced to only one. It consists of the already known Wilson term with a natural choice of $r = 1$ and an additional term which contains the field strength tensor. The resulting clover-Wilson action then reads

$$S_{ferm}^{SW} = S_{ferm}^{W} + c_{SW}\frac{i}{4}a^5 \sum_x \bar{\psi}(x)\sigma_{\mu\nu}F_{\mu\nu}\psi(x). \tag{2.49}$$

For $F_{\mu\nu}$ one usually chooses the simplest lattice realization which is given by

$$F_{\mu\nu}(x) = \frac{1}{8a^2}\left[Q_{\mu\nu}(x) - Q_{\nu\mu}(x)\right], \tag{2.50}$$

with

$$\begin{aligned} Q_{\mu\nu}(x) = {} & U_\mu(x)U_\nu(x+a\hat{\mu})U_{-\mu}(x+a\hat{\mu}+a\hat{\nu})U_{-\nu}(x+a\hat{\nu}) \\ & + U_\mu(x)U_{-\nu}(x+a\hat{\mu})U_{-\mu}(x+a\hat{\mu}-a\hat{\nu})U_\nu(x-a\hat{\nu}) \\ & + U_{-\mu}(x)U_{-\nu}(x-a\mu)U_\mu(x-a\mu-a\nu)U_\nu(x-a\nu) \\ & + U_{-\mu}(x)U_\nu(x-a\mu)U_\mu(x-a\mu+a\nu)U_{-\nu}(x+a\nu), \end{aligned} \tag{2.51}$$

where the $U_\mu(x)$ are link variables which we introduce in the next section. The field strength tensor can be depicted as in Fig 2.2, which roughly resembles four-leaved clovers. This is also the reason for the name of the action. After this improvement lattice artifacts are reduced to $O(a^2)$. Nevertheless, additive mass renormalization is still necessary.

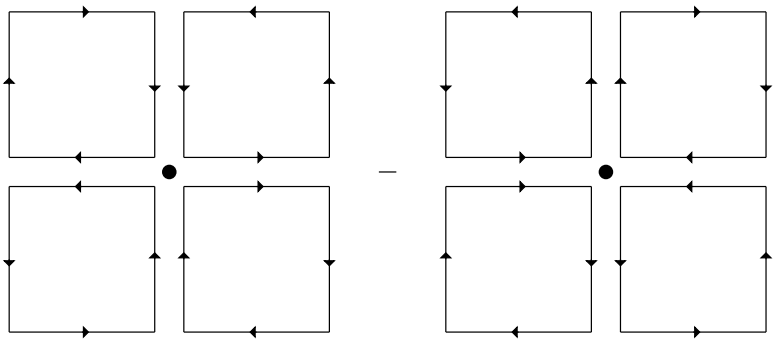

Figure 2.2: Picture of the simplest formulation of the field strength tensor on the lattice. The clover-like shapes are responsible for the name of the clover improved Wilson action.

Within perturbation theory the coefficient of the clover term is given by

$$c_{SW} = 1 + O(g_0^2). \tag{2.52}$$

It can, however, also be calculated non-perturbatively, e.g., within the framework of the Schrödinger functional [34, 35, 36, 37].

A very general introduction to non-perturbative improvement can be found in Ref. [38].

2.3 Gauge fields on the lattice

2.3.1 Coupling to the gauge fields

In Section 2.1, we have derived the interaction between fermions and gauge fields by requiring the fermion Lagrangian and thus the action to be invariant under a local gauge transformation of the fermion fields. We follow the same procedure on the lattice. This means that the fermion action

$$S = a^4 \sum_{x,y} \bar{\psi}(x) D(x,y) \psi(y) \tag{2.53}$$

again has to be invariant under the transformation

$$\psi(x) \longrightarrow \psi'(x) = \Lambda(x)\psi(x), \tag{2.54}$$

$$\bar{\psi}(x) \longrightarrow \bar{\psi}'(x) = \bar{\psi}(x)\Lambda^\dagger(x). \tag{2.55}$$

Therefore, the Dirac operator must transform as

$$D(x,y) \longrightarrow D'(x,y) = \Lambda(x) D(x,y) \Lambda^\dagger(y). \tag{2.56}$$

This means that the Dirac operator has to connect points x and y in a gauge covariant way. For that purpose, the concept of parallel transporters [7, 39], usually called Wilson lines, is used. In the continuum, they are given by

$$U(x,y) = \mathcal{P} \exp\left(i \int_x^y dz_\mu A_\mu(z) \right), \tag{2.57}$$

where $\mathcal{P}$ denotes path ordering. After discretizing this expression on a lattice with lattice spacing a we obtain

$$U_\mu(x) := U(x, x + a\hat{\mu}) \approx \exp(iaA_\mu(x)) \in SU(3), \tag{2.58}$$

where $A_\mu(x)$ are the continuum gauge fields. One immediately sees that the object $U_\mu(x)$ lives on the link connecting the site x to its nearest neighbor in direction μ. We therefore refer to them in the following as *link variables*, or simply just links. They represent the gauge field degrees of freedom on the lattice.

Using these results the covariant Wilson Dirac operator, for example, then reads

$$D^W(x,y) = (m + 4/a)\mathbb{1}\delta_{x,y} - \frac{1}{2a} \sum_{\mu=\pm 1}^{\pm 4} (\mathbb{1} + \gamma_\mu) U_\mu(x) \delta_{x+a\hat{\mu},y}, \tag{2.59}$$

where we have used the convention

$$U_{-\mu}(x) = U_\mu(x - a\hat{\mu})^\dagger \tag{2.60}$$

Another important object we want to define here is the *plaquette*

$$U^{pl}_{\mu\nu}(x) = U_\mu(x) U_\nu(x + a\hat{\mu}) U_{-\mu}(x + a\hat{\mu} + a\hat{\nu}) U_{-\nu}(x + a\hat{\nu}). \tag{2.61}$$

It represents the closed loop around a square with side length a.

2.3.2 Wilson gauge action

We can use the plaquette to construct the *Wilson gauge action* [7]

$$S_{gauge} = a^4 \beta \sum_x \sum_{1 \le \mu < \nu \le 4} \left\{ 1 - \frac{1}{N_c} Re[\mathrm{Tr}(U^{pl}_{\mu\nu}(x))] \right\}, \tag{2.62}$$

where $Re[X]$ denotes the real part of X and $N_c = 3$ in the case of QCD. The invariance of this action under a local gauge transformation $\Lambda(x)$ is shown very easily. The link variables are defined to transform as

$$U'_\mu(x) = \Lambda(x) U_\mu(x) \Lambda^{-1}(x + a\hat{\mu}). \tag{2.63}$$

By using Equation (2.60) and the invariance of the trace under cyclic permutations, one can immediately see that S_{gauge} is invariant.

Now we want to show that Equation (2.62) has the right continuum limit. Therefore, we expand the links to first order in a. This results in

$$S_{gauge} = -\frac{\beta}{4N_c} \int d^4x \mathrm{Tr}[F_{\mu\nu}(x)\, F_{\mu\nu}(x)] + O(a^2). \tag{2.64}$$

We compare this to (2.7)and find

$$\beta = \frac{2N_c}{g^2}. \tag{2.65}$$

Another thing we see is that Equation (2.62) still has discretization errors of order $O(a^2)$. To reduce these errors, we have to include more complicated objects than simple plaquettes in the construction of the gauge action. Two examples of improved gauge actions are described in the following section.

2.3.3 Improved gauge actions

We have seen that the Wilson gauge action still has quite large discretization errors. In the following we want to discuss two improvement schemes to reduce these errors.

The first one is based on the transformation behavior of lattice actions under the renormalization group. By an iterative blocking of the lattice action until a fixed point of the renormalization group flow is reached, we obtain an improved gauge action with reduced discretization errors.

A different improvement scheme was proposed by Symanzik [40, 41]. He has shown that a Lagrangian field theory on a lattice is equivalent order by order in g and a to a local effective Lagrangian in the continuum. This allows one to improve lattice actions order by order by adding higher dimensional operators with appropriately chosen coefficients. As an example for this improvement scheme we want to discuss the Lüscher-Weisz gauge action. As we have seen in Section 2.2.4, this improvement scheme can be also applied to lattice fermion actions.

Iwasaki gauge action

The Iwasaki gauge action is a renormalization group improved $SU(3)$ gauge action

$$S_G^{RG} = \frac{\beta}{6} \left(c_0 \sum_{x,\mu<\nu} U^{pl}_{\mu\nu}(x) + c_1 \sum_{x,\mu,\nu} U^{rt}_{\mu\nu}(x) \right), \tag{2.66}$$

with

$$U^{rt}_{\mu\nu}(x) = U_\mu(x)U_\nu(x+a\hat{\mu})U_\nu(x+a\hat{\mu}+a\hat{\nu}) \\ U_{-\mu}(x+a\hat{\mu}+2a\hat{\nu})U_{-\nu}(n+2a\hat{\nu})U_{-\nu}(n+a\hat{\nu}). \tag{2.67}$$

The coefficient $c_1 = -0.331$ of the rectangular loops $U^{rt}_{\mu\nu}$ is fixed by an approximate renormalization analysis [8], while $c_0 = 1 - 8c_1 = 3.648$ is determined by the normalization condition, which defines the bare coupling $\beta = 6/g^2$. From the point of view of Symanzik improvement, which we want to discuss next, the leading discretization error of this action are $O(a^2)$, the same as for Wilson gauge action. However, in a number of calculations, some improvement has been found.

Lüscher-Weisz gauge action

Following Symanzik's improvement program, Lüscher and Weisz [9, 42] have been able to derive an improved lattice gauge action. This is achieved by adding rectangular and "parallelogram" terms with appropriately chosen coefficients to the Wilson gauge action. The resulting action reads

$$\begin{aligned} S^{LW}_G = \beta_0 \sum_S \left(1 - \frac{1}{N} Re\mathrm{Tr} U^{pl}_{\mu\nu}\right) \\ + \beta_1 \sum_R \left(1 - \frac{1}{N} Re\mathrm{Tr} U^{rt}_{\mu\nu}\right) \\ + \beta_2 \sum_P \left(1 - \frac{1}{N} Re\mathrm{Tr} U^{pg}_{\mu\nu\rho}\right), \end{aligned} \tag{2.68}$$

where the additional "parallelogram" terms are given by

$$U^{pg}_{\mu\nu\rho}(x) = U_\mu(x)U_\nu(x+a\hat{\mu})U_\rho(x+a\hat{\mu}+a\hat{\nu}) \\ U_{-\mu}(x+a\hat{\mu}+a\hat{\nu}+a\hat{\rho})U_{-\nu}(x+a\hat{\nu}+a\hat{\rho})U_{-\rho}(x+a\hat{\rho}). \tag{2.69}$$

A comparison with perturbative calculated quantities however has shown that the bare coupling which is incorporated in β and β_0 for standard Wilson and improved Lüscher-Weisz action, respectively, is not a meaningful expansion parameter. A more useful parameter can be obtained after a redefinition of the coupling constant within the framework of tadpole improved perturbation theory [43]. When combining these considerations with the Lüscher-Weisz gauge action the coefficients are given in terms of the expectation value of the plaquette

variable [44]:

$$u_0^4 = \frac{1}{3} Re \mathrm{Tr} \langle U^{pl} \rangle, \tag{2.70}$$

$$\alpha = -\frac{\ln u_0^4}{3.06839}, \tag{2.71}$$

$$\beta_1 = -\frac{\beta_0}{20 u_0^2}(1 + 0.4805\alpha), \tag{2.72}$$

$$\beta_2 = -\frac{\beta_0}{u_0^2} 0.03325\alpha. \tag{2.73}$$

The variable α is the redefined coupling constant in tadpole improved perturbation theory. The remaining discretization errors are order $O(g^2 a^2)$.

At this point we want to mention a technical detail of the tadpole improved Lüscher-Weisz gauge action. Since for a given β_0 the others are given in term of an expectation value of the plaquette variable, these coefficients can be calculated iteratively within a lattice calculation: For a given β_0 chose an arbitrary value for u_0. With these values create an ensemble of configurations. Measure u_0 on this ensemble and recalculate the coefficients. Iterate this until the coefficients converge.

2.4 Chiral symmetry on the lattice

2.4.1 Nielson-Ninomiya No-Go theorem

In Section 2.2.4, the fermion doublers have been removed by adding the Wilson term to the naive action. This term, however, explicitly breaks chiral symmetry. In a general theorem, Nielsen and Ninomiya [10] have proven, that for a translational invariant free fermion lattice action the following properties cannot be realized simultaneously[6]:

1. Locality, i.e., $|D(x,y)| < C \exp(-\alpha|x-y|)$.
2. Exact chiral symmetry: $D\gamma_5 + \gamma_5 D = 0$, for $m = 0$.
3. No doublers.
4. Correct continuum limit.

This means that on the lattice at least one of the above conditions has to be violated.

[6] In fact, this is only a corollary of the Nielsen-Ninomiya theorem.

The proof of the theorem is very simple. Consider a general chirally symmetric and translationally invariant free fermion lattice action. It can be written as

$$S = \sum_{x,y,\mu} \bar{\psi}(x)\gamma_\mu K_\mu(x-y)\psi(y), \tag{2.74}$$

with a local kernel $K_\mu(x-y)$. After a Fourier transformation the kernel in momentum space, $K_\mu(p)$, is necessarily a regular function of the Brillouin zone, i.e., there are no poles. Since the action is real and translationally invariant, $K_\mu(p)$ also is real and must be a periodic function in p. Zeros in $K_\mu(p)$ then correspond to poles of the propagator and thus to fermions, both physical ones and doublers. Here, the Nielsen-Ninomiya theorem comes into play. It states that a real-valued, regular, and periodic function $K_\mu(p)$ necessarily vanishes at more than only a single point. In one dimension this is obvious. A regular periodic function with at least one zero is positive on one side to the zero and negative on the other side. Thus, the function necessarily must go through zero again in order to satisfies periodicity. In higher dimensions the prove is similar. In d dimensions, the zeros lie on d closed $(d-1)$-dimensional surfaces. These surfaces cannot intersect only in a single point, if the d-dimensional space is periodic in each direction. Thus, there is at least one doubler.

2.4.2 Ginsparg-Wilson equation

One way to evade the No-Go theorem has been proposed in 1982 by Ginsparg and Wilson [11]. They have replaced the continuum version of chiral symmetry by

$$D\gamma_5 + \gamma_5 D = a2D\gamma_5 D \qquad \text{for } m = 0. \tag{2.75}$$

This relation implies that chiral symmetry is violated explicitly but in a minimal way, which is sufficient to evade the No-Go theorem. Later, Lüscher [45] proposed a modification of the standard chiral transformations

$$\begin{aligned} \psi &\to \psi + \delta\psi = (1 + i\epsilon\gamma_5(1-aD))\,\psi, \\ \bar{\psi} &\to \bar{\psi} + \delta\bar{\psi} = \bar{\psi}\,(1 + i\epsilon(1-aD)\gamma_5)\,, \end{aligned} \tag{2.76}$$

where D is a lattice Dirac operator which depends on the gauge fields and we have considered only a single flavor. In the continuum limit these transformations reduce to the usual ones (2.16). We now use these relations to perform a transformation of a fermion action with the Dirac operator D.

$$\bar{\psi}D\psi \to \bar{\psi}\,(1 + i\epsilon(1-aD)\gamma_5)\,D\,(1 + i\epsilon\gamma_5(1-aD))\,\psi \tag{2.77}$$

$$= \bar{\psi}D\psi + i\epsilon\bar{\psi}\,(D\gamma_5 + \gamma_5 D - a2D\gamma_5 D)\,\psi + O(\epsilon^2) \tag{2.78}$$

$$= \bar{\psi}D\psi + O(\epsilon^2), \tag{2.79}$$

where in the last step we have assumed that the operator D fulfills the GW-relation. Thus, the GW-relation is intimately connected to chiral symmetry on the lattice. To make the distinction to continuum chiral symmetry, fermions fulfilling this relation should not be called chiral, although they are in a certain sense, but be referred to as GW-fermions.

It is a non-trivial task to explicitly construct an operator compatible with the GW-equation. That is also the reason why it has been forgotten for a long time. In 1997, Hasenfratz [16] has rediscovered the relation and a short time later an exact solution of the GW-relation has been proposed by Neuberger [46, 47], called the overlap operator [12, 13].

2.4.3 Overlap fermions

The massless overlap operator is given by

$$D_{ov} = \frac{1}{2}\left(\mathbb{1} + \gamma_5 \mathrm{sgn}(\gamma_5 D)\right) \tag{2.80}$$

where sgn is the matrix sign function and the kernel operator D can be an arbitrary Dirac operator without doublers, for example, the Wilson Dirac operator. One can easily show that this operator describes GW-fermions by inserting it into Equation (2.75) and using $[\mathrm{sgn}(\gamma_5 D)]^2 = \mathbb{1}$. Although this operator has a very simple form, it is numerically very expensive to exactly evaluate the sign function of $\gamma_5 D$, because it requires to compute the sign function of its eigenvalues. For this, the matrix has to be diagonalized, which is only possible for very small lattices. Fortunately, in most lattice QCD simulations only the Dirac operator multiplied by a vector is needed. For this operation one can use approximation schemes which express the matrix sign function applied to a vector in terms of the kernel operator times the vector. To improve such methods one often uses deflation techniques[48], i.e., the lowest lying eigenvalues of the kernel operator are treated exactly and only for the higher lying ones an approximation scheme is used. For a variety of these methods, including several 5-D approximation schemes, the interested reader is referred to [49, 50, 51, 52, 53] and the references therein.

Although these schemes have greatly improved in recent years, they are still very expensive. Only when running the latest algorithms on supercomputers, which are currently developed (see for example [54]), simulations with dynamical overlap fermions in a physically interesting regime are about to become possible. Until then, fermion actions satisfying the GW-relation only approximately are a good alternative. One example for such an action, which we have extensively used in our simulations, will be discussed in detail in the following section.

2.4.4 CI-Fermions

The Chirally Improved (CI)-Dirac operator [18, 19] is an approximate solution of the GW-equation. One[7] starts by writing down a general expansion of a Dirac operator in terms of the 16 generators of the Clifford algebra Γ_α and all gauge transporters connecting a given point x with a point y:

$$D(x,y) = \sum_{\alpha=1}^{16} \Gamma_\alpha \sum_{p \in \mathcal{P}_{x,y}} c_p^\alpha \prod_{l \in p} U_l. \tag{2.81}$$

Each of the terms comes with a coefficient c_p^α, where α labels the generator of the Clifford algebra and p individual paths in the set of all paths $\mathcal{P}_{x,y}$ connecting x and y. One then imposes symmetries which should be fulfilled by any well-behaved Dirac operator, i.e., invariance under translation and rotation, invariance under charge conjugation and parity transformation, and of course γ_5-hermiticity. These considerations allow us to rewrite Equation (2.81) as

$$\begin{aligned}
D(x,y) = \mathbb{1} & \left(s_1 + s_2 \sum_{l_1} \langle l_1 \rangle + s_3 \sum_{l_2 \neq l_1} \langle l_1, l_2 \rangle + s_4 \sum_{l_1} \langle l_1, l_1 \rangle + \dots \right) \\
& + \sum_{\mu} \gamma_\mu \sum_{l_1 = \pm\mu} \mathrm{sgn}(l_1) \left(v_1 \langle l_1 \rangle + v_2 \sum_{l_2 \neq \pm\mu} [\langle l_1, l_2 \rangle + \langle l_2, l_1 \rangle] + v_3 \langle l_1, l_1 \rangle + \dots \right) \\
& + \sum_{\mu<\nu} \gamma_\mu \gamma_\nu \sum_{\substack{l_1=\pm\mu \\ l_2=\pm\nu}} \mathrm{sgn}(l_1 l_2) \sum_{i,j=1}^{2} \epsilon_{i,j} \left(t_1 \langle l_i, l_j \rangle + \dots \right) \\
& + \sum_{\mu<\nu<\rho} \gamma_\mu \gamma_\nu \gamma_\rho \sum_{\substack{l_1=\pm\mu \\ l_2=\pm\nu \\ l_3=\pm\rho}} \mathrm{sgn}(l_1 l_2 l_3) \sum_{i,j,k=1}^{3} \epsilon_{ijk} \left(a_1 \langle l_i, l_j, l_k \rangle + \dots \right) \\
& + \gamma_5 \sum_{l_\mu = \pm 1}^{\pm 4} \mathrm{sgn}(l_1 l_2 l_3 l_4) \sum_{i,j,k,o=1}^{4} \epsilon_{ijko} \left(p_1 \langle l_i, l_j, l_k, l_o \rangle + \dots \right),
\end{aligned} \tag{2.82}$$

where

$$\langle \mu_1, \mu_2, \dots, \mu_k \rangle = \delta_{m, n+\sum_k \hat{\mu}_k} U_{\mu_1}(n) U_{\mu_2}(n+\hat{\mu}_1) \cdots U_{\mu_k}(m-\hat{\mu}_k) \tag{2.83}$$

denotes path ordered products of gauge links, tracing a path from n to m, in which the k-th hop is in direction μ_k. In the above formula, which is depicted in Figure 2.3, we group the terms according to their transformation behavior in Dirac space, i.e., scalar, vector, tensor, axialvector, and pseudoscalar, and show only the shortest terms in each of these channels.

[7] For this section we follow the derivation of the CI-operator which has been compiled in Reference [55].

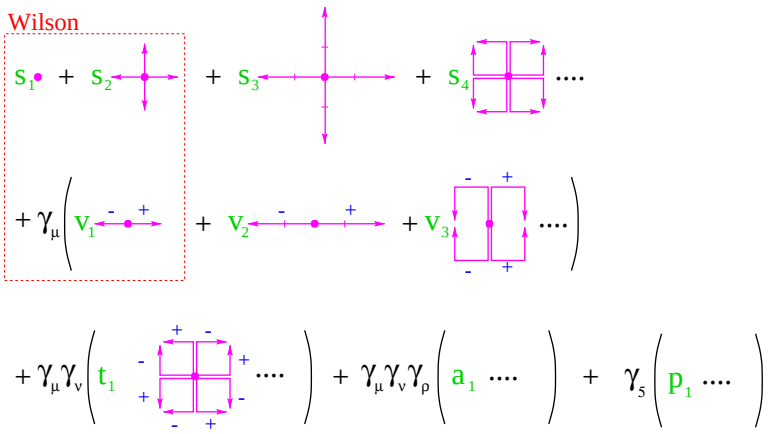

Figure 2.3: Graphical interpretation of the leading terms of Equation (2.82). The parts, which correspond to the Wilson Dirac operator, are marked separately.

To determine the coefficients s_i, v_i, a_i, t_i, and p_i, we insert the full expansion into the GW-relation. The resulting set of coupled equations reads

$$
\begin{aligned}
0 &= -2s_1 + s_1^2 + 8s_2^2 + 18s_3^2 + 8v_1^2 + 96v_2^2 + 8v_3^2 + 48t_1^2 + 192a_1^2 + 384p_1^2 + \dots \\
0 &= -2s_2 + 2s_1s_2 + 12s_2s_3 + 2s_2s_4 + 12v_1v_2 + 2v_1v_3 + \dots \\
0 &= -2s_3 + 2s_1s_3 + s_2^2 + 4s_3^2 + 2s_3s_4 + 4v_2^2 + 2v_2v_3 + \dots \\
0 &= -2s_4 + 2s_1s_4 + s_2^2 + 6s_3^2 - v_1^2 - 6t_1^2 - 24a_1^2 - 48p_1^2 + \dots \\
0 &= -s_2v_1 - 4s_3v_2 - 2s_4v_2 - s_3v_3 - v_3t_1 - 4v_2t_1 + \dots \\
0 &= -2t_1 + 2s_1t_1 - 2s_4t_1 - v_1^2 - 4v_2^2 - 2v_2v_3 - 4t_1^2 + 8v_1a_1 - 8a_1^2 + 16t_1p_1 + \dots \\
0 &= -s_2a_1 + v_2t_1 - v_3p_1 + \dots \\
0 &= -v_2t_1 + \dots \\
0 &= -s_2a_1 - 2v_2p_1 + \dots \\
0 &= -2s_2a_1 + 2v_2t_1 - 4v_2p_1 + \dots \\
0 &= -2p_1 + 2s_1p_1 - 2s_4p_1 - 2v_1a_1 + t_1^2 + \dots
\end{aligned}
\tag{2.84}
$$

These equations are still equivalent to the GW-relation but each of them contains a series of infinitely many terms. Since locality is one of the conditions, which are fulfilled by GW-fermions, the coefficients should decrease at least exponentially with the length of the associated paths. Therefore, a well-justified approximation is to remove paths with largest length from the above set of equations. This renders the resulting Dirac operator ultra-local which makes it attractive for numerical simulations.

Furthermore, we have to ensure the correct continuum limit for massless fermions

$$\tilde{D}(p) = i\gamma_\mu p_\mu + O(p^2), \tag{2.85}$$

which yields two more equations:

$$\begin{aligned} 0 &= s_1 + 8s_2 + 48s_3 + 8s_4 + \dots \\ 1 &= 2v_1 + 24v_2 + 4v_3 + \dots . \end{aligned} \tag{2.86}$$

In principle, the first equation guarantees that any term vanishes which breaks chiral symmetry explicitly. Since we have performed an approximation by truncating the expansions in (2.84), we have reintroduced such a term. The effects of that term, however, should become smaller and smaller as we relax the approximation. It turns out that terms with rather long paths have to be included to obtain a decent continuum limit. Therefore, in [19] an improvement has been proposed which modifies (2.86) to

$$\begin{aligned} 0 &= s_1 + 2s_2 z_s + 48s_3 z_s^2 + 8s_4 z_s^2 + \dots \\ 1 &= 2v_1 z_v + 24v_2 z_v^2 + 4v_3 z_v^2 + \dots . \end{aligned} \tag{2.87}$$

The real parameters $z_s(\beta)$ for scalar and $z_v(\beta)$ for vector terms are then determined in lattice simulations for each values β such that the equations above are fulfilled as good as possible. The equations (2.84) coming from the GW-relation are not altered. This allows one to optimize the properties of the Chirally Improved operator without sacrificing chiral symmetry.

In a last step, $O(a)$-discretization effects are removed. Exact solutions to the GW-relation have this property already. Since we have performed an approximation, we reinsert tree level improvement by requiring

$$s_2 + 12s_3 + 4s_4 + \dots = 4t_1 + 32t_2 + 16t_3 + \dots \tag{2.88}$$

This is similar to choosing $c_{SW} = 1$ for Clover-Wilson fermions.

The level of approximation has been tuned to obtain fermions with good chirality while keeping the computational overhead relatively small. The coefficients used in our calculations are summarized in Appendix G.

2.5 Lattice QCD simulations

2.5.1 Path integral on the lattice

After discretizing fermion and gauge action, we rewrite the path integral (2.13) in terms of the new degrees of freedom $\bar{\psi}$, ψ and U_μ. The expectation value for an observable on the lattice then reads

$$\langle \mathcal{O}[\psi, \bar{\psi}, U] \rangle = \frac{1}{Z} \int [d\psi]\, [d\bar{\psi}]\, [dU]\, \mathcal{O}[\psi, \bar{\psi}, U]\, e^{-S_{QCD}}, \tag{2.89}$$

with the partition function

$$Z = \int [d\psi]\,[d\bar{\psi}]\,[dU]\; e^{-S_{QCD}} \tag{2.90}$$

On the lattice the integral measures are well-defined:

$$[d\psi] = \prod_x \prod_{\alpha,a,f} d\psi^f_{\alpha,a}(x), \tag{2.91}$$

$$[d\bar{\psi}] = \prod_x \prod_{\alpha,a,f} d\bar{\psi}^f_{\alpha,a}(x), \tag{2.92}$$

$$[dU] = \prod_x \prod_{\mu} dU_\mu(x). \tag{2.93}$$

In the last expression each individual measure $dU_\mu(x)$ is the measure invariant under group transformations, the so-called *Haar measure*.

The path integral can be separated into a fermionic and a gauge field part

$$\langle \mathcal{O}[\psi,\bar{\psi},U]\rangle = \frac{1}{Z}\int [dU]\, e^{-S_{gauge}[U]}\,(\int [d\psi]\,[d\bar{\psi}]\, e^{-S_{ferm}[\psi,\bar{\psi},U]}\,\mathcal{O}[\psi,\bar{\psi},U]), \tag{2.94}$$

$$= \langle \mathcal{O}[U]\rangle_U, \tag{2.95}$$

where we have used the fact, that S_{QCD} can be split into a fermionic part which depends on the fermion fields as well as on the gauge variables and a gauge part which depends only on the gauge fields. We first evaluate the integral over the fermion fields which can be done analytically, as we show in the next section. The result, which we denote with $\mathcal{O}[U]$, then depends only on the gauge fields. This result must then be integrated over all possible sets of gauge links, each one weighted with $\exp(-S_{gauge})$. This step, denoted by $\langle \ldots \rangle_U$, has to be done numerically, using Monte Carlo methods (see Section 2.5.3).

2.5.2 Fermion contractions and quenched approximation

We want to show how the integration of the fermion fields in Equation (2.94) is done. For this we consider only the integral over the fermions in the numerator (2.94)[8]

$$\int [d\psi]\,[d\bar{\psi}]\, e^{-S_{ferm}[\psi,\bar{\psi},U]}\mathcal{O}[\psi,\bar{\psi},U].$$

[8]The term in the denominator of (2.94) can be treated the same way by setting $\mathcal{O} = \mathbb{1}$.

To solve this integral we use the results of Appendix C. We can then rewrite it as

$$\int [d\psi]\,[d\bar{\psi}]\,e^{-S_{ferm}[\psi,\bar{\psi},U]}\mathcal{O}[\psi,\bar{\psi},U] = \mathcal{O}[\frac{\partial}{\partial\bar{\eta}},\frac{\partial}{\partial\eta},U]\,Z[\eta,\bar{\eta}]\Big|_{\substack{\eta=0\\ \bar{\eta}=0}}$$
$$= \left(\prod_f \det D_f[U]\right)\,\mathcal{O}[D_f^{-1},U], \qquad (2.96)$$

where f labels the different quark flavors. $\mathcal{O}[D_f^{-1},U]$ now is a functional of the quark propagators D_f^{-1}. Here Z is the generating functional of the fermions[9]

$$Z[\eta,\bar{\eta}] = \int \prod_k^{N_f}(d\psi_k\,d\bar{\psi}_k)\,\exp\left\{-\sum_f \bar{\psi}_f\,D\,\psi_f + \bar{\psi}_f\eta_f + \bar{\eta}_f\psi_f\right\}. \qquad (2.97)$$

So the integral in (2.94) simplifies to

$$\langle\mathcal{O}[U]\rangle_U = \frac{1}{Z}\int [dU]\,e^{-S_{gauge}[U]}\,(\prod_f \det D_f[U])\,\mathcal{O}[D_f^{-1},U]. \qquad (2.98)$$

In the literature, this integration of the fermion fields is often referred to as *fermion contraction*.

A tremendous simplification of the numerical effort is obtained by using the *quenched approximation*, where one sets

$$\det D_f[U] \equiv const. \qquad (2.99)$$

The reason for this is that $D_f[U]$ is a very large matrix ($12V \times 12V$) which makes it very expensive to calculate the determinant. The quenched approximation neglects all internal quark loops. Of course, at first sight, this is not a very good approximation since essential features of the theory are being removed. Nevertheless it works surprisingly well[10]. This simplifies the integral to

$$\langle\mathcal{O}[U]\rangle_U = \frac{1}{Z}\int [dU]\,e^{-S_{gauge}[U]}\,O[D^{-1},U]. \qquad (2.100)$$

On the other hand to correctly describe nature, the full expression with determinants must be used. The dominant contributions come from the light flavors up and down, which are approximately mass degenerate, but also the strange

[9] For further details see Section 7.1 of [21].

[10] Often there are corrections of not more than 10%-20%, depending upon the quantity one is looking at.

quark should be taken into account. Thus, in dynamical simulations one usually neglects the contributions of the heaviest quark flavors. Therefore, in lattice QCD one refers to $N_f = 2$ when two degenerate light quark flavors, up and down, are considered and to $N_f = 2 + 1$ when also a heavier strange quark is included. For the algorithms used in dynamical simulations it is essential to express the determinants in Equation (2.98) as bosonic Gaussian integral

$$\det D[U] = \frac{1}{\det(D^{-1}[U])} = \int [d\phi][d\bar{\phi}] \exp(\bar{\phi} D^{-1}[U]\phi). \tag{2.101}$$

The bosonic variables $\bar{\phi}, \phi$ have the same indices as the Grassmann valued variables $\bar{\psi}, \psi$ but are ordinary complex numbers. Thus, they are referred to as *pseudofermions*. The path integral can then be written as

$$\langle \mathcal{O}[U] \rangle_U = \frac{1}{Z} \int [dU][d\phi][d\bar{\phi}]\, e^{-S_{eff}[U,\bar{\phi},\phi]}\ \mathcal{O}[D_f^{-1}, U], \tag{2.102}$$

with the effective action

$$S_{eff}[U, \bar{\phi}, \phi] = S_{gauge}[U] + \sum_{f=1}^{N_f} \bar{\phi}_f D_f^{-1}[U] \phi_f. \tag{2.103}$$

At first sight it seems as if nothing is gained by this. However, from a numerical point of view the complex numbers $\bar{\phi}, \phi$ can be treated much easier than Grassmann variables.

2.5.3 Monte-Carlo methods

The evaluation of the integrals over gauge fields, both for full QCD, Equation (2.98), and in the quenched approximation, Equation (2.100), cannot be done with standard numerical methods. The reason is the high dimensionality of the integral[11]. The only feasible way is to use *Monte Carlo methods*.

The idea behind these methods is that integration measures can be identified with probabilities. One evaluates the integral by sampling a number of random points from a probability distribution given by the integral measure. In the case of Equation (2.98) this means that one generates a set of gauge configurations $(\{U\}_1, \{U\}_2, \ldots, \{U\}_N)$ from the distribution

$$P(\{U\}, \bar{\phi}, \phi)[dU][d\phi][d\bar{\phi}] = \frac{1}{Z} e^{-S_{eff}[U,\bar{\phi},\phi]}. \tag{2.104}$$

[11] For a lattice with 10^4 sites, there are 4×10^4 link variables. Each of them can be parametrized by 8 real parameters in the case of $SU(3)$, hence 320000 integrations are to be done. If one evaluates each integrand at only 10 points, this means that the full integral over the gauge fields has to be approximated by a sum over 10^{320000} terms (Example taken from [4]).

The integrand is then evaluated at these points and the integral can be approximately obtained by a sample average

$$\bar{\mathcal{O}}_N = \frac{1}{N} \sum_{i=1}^{N} \mathcal{O}[\{U\}_i]. \tag{2.105}$$

The law of large numbers then guarantees that the sample average becomes the expectation value $\langle \mathcal{O} \rangle_U$ in the limit of infinitely many configurations

$$\langle \mathcal{O} \rangle_U = \lim_{N \to \infty} \bar{\mathcal{O}}_N. \tag{2.106}$$

However, for a finite number of configurations all results are affected by a statistical error and effects of the finite autocorrelation times become important. Therefore, a decent error analysis has to be carried out (see Appendix F).

Creating gauge configurations is the first step which has to be done for any lattice QCD calculation. Over the years many algorithm have been developed for this task. For dynamical fermions the state of the art is the so-called *Hybrid Monte Carlo* (HMC) algorithm [56].

An introduction to these algorithms can be found in standard textbooks [3, 4] and in [57]. The latter focuses on dynamical simulations and discusses in detail the HMC algorithm. There exist also several improvement ideas for these algorithms, like better integrators [58], Hasenbusch acceleration[59], multi-Pseudo-fermion methods, timescale separation à la Sexton-Weingarten [60] and initial guess techniques [61]. However, a detailed discussion of all these techniques is beyond the scope of this thesis.

2.5.4 Calculation of the quark propagator

The last missing ingredient for lattice QCD simulations is the calculation of quark propagators. For observables with fermions we find that after fermion contraction an observable contains once or several times the inverse of the Dirac operator, D^{-1}, which we call full quark propagator in the following. An exact computation of this quantity is only feasible for very small lattices since this would require up to n^3 operations where $n = 12 \times V$ is the the rank of the Dirac operator. Fortunately, for many observables and for the generation of configurations with dynamical fermions the full propagator is not necessary, and it is enough to compute the propagator applied to a source vector b. This means that one needs to find the solution x of the linear equation

$$D[U]x = b. \tag{2.107}$$

The solution can then be computed using iterative methods, like conjugate gradient [62, 63], which give an exact solution after n iterations. However, in practical

simulations with a finite numerical precision it is usually enough to obtain x to a certain relative accuracy

$$\frac{||Dx - b||}{||b||} < \epsilon. \tag{2.108}$$

When the desired precision is reached the iterations are stopped. The speed with which these iterative methods converge are dictated by the condition number $\kappa(D)$ of the matrix which is defined as

$$\kappa(D) = \left| \frac{\lambda_{max}}{\lambda_{min}} \right|, \tag{2.109}$$

where λ_{max} and λ_{min} are the largest and smallest eigenvalue of the matrix D, respectively. For small quark masses the lowest eigenvalue of D is nearly zero, resulting in a very large condition number. Then many more iterations are necessary in order to reach a given relative accuracy. This is also the reason why lattice QCD simulations are usually restricted to rather large quark masses.

Chapter 3

Spectroscopy on the lattice

The calculation of hadron masses is one of the central subjects in lattice QCD. The main reason is that lattice QCD gives us the opportunity to study the spectrum of hadrons from first principles. The results of such calculations can then be compared to experiment. This allows us to not only learn something about experimentally known resonances but also enables us to predict masses and properties of states which have not yet been measured. Since the precise nature of hadron resonances is unknown, lattice QCD calculations provide an indispensable contribution for their understanding.

However, this is not the only reason why hadron masses are the subject of very intensive studies in lattice QCD. A second, more technical reason is that we want to know to what extent our calculations are affected by systematic errors, which are usually connected to limited computer resources[1]. The calculation of hadron masses gives us the possibility to study these systematics of our formulation by allowing us to compare our results with precise experimental measurements.

While it is well understood how to extract the mass of the ground state in a given channel, a clean extraction of the masses of excited states in a lattice QCD calculation is still a challenge. One of the main difficulties is the fact that excited states only appear as subleading exponentials in Euclidean two-point correlation functions. To extract them, a variety of approaches have been tried. They reach from brute-force multi-exponential fits to more sophisticated techniques using Bayesian priors methods [64, 65, 66] and "NMR-inspired blackbox" methods [67]. Even evolutionary algorithms have been considered [68]. A number of these methods have been studied and compared in [69]. However, the probably most powerful technique is the variational approach [70, 71, 72], which is also the

[1]Usual systematic errors are finite volume, quenching, and discretization effects. However, effects coming from fermions which explicitly break chiral symmetry on the lattice can also be crucial. Certainly, the quenched approximation leads to significant systematic effects.

method we use for our studies. In this approach one studies not only a single correlator but a whole matrix of correlation functions.

To access the crucial information contained in this matrix, a rich enough basis of interpolating operators (i.e., products of creation and annihilation operators with the correct quantum numbers, which approximate the hadron on the lattice) has to be constructed.

In the following sections we show how to extract meson masses from Euclidean two-point correlation functions and discuss the variational method which should allow us to also obtain the masses of excited mesons. In Section 3.3, we describe how we construct a rich basis of interpolators by using different spatial wave-functions for the quark fields. This approach of using differently smeared quark sources has already been very successful in previous quenched studies and we bank on those results.

Then, after briefly describing the details of the simulations, we present our findings for the meson spectrum. We give reasons for our choices of fit ranges and the expressions we have used for the chiral extrapolations. In this study we have concentrated on the pseudoscalar, vector, scalar, and axialvector channel of the meson spectrum. In the end we summarize our results for these channels and compare them to experimental values.

Our final studies, which are to be published [73] and are based on CP-PACS field configurations for $N_f = 2$ clover Wilson fermions, are complemented by similar studies on quenched lattices with Chirally Improved fermions [74].

3.1 Meson two-point functions and their interpretation in Hilbert space

In this section we show how to obtain ground state masses of hadrons from Euclidean two-point correlation functions. We restrict ourselves to mesons, the generalization to baryons is straightforward.

The energies of mesons can be obtained from the time dependence of two-point correlation functions of the type

$$\langle M(\vec{p},t)M^\dagger(\vec{p},0)\rangle, \tag{3.1}$$

where $M^\dagger(\vec{p},0)$ and $M(\vec{p},t)$ are meson operators which create and annihilate mesons with momentum $\vec{p}$ at time 0 and t, respectively. We evaluate the two-

point function on the lattice by formulating it as path integral

$$\langle M(\vec{p},t)M^\dagger(\vec{p},0)\rangle = \frac{1}{Z}\int D[\psi,\bar{\psi},U]e^{-S[\psi,\bar{\psi},U]}M[\psi,\bar{\psi},U;\vec{p},t]M^\dagger[\psi,\bar{\psi},U;\vec{p},0] \tag{3.2}$$

$$= \left\langle M[\psi,\bar{\psi},U;\vec{p},t]\ M^\dagger[\psi,\bar{\psi},U;\vec{p},0]\right\rangle . \tag{3.3}$$

The meson operators are expressed in terms of the basic degrees of freedom, ψ,$\bar{\psi}$ and U. It is not possible to do this in such a way that the resulting operators are describing the corresponding meson states exactly. Also we are working on a discretized space-time lattice and therefore certain continuum symmetries are broken. Finally, the exact many-particle wavefunctions of the mesons are not known anyway and are also scale dependent. Therefore, one uses *interpolators*, which are of much simpler structure, but have the same quantum numbers as the desired mesons, to create the correct states (see below). After this rewriting, the methods described in Sections 2.5.2 and 2.5.3 are applicable.

On the other hand, we can reinterpret the two-point functions in Hilbert space by using the transfer matrix formalism. For that purpose we write Equation (3.1) as

$$\langle M(\vec{p},t)M^\dagger(\vec{p},0)\rangle = \frac{1}{Z}Tr\left[e^{-(T-t)\hat{H}}Me^{-t\hat{H}}M^\dagger\right], \tag{3.4}$$

with the normalization factor

$$Z = Tr\left[e^{-T\hat{H}}\right]. \tag{3.5}$$

The expression in Equation (3.4) is the trace of four operators (read from right to left): The operator $M^\dagger$, which creates a meson; then a time evolution operator in Euclidean space-time evolving the state for a certain time t; then the operator M, which annihilates the meson again; and finally another Euclidean time evolution operator evolving everything again for a time $T-t$, expressing the fact that we are working on a lattice with finite temporal extent T.

We may write out the trace explicitly as a sum over a complete set of eigenstates of the Hamiltonian and insert another complete set between the time evolution operator $e^{-t\hat{H}}$ and the operator M. We should stress that the eigenstates of the Hamiltonian, along with its eigenvalues, are yet unknown. Then one obtains:

$$\begin{aligned}\frac{1}{Z}Tr\left[e^{-(T-t)\hat{H}}Me^{-t\hat{H}}M^\dagger\right] &= \frac{\sum_{n,m}e^{-(T-t)E_m}\langle m|M|n\rangle e^{-tE_n}\langle n|M^\dagger|m\rangle}{\sum_m e^{-TE_m}} \\ &= \frac{\sum_{n,m}\langle m|M|n\rangle\langle n|M^\dagger|m\rangle e^{-t\Delta E_n}e^{-(T-t)\Delta E_m}}{1+e^{-T\Delta E_1}+e^{-T\Delta E_2}+\cdots},\end{aligned} \tag{3.6}$$

where

$$\Delta E_n = E_n - E_0 \tag{3.7}$$

is the energy difference between the state $|n\rangle$ and the vacuum state $|0\rangle$. For notational convenience, from now on we denote this energy difference simply as E_n.

We then expand Equation (3.6) in the lowest lying meson states $|M\rangle$, $|M'\rangle$, ... which have overlap with the meson operators M and $M^\dagger$. We thus obtain

$$\begin{aligned}\langle M(\vec{p},t)M^\dagger(\vec{p},0)\rangle &= \sum_{m,n}\langle m|M|n\rangle\langle n|M^\dagger|m\rangle e^{-tE_n}e^{-(T-t)E_m} \\ &= \langle 0|M|M\rangle\langle M|M^\dagger|0\rangle e^{-tE_M} + \langle\overline{M}|M|0\rangle\langle 0|M^\dagger|\overline{M}\rangle e^{-(T-t)E_M} \\ &+\langle 0|M|M'\rangle\langle M'|M^\dagger|0\rangle e^{-tE_{M'}} + \langle\overline{M'}|M|0\rangle\langle 0|M^\dagger|\overline{M'}\rangle e^{-(T-t)E_{M'}} + \dots \\ &= |\langle 0|M|M\rangle|^2\left(e^{-tE_M}+e^{-(T-t)E_M}\right)\times \\ &\quad\left\{1+\frac{|\langle 0|M|M'\rangle|^2}{|\langle 0|M|M\rangle|^2}\frac{e^{-tE_{M'}}+e^{-(T-t)E_{M'}}}{e^{-tE_M}+e^{-(T-t)E_M}}+\dots\right\},\end{aligned} \tag{3.8}$$

where we have assumed that the time extent T of our lattice is large enough such that the exponentials in the denominator of (3.6) are sufficiently suppressed and that for mesons one can choose $M = M^\dagger$.

When we focus on the leading term, which should dominate in the regions where $0 \ll t \ll T$, we can rewrite the above equation to obtain

$$\langle M(\vec{p},t)M^\dagger(\vec{p},0)\rangle = |\langle 0|M|M\rangle|^2 e^{-\frac{E_M T}{2}}\left(e^{(\frac{T}{2}-t)E_M}+e^{-(\frac{T}{2}-t)E_M}\right)\{1+\dots\} \tag{3.9}$$

$$= A\cosh((\frac{T}{2}-t)E_M)\{1+\dots\}, \tag{3.10}$$

with $A = 2Z^{-1}|\langle 0|M|M\rangle|^2 e^{-\frac{E_M T}{2}}$. Equation (3.10) is the function to which our lattice results for meson two-point functions is fitted in order to extract ground state energies.

For spectroscopic calculations we are only interested in the rest masses of the mesons. Therefore, we use the operators $M^\dagger(\vec{x}=0,t=0)$ in real space to create hadrons of arbitrary momentum and an operator $M(\vec{p},t)$ in momentum space with definite momentum $\vec{p}$ to annihilate it. This means that the hadron is annihilated only if it has the momentum $\vec{p}$ and only then it does contribute to the correlator[2]. To project the operator to definite momentum, we use the Fourier transformation

$$M(\vec{p},t) = L^{-\frac{3}{2}}\sum_{\vec{x}} e^{-i\vec{p}\vec{x}}M(\vec{x},t). \tag{3.11}$$

[2]Alternatively, one can Fourier transform both operators and then shift one of the spatial indices to zero by using translational invariance, which however is only recovered in the full ensemble average.

After this projection the energies in Equation (3.10) turn into rest masses. We can extract them by fitting the results of our lattice calculations with Equation (3.10). Since in our calculations we are only interested in the rest masses, projection to zero momentum is implicitly assumed in the following.

3.2 Variational method

In the previous section, we explained how one can extract the mass of the ground state from two-point functions. But we are not only interested in the ground states. We also want to obtain the spectrum of excited states. One possibility is trying to extract the masses of the excited states by a multi-exponential fit to the form

$$\langle M(t)M^\dagger(t=0)\rangle = \sum_n \langle 0|M|n\rangle\langle n|M^\dagger|0\rangle e^{-M_n t}, \tag{3.12}$$

in order to get the excited masses M_n, $n > 1$ from the sub-leading exponential contributions of the two-point functions, where for the moment we have neglected the contribution coming from the term which goes like $\exp[-(T-t)M_n]$. The disadvantage of this brute-force approach is that all the information has to be extracted from a single correlator. In the unfortunate case that the overlap of the operator M with an excited state is small, it becomes difficult to extract the mass of that state.

Another method to obtain the excited states spectrum, the method we use to get our results, is the variational method, which was first proposed by Michael [70] and later refined by Lüscher and Wolff [71].

The idea is to use several different operators M_i, $i = 1, \ldots, N$ which all have the quantum numbers of the desired meson state. One then uses these operators to compute all possible combinations of two-point functions, which are then collected in a so-called *cross-correlation matrix*

$$C_{ij}(t) = \langle M_i(t)M_j^\dagger(t=0)\rangle \tag{3.13}$$

$$= \sum_n \langle 0|M_i|n\rangle\langle n|M_j^\dagger|0\rangle e^{-M_n t}. \tag{3.14}$$

According to Michael, Lüscher and Wolff, we can then extract the eigenvalues λ of this matrix by solving the generalized eigenvalue problem

$$C(t)\,\vec{v}^{(k)} = \lambda^{(k)}(t,t_0)C(t_0)\,\vec{v}^{(k)}. \tag{3.15}$$

The so obtained eigenvalues then behave like

$$\lambda^{(k)}(t,t_0) \propto e^{-M_k(t-t_0)}[1 + O(e^{-(t-t_0)\Delta M_k})], \tag{3.16}$$

where M_k is the mass of the k-th state and ΔM_k is the difference to the mass closest to M_k. Certainly, we cannot rely anymore on the symmetry property that $M_i = M_j^\dagger$ for $i \neq j$. However, one can show that the entries of the cross-correlation matrix are either hyperbolic cosines or sines, depending on the relative time reversal symmetry, and for most operators they are purely real or imaginary. Therefore, after solving the eigenvalue problem, the $\lambda^{(k)}$ in general mix cosh- and sinh-like behavior. Thus, we can only fit exponentials to the eigenvalues in the time regions, where cosh and sinh are both approximately exponential.

Additional information is provided by the eigenvectors $\vec{v}^{(k)}$. Their components are the weights for the different operators, reflecting the size of the contribution of a certain M_i to the considered eigenvalue. Thus, one can view them as a "fingerprint" of the corresponding state. We use this knowledge to improve the reliability of the time intervals in which we fit the obtained eigenvalues.

Although we present in this chapter results of dynamical simulations, we nevertheless want to mention another remarkable property of the variational method. In quenched and partially quenched simulations (i.e., simulations where the sea quarks are heavier than the valence quarks) it is possible that additional, unphysical states appear in the meson spectrum. In [72], we have shown that these so-called ghost contributions, which enter with a modified time dependence, can be isolated in individual eigenvalues (up to higher order corrections) and thus are separated from the proper physical states. The corresponding eigenvalues can then be excluded from the analysis.

3.3 Construction of meson interpolators

The key to a successful application of the variational method is the choice of basis interpolators M_i, $i = 1, \ldots, N$. They should be linearly independent and orthogonal if possible. At the same time they should have good overlap with the desired states such that the matrix elements in Equation (3.14) are large. And of course, they should be numerically cheap and easy to implement.

In the case of flavor non-singlet mesons[3], local interpolators have the form

$$M(\vec{x}, t) = \bar{u}(\vec{x}, t)\, \Gamma\, d(\vec{x}, t), \tag{3.17}$$

where Γ is an element of the Clifford algebra. For meson spectroscopy it is well known that different Dirac structures Γ can be used to construct meson interpolators with the same quantum numbers. For example, using either γ_i or

[3]Flavor singlet mesons are very difficult to treat on the lattice, since so-called disconnected contributions to the correlation function have to be calculated. These contributions are numerically very expensive and non-standard techniques must be used. We come back to this issue in Section 4.1.2.

$\gamma_4\gamma_i$ gives an interpolator with the quantum numbers $J^{PC} = 1^{--}$. However, it is also well known (see, e.g.,[75, 76]) that using correlators with different Dirac structures alone does not provide a sufficient basis to obtain good overlap with excited states. To construct better meson interpolators we follow a strategy which already has been very successful in our previous quenched studies of the excited hadron spectrum [77, 78], however with some modifications.

In our previous studies we have used two extended sources obtained by a different amount of Jacobi smearing [79, 80]. In a lattice spectroscopy calculation the hadron correlators are built from quark propagators D^{-1} acting on a source b (see Section 2.5.4),

$$\sum_{\vec{y},\rho,c} D^{-1}(\vec{x},t \mid \vec{y},0)_{\substack{\beta \\ b}}{}^{\substack{\rho \\ c}} \; b^{(\alpha,a)}(\vec{y},0)_{\substack{\rho \\ c}} \; . \tag{3.18}$$

If the source is point-like, i.e., $b = P$, with

$$P^{(\alpha,a)}(\vec{y},0)_{\substack{\rho \\ c}} = \delta_{\vec{y},\vec{0}} \; \delta_{\rho\,\alpha} \; \delta_{c\,a} \; , \tag{3.19}$$

then the two quarks in Equation (3.17) both sit on the same lattice site. Certainly this is not a very physical assumption, because hadrons are extended objects.

The idea of Jacobi smearing is to create an extended source by iteratively applying the hopping part of the Wilson term within the timeslice of the source:

$$\begin{aligned} b^{(\alpha,a)} &= S_J \; P^{(\alpha,a)} \quad , \quad S_J = \sum_{n=0}^{N} \kappa^n \, H^n \; , \\ H(\vec{x},\vec{y}\,) &= \sum_{i=1}^{3} \Big[\, U_i(\vec{x}\,) \, \delta_{\vec{x}+\hat{i},\vec{y}} + U_{-i}(\vec{x}\,) \, \delta_{\vec{x}-\hat{i},\vec{y}} \Big] \, . \end{aligned} \tag{3.20}$$

Applying the inverse Dirac operator as shown in (3.18) connects the source at timeslice zero to the lattice points at timeslice t. There, an extended sink may be created by again applying the smearing operator S_J. This smearing technique has two free parameters: the number of smearing steps N and the positive real parameter κ which is proportional to the probability of "hopping" to a neighboring spatial site.

In our previous studies the sources have been tuned in such a way that they resemble Gaussians with different spatial widths which, in appropriate combinations, represent the wavefunctions of ground and excited states of a spherical harmonic oscillator model of hadrons. The idea was to construct interpolators from these Gaussians and insert them into the variational approach to open the possibility of a radial excitation.

For simulations using configurations with dynamical fermions, however, it turns out that such a tuning is very difficult, since the effective lattice spacing depends

P	Point source at $x = 0$
n	Narrow source obtained with Jacobi smearing $N = 8, \kappa = 0.22$
L	Covariant 3D lattice Laplacian $\Delta^{(3)}$ applied to narrow source
∇_x	Covariant derivative ∇_x applied to narrow source
∇_y	Covariant derivative ∇_y applied to narrow source
∇_z	Covariant derivative ∇_z applied to narrow source

Table 3.1: List of quark sources.

on the sea quark masses. Therefore, the matching to the Gaussians should be done separately for each sea quark mass.

Ignoring these fine tuning problems, we decide to use only a single Jacobi smeared source. We refer to it as *narrow source* in the following and denote it with n. In order to still allow for a radial excitation we also include a source, where we apply a three-dimensional gauge covariant lattice Laplacian

$$\Delta^{(3)}(\vec{x},\vec{y}\,) = \sum_{i=1}^{3} \left(U_i(\vec{x})\,\delta_{\vec{x}+\hat{i},\vec{y}} + U_{-i}(\vec{x})\,\delta_{\vec{x}-\hat{i},\vec{y}} - 2\delta_{\vec{x},\vec{y}} \right) \tag{3.21}$$

onto the narrow smeared sources. This one we call *Laplacian source* and denote it with L. Since both Jacobi smearing and the Laplacian are scalar operators, these do not change the quantum numbers of our generic meson interpolators.

To enlarge our interpolator basis even more and also to explore the possibility of orbital excitations we augment our quark sources by additional *derivative sources*. These are generated by applying a symmetric covariant lattice derivative

$$\nabla_i(\vec{x},\vec{y}\,) = \frac{1}{2} \left(U_i(\vec{x})\,\delta_{\vec{x}+\hat{i},\vec{y}} - U_{-i}(\vec{x})\,\delta_{\vec{x}-\hat{i},\vec{y}} \right) \tag{3.22}$$

in the appropriate direction onto the narrow smeared source. However, the resulting derivative sources, denoted by ∇_x, ∇_y, and ∇_z, have to be combined appropriately with Dirac gamma matrices, to construct meson interpolators with the desired quantum numbers. The necessary group theory for this can be found in [81]. Although the derivative sources allow us to construct operators for spin-2 and spin-3 mesons, we focus in this study on the spin-0 and spin-1 sectors, and try to build a rich basis for these mesons.

Finally, we also incorporate point-like sources, denoted by P, to our set of smearings. Although the resulting interpolators have smaller overlap with the states, these additional sources give us the opportunity to not only extract the masses of the mesons, but also to compute local matrix elements which can be related to the decay constants of the mesons.

A complete list of our smearings is given in Table 3.1.

3.4 Simulation details

Before presenting the results of our calculations, we briefly summarize the technical details of our simulations.

We calculate our meson two-point correlation functions on configurations with two flavors of dynamical quarks. These configurations have been generated by the CP-PACS Collaboration[82, 83] using clover Wilson fermions with mean field improved clover coefficients and the renormalization group improved Iwasaki gauge action. For our calculation only every fifth configuration in each ensemble has been used to reduce effects coming from finite autocorrelation times and at the same time save computational resources.

In Appendix H, we summarize the details of the configurations used in our simulations. For each lattice size, there exist four ensembles with different sea quark masses. The values κ_{sea} have been chosen in such a way that the ratio m_{PS}/m_V is approximately the same for the different lattice sizes. More information about these configurations, especially how they have been generated, can be found in [82, 83].

We use the smearings which we have discussed in the previous section to construct a number of interpolating fields for pseudoscalar, scalar, vector, and axialvector mesons. As the normalization timeslice for the variational method we choose $t_0 = 1$.

For our simulations we use CHROMA [84], a lattice QCD software package developed by USQCD. Our computations are performed on our small version of the QCDOC [85] in Regensburg.

3.5 Results

In the following we present the results of our calculations.

For our analysis we take advantage of several symmetries of the cross-correlation matrix. We find that the matrices $C(t)$ are real and symmetric within error bars. Therefore, we symmetrize them by replacing $C_{ij}(t)$ by $(C_{ij}(t)+C_{ji}(t))/2$. We can increase our statistics even further by taking into account the contributions which are proportional to $\exp[-(T-t)M_n]$. As we have already mentioned in Section 3.2, one can show that there are two types of entries in the cross-correlation matrices: One which is proportional to a hyperbolic sine and one proportional to a hyperbolic cosine. However, the absolute values of both types of entries have the same functional dependence, namely $\exp[-tM_n]$, except for the region near $T/2$. When solving the generalized eigenvalue problem, this is also the region where both types differ and we have to avoid this region in our fits. Therefore,

after the symmetrization, we replace $C(t)$ by $(|C(t)| + |C(T-t)|)/2$ and use the result in the variational method.

The eigenvalues, we obtain from the generalized eigenvalue problem (3.15), can then be fitted to the function

$$\lambda^{(k)}(t, t_0) \quad = \quad Ae^{-M_k(t-t_0)}. \tag{3.23}$$

To determine fit ranges, we define the effective mass

$$m_{eff}(t + \frac{1}{2}) \quad = \quad \ln\left(\frac{\lambda^{(k)}(t, t_0)}{\lambda^{(k)}(t+1, t_0)}\right). \tag{3.24}$$

This quantity should form a plateau as a function of t once the contributions of the higher excited states are strongly suppressed. Additional information is provided by the eigenvectors $\vec{v}^{(k)}$. Their components should also show a plateau when only a single state contributes.

Another important feature of our analysis is that we use only a submatrix of the correlator matrix. We refer to this procedure as *pruning of the operator basis*. The reason is that many of the interpolators have only small overlap with the physical state or, given the limited number of gauge configurations, they convey no new information. Their inclusion contributes mainly noise to the correlator. Also, one can show [86] that choosing certain interpolator combinations helps in suppressing contributions of higher order corrections in the different eigenvalues. In this way, one can improve the effective mass plateaus to a certain extent by choosing an optimal, and often smaller, interpolator basis. However, to find such a combination is rather difficult, since the number of possibilities to choose a certain interpolator combination is extremely high. Pruning might also be very subjective and thus can lead to ambiguous results if several combinations of operators seem to be equally good but give slightly different effective mass plateaus. As long as these deviations are well within errors we should be allowed to choose anyone of these combinations.

The numerical results of our fits together with the optimal operators for the meson states can be found in the tables in Appendix B.

3.5.1 Effective masses

In Figure 3.1, we show the effective masses for pseudoscalar (PS), scalar (SC), vector (V), and axialvector (AV) mesons obtained on the $12^3 \times 24$ lattice for the four quark masses we have used in our calculations. The horizontal lines denote the time intervals where we have performed correlated fits to the eigenvalues and represent the resulting masses and their statistical errors.

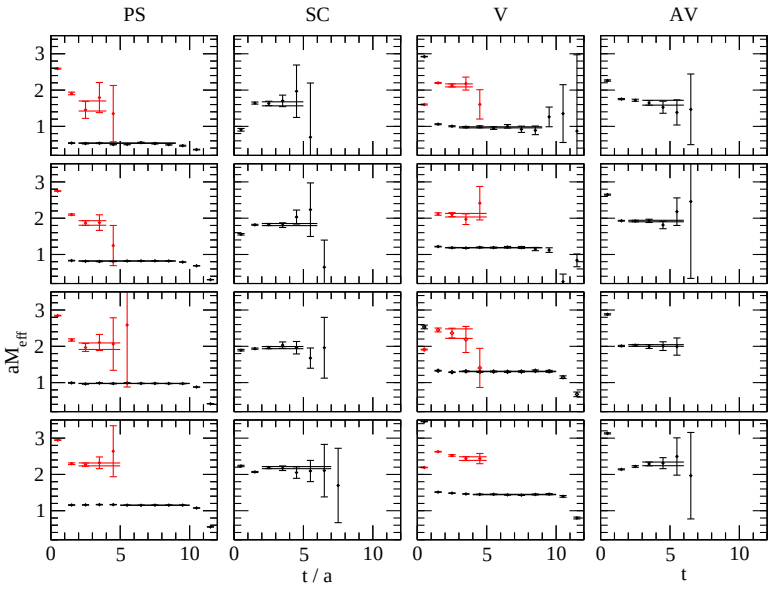

Figure 3.1: Effective mass plots for mesons from our coarse lattice ($12^3 \times 24$, with $\kappa = 0.1464, 0.1445, 0.1430, 0.1409$ from top to bottom). Both ground and excited states are shown, along with the $M \pm \sigma_M$ results (horizontal lines) from correlated fits to the corresponding time intervals.

We obtain excellent plateaus for the pseudoscalar and vector ground states. For these channels we are also able to extract first excited states. There, however, the results are not that good: The plateaus consist of only two or three effective mass points and are very noisy. We find that the ground states for both meson channels are practically unaffected by the choice of operators. For the excited pseudoscalar meson we are able to use the same optimal interpolator combination for all quark masses. However, to obtain results for the excited vector meson state we have to alter the optimal operator combination for each sea quark mass (see Appendix B).

The results for scalar and axialvector are also very good, however, slightly noisier than those of pseudoscalar and vector ground states. The fact that the pseudoscalar and vector channels yield better results than the other mesons is usually observed in lattice QCD. This is not unexpected since these states are much lighter than all the others and thus yield a better signal for a larger number of timeslices.

In Figure 3.2, we present the effective masses from the finer lattice.

Again we obtain excellent results for pseudoscalar and vector ground states with long clear plateaus. However, the situation for the excited pseudoscalar and vector states improved only marginally. The plateaus are noisy and rather

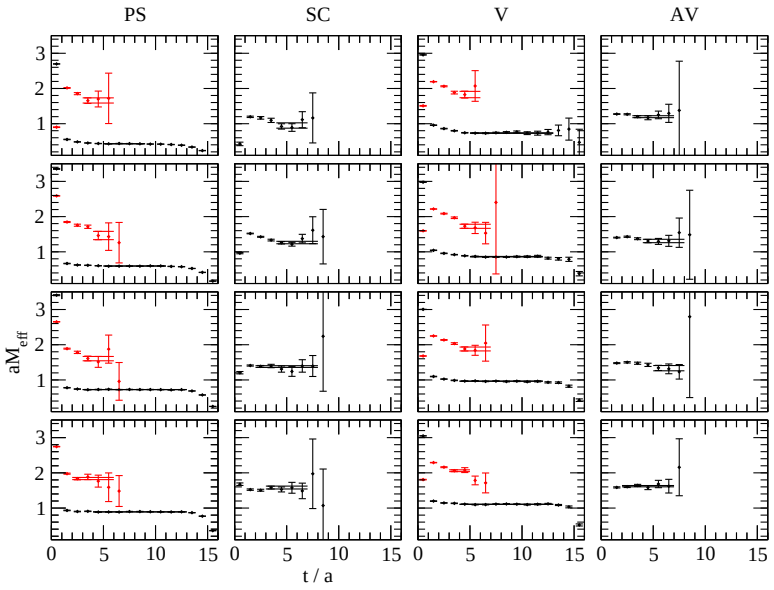

Figure 3.2: Effective mass plots for mesons from our fine lattice ($16^3 \times 32$, with $\kappa = 0.1410, 0.1400, 0.1390, 0.1375$ from top to bottom). Both ground and excited states are shown, along with the $M \pm \sigma_M$ results (horizontal lines) from correlated fits to the corresponding time intervals.

short, often we can include only three or four timeslices in our fits. Certainly an improvement is given by the fact that for the finer lattice we can choose the same optimal combination for all sea quark masses, except for the smallest quark mass. There we altered the optimal interpolator combination for the pseudoscalar meson slightly (see Appendix B).

In the scalar and axialvector channel we find only a slight improvement when going to the finer lattice. For the scalar meson it is necessary to choose a different operator for $\kappa = 0.1400$ than for the other masses. Since the combination $L\mathbb{1}n$ is very similar to $\nabla_i \mathbb{1} \nabla_i$ (both of them represent a three-dimensional lattice Laplacian but with different displacement), we do not regard this as a problem.

Fortunately, in our previous quenched studies [77, 78], we were able to use for each valence quark mass the same timeslice as starting point of the fit intervals. In this study, however, we sometimes need to change this timeslice as we move from one quark mass to next one. The reason is that the ensembles for different sea quark masses are generated independently. Thus, they should be completely uncorrelated, in contrast to the quenched case, where we changed only valence quark mass but always used the same set of configurations. Additionally, the effective lattice spacing depends on the sea quark mass. Nevertheless, we still require that both the effective mass and components of the corresponding eigenvector show plateaus in the fit interval.

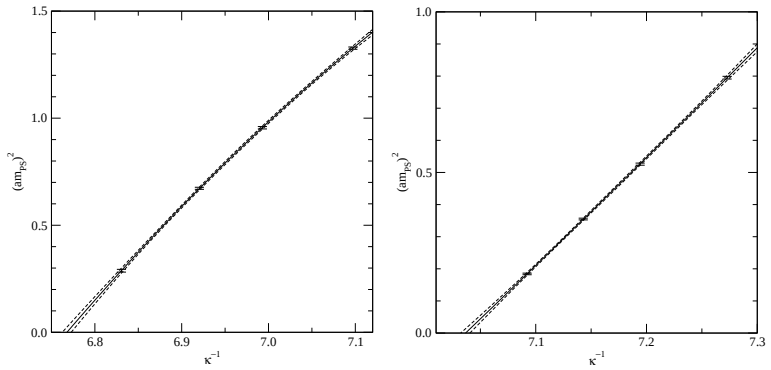

Figure 3.3: The figure shows $(am_{PS})^2$ as a function of κ^{-1}. The left plot is for the $12^3 \times 24$ lattice, while the right plot shows the results for the $16^3 \times 32$ lattice. We also show the results of our chiral extrapolation (solid line) together with the one sigma error band (dashed lines).

3.5.2 Pseudoscalar meson ground state

For the pion ground state the results of our fits are presented in Figure 3.3, where we plot the pion mass squared as a function of κ^{-1}. To be able to extrapolate our other results to the chiral limit, we have to determine the critical quark mass. It is defined as the value κ_c^{-1} where the mass of the pseudoscalar meson vanishes.

For the pseudoscalar meson the appropriate chiral extrapolation formula is given by resummed Wilson chiral perturbation theory (RWχPT) [82]. It reads

$$m_{PS}^2 = Am \left[-\log\left(\frac{Am}{\Lambda_0^2}\right)\right]^{\omega_0} \left[1 + \omega_1 m \log\left(\frac{Am}{\Lambda_3^2}\right)\right], \tag{3.25}$$

where $m = \frac{1}{2}(\kappa^{-1} - \kappa_c^{-1})$ is the quark mass and A, Λ_0, Λ_3, ω_0, and ω_1 are parameters in the theory. Since we have only four data points for each lattice it is not possible to use this expression as a fit function. Therefore, we restrict ourselves to a much simpler function given by

$$(am_{PS})^2 = B_{PS}\, m + C_{PS}\, m^2, \tag{3.26}$$

and we take κ_c^{-1} as additional fit parameter. The linear term is motivated by Wilson χPT without resummation

$$m_{PS}^2 = Am \left[1 + \omega_1 m \log\left(\frac{Am}{\Lambda_3^2}\right) + \omega_0 \log\left(\frac{Am}{\Lambda_0^2}\right)\right], \tag{3.27}$$

while we include the quadratic term in order to account for the slight curvature of our results. Since we are working at pion masses above 400 MeV, it is questionable whether χPT is applicable at all.

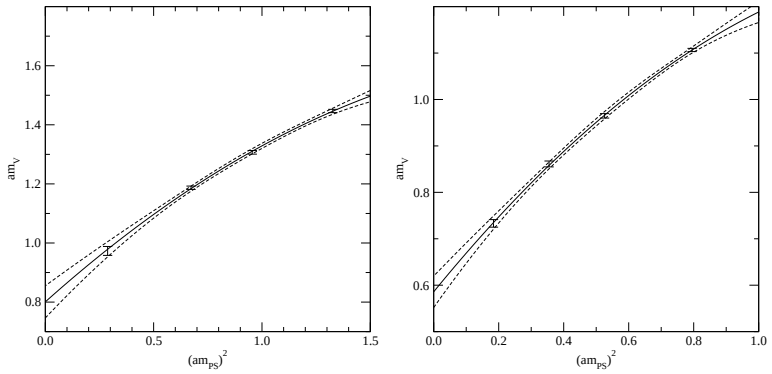

Figure 3.4: The figure shows the vector meson ground states as a function of $(am_{PS})^2$. The left plot shows the results for the $12^3 \times 24$ lattice, while the right plot shows the results for the $16^3 \times 32$ lattice. We also show the results of our chiral extrapolation (solid line) together with the one sigma error band (dashed lines).

3.5.3 Vector meson ground state

In Figure 3.4, we present our results for the vector meson ground state as a function of the mass of the pseudoscalar ground state.

For the chiral extrapolations we use

$$am_V = A_V + B_V(am_{PS})^2 + C_V(am_{PS})^4 \tag{3.28}$$

as the fit function.

Since our results for the pion and rho ground states are slightly different from the ones obtained by the CP-PACS collaboration, we re-determine the physical point and the lattice spacing by following the procedure described in [83]. For the physical point, we consider the ratio

$$\frac{am_\pi}{A_V + B_V(am_\pi)^2 + C_V(am_\pi)^4} = \frac{M_\pi}{M_\rho}, \tag{3.29}$$

where $M_\pi = 0.1396$ GeV and $M_\rho = 0.7755$ GeV are fixed to the experimental values. The lattice spacing is then given by

$$a = \frac{am_\rho}{M_\rho}, \tag{3.30}$$

with $am_\rho = am_V(am_\pi)$ being the mass of the rho meson in lattice units determined at the physical point for am_π, determined via Equation (3.29). In addition,

$L^3 \times T$	κ_{ud}^{-1}	am_π	am_ρ	a[fm]
$12^3 \times 24$	6.7722(27)	0.1438(28)	0.814(52)	0.2071(132)
$16^3 \times 32$	7.0400(21)	0.1055(18)	0.595(32)	0.1515(82)

Table 3.2: The physical point determined by matching the ratio $\frac{M_\pi}{M_\rho}$.

we can also compute κ_{ud}^{-1} which corresponds to up/down quark mass on the lattices by solving

$$(am_{PS})^2(\kappa_{ud}) = (am_\pi)^2. \tag{3.31}$$

The resulting values for the physical point am_π, the lattice spacing a, and the parameters am_π and am_ρ are summarized in Table 3.2.

3.5.4 Scalar and axialvector meson ground state

After determining the physical point and the lattice spacing, we can discuss the results for the other meson channels.

We start with the scalar ground state which is shown in the upper plots of Figure 3.5. For the $12^3 \times 24$ lattice, we find that the scalar mass depends linearly on the squared pion mass. Therefore, we perform linear fits in $(am_{PS})^2$ for the chiral extrapolation. This means that we fit our results to

$$am_{SC} = A_{SC} + B_{SC}(am_{PS})^2. \tag{3.32}$$

However, for the finer lattice the scalar meson mass for the smallest quark mass shows some deviation from the linear behavior of the other points. Therefore, we extend the expression in Equation (3.32) by an additional term $C_{SC}(am_{PS})^4$. We also try to add such an additional term to the fit functions of the other meson states. However, in all these cases the fit results for the corresponding parameter C is consistent with zero.

For the axialvector meson ground state (see Figure 3.5 lower plots) we find that the results on both lattices depend linearly on $(am_{PS})^2$. Thus, we use

$$am_{AV} = A_{AV} + B_{AV}(am_{PS})^2 \tag{3.33}$$

as the fit function for our chiral extrapolations. The only point which shows a slight deviation from a linear behavior is the point at $(am_{PS})^2 \approx 0.53$. Nevertheless, we have decided to include this point in our fit, since leaving it out changes our results negligibly.

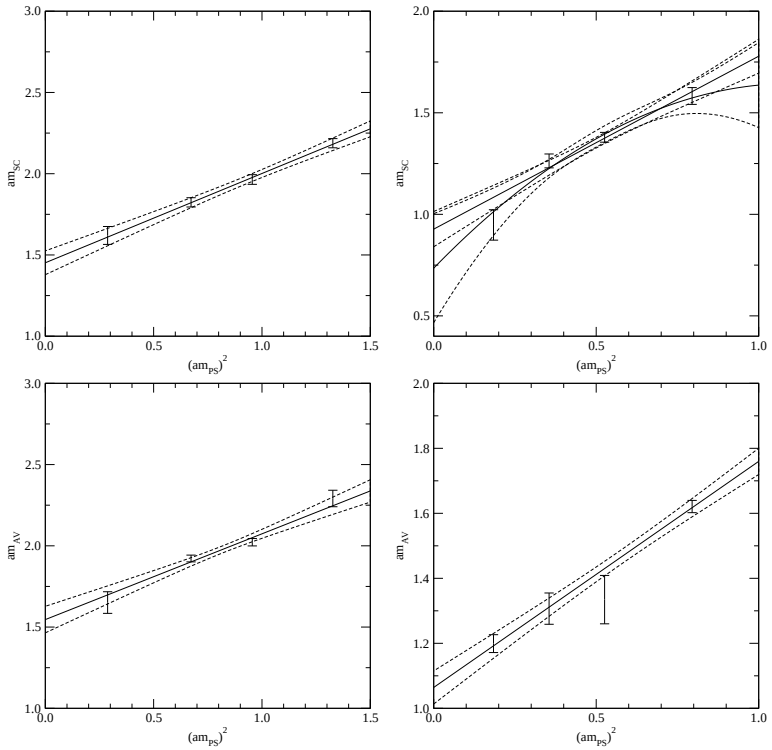

Figure 3.5: The figure shows the scalar meson ground states (upper plots) and the axialvector meson ground states (lower plots) as a function of $(am_{PS})^2$. The left plots show the results for the $12^3 \times 24$ lattice, while the right plots are for the $16^3 \times 32$ lattice. For the scalar meson results on the $16^3 \times 32$ lattice both linear and a quadratic fits have been performed. We also show the results of our chiral extrapolation (solid line) together with the one sigma error band (dashed lines).

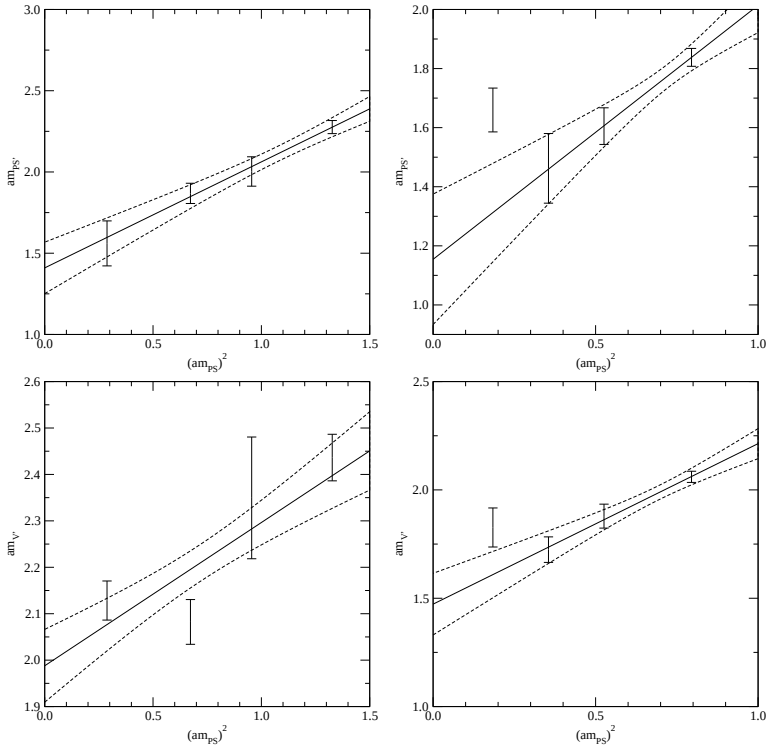

Figure 3.6: The figure shows the pseudoscalar meson excited states (upper plots) and the vector meson excited states (lower plots) as a function of $(am_{PS})^2$. The left plots show the results for the $12^3 \times 24$ lattice, while the right plots are for the $16^3 \times 32$ lattice. We also show the results of our chiral extrapolation (solid line) together with the one sigma error band (dashed lines).

3.5.5 Pseudoscalar and vector meson excited state

We start our discussion of the excited states with the excited pseudoscalar meson. In the upper plots in Figure 3.6 we plot the results of our fits to the eigenvalues as a function of $(am_{PS})^2$. On both lattices we find a linear behavior except for the smallest quark mass on the finer lattice which lies exceptionally high. We therefore do not include this point in our chiral extrapolations.

Next, we discuss the results for the excited vector meson channel. We find that our results on the coarse lattice are somewhat problematic. We observe a very jumpy behavior of the meson masses as a function of $(am_{PS})^2$. A reason for this might be that we had to choose different operator combinations for the different sea quark masses. This also makes the chiral extrapolation very difficult. We try a linear fit as the simplest choice. This leads to a value of $\chi^2/d.o.f. \approx 4$ which shows that the fit is not very reliable. Thus, the result should not be taken too seriously. On the finer lattice, we again find that the result for the smallest quark mass lies exceptionally high. Thus, we exclude also this point in our chiral extrapolation.

3.6 Summary

We compute the meson spectrum by evaluating the results of the chiral extrapolations at the physical point am_π and then converting them into physical units by using our results for the lattice spacing a (see Table 3.2). This means that for each meson channel we calculate

$$M_{meson} = \frac{[am_{meson}(am_\pi; A_{meson}, B_{meson}, C_{meson})]}{a}, \tag{3.34}$$

where A_{meson}, B_{meson}, and C_{meson} are the parameters that we have obtained from our chiral extrapolations and the a in the denominator stands for the lattice spacing, which we have determined with the rho meson.

Our final results for the meson spectrum are summarized in Figure 3.7, where we plot our results for both lattices in comparison with the experimental values from [87]. We do not show the vector meson ground state results since they have been used to determine the lattice spacing.

For the excited pseudoscalar meson our findings are in good agreement with the $\pi(1300)$ although the error for the finer lattice is quite large, thus making it also compatible with the $\pi(1800)$.

The results for the excited vector meson lie much too high. A reason for this might be the following: Our correlators are rather noisy, i.e., our effective mass plateaus are short, thus it might be that we start our fits too early. Another

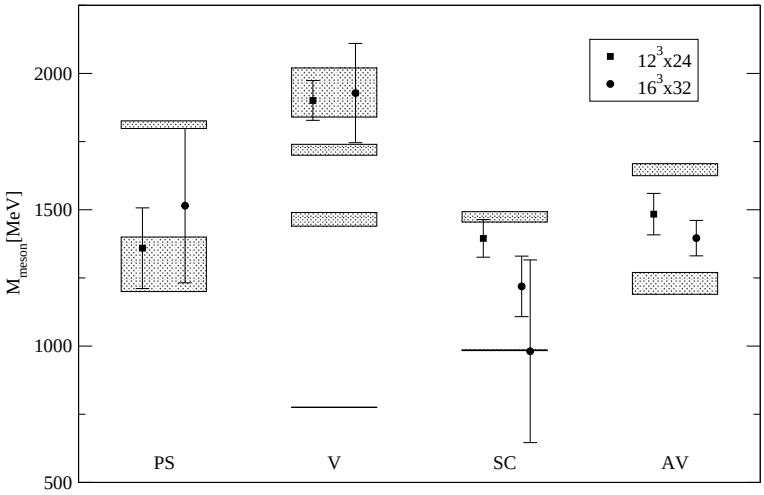

Figure 3.7: Final results for the meson spectrum from our calculation. The boxes with the shaded areas represent the experimental values as classified by the Particle Data Group [87]. For the scalar meson on the fine lattice we present results both for linear and quadratic extrapolation in $(am_{PS})^2$. The vector meson and pseudoscalar meson ground states are not shown, since the former is used to fix the lattice spacing a, and the latter becomes massless in the chiral limit.

explanation is that our quark masses are too large and a more sophisticated extrapolation is needed. Unfortunately this is not possible since we have too few data points. We also want to mention here that we have found something similar in our previous quenched studies [77] on a coarse lattice. There, a finer lattice was needed to obtain better results.

For the scalar meson our results on the coarse lattice are compatible with the $a_0(1450)$. However, on the finer lattice we find smaller values. The linear extrapolated results lie between the $a_0(980)$ and the $a_0(1450)$. When a quadratic fit is used, the average value for the mass becomes smaller but the error is much larger. The first finding is similar to what we already have observed in previous quenched studies with approximate chiral fermions. Recent studies with dynamical CI-fermions [88] however obtain a value which is consistent with the $a_0(980)$. This suggests that chiral sea quarks play a crucial role for scalar mesons.

For the axialvector meson our results are also higher than expected. They lie right between the $a_1(1260)$ and the $a_1(1640)$. This is similar to what we have seen in our previous quenched studies. Probably, here chiral sea quarks are needed to improve the situation, too.

Chapter 4

Estimation of all-to-all quark propagators

In Section 2.5.4, we showed how one usually calculates propagators in lattice QCD. We saw that it is done by iterative methods for a single source. In the end, one obtains a propagator from a single site to all sites on the lattice. For many applications, having the full propagator, i.e., the propagator from any location to any other point in the lattice, can be very advantageous. It can be used to determine specific quantities on a single configuration with high precision.

However, calculating the propagator D^{-1} exactly is not feasible, since we are dealing with a square matrix with about $O(10^5)$ rows and columns. Thus, direct inversion, i.e., inversion like in standard linear algebra, is not possible because it involves keeping the whole matrix in memory and performing a huge amount of computation. An alternative would be to put one source after the other on each site on the lattice and compute the resulting propagator like in Section 2.5.4. Also this task is not feasible. The only way to get the propagator (at least an approximate one) from anywhere to anywhere is to estimate it.

In recent years, a number of techniques have been developed for estimating propagators. The most naive method is the stochastic estimation technique. Here one uses a set of random source vectors, i.e, vectors on the whole lattice whose entries are random numbers. One way of improving such estimates is to sample better random vectors [89]. Other improvement schemes involve exact calculation of the lowest lying eigenmodes of the Dirac operator [90], performing so-called dilution of source vectors (see, e.g., Refs.[91]), or exploiting the properties of certain fermion formulations (for example, Hopping Parameter Acceleration [92]). Often two or more of these techniques are combined. Yet another type of improved estimate is the so-called Maximal Variance Reduction [93]. There, the lattice is decomposed in three different domains, two domains of interest and one domain which separates the other two from each other. Then one estimates the propa-

gators from one domain of interest to the other one using random sources being located in the third domain. Also noisier estimates from the source region to either of the two domains can be obtained.

In the following we present our own method, which is also based upon domain decomposition, or more specifically, the decomposition of block matrices. In contrast to the Maximal Variance Reduction, it has the advantage, especially for improved actions, of dealing directly with the Dirac operator (rather than its square). We end up with two types of estimators: one for "open" propagators between the two domains of the lattice, which we call "half-to-half" propagators, and one for "closed" propagators within one of the domains.

We begin our discussion with the derivation of the relevant formulas for our domain decomposition improvement (DDI). It relies on the block decomposition of matrices using the Schur complement. The latter is also used for even-odd-preconditioning of Dirac operators to speed up inversions [94] and there exists also a 5D Schur complement approach to overlap fermions (see [49] and references therein). And even for Hybrid Monte-Carlo simulations of Wilson fermions, domain decomposition methods in connection with the Schur complement have been applied with great success [95].

First tests for the closed contributions, using pseudoscalar disconnected diagrams as the observable, show that our method gives only very small improvement in this case. Therefore, we have decided to concentrate on the half-to-half propagators for which we present in Section 4.2 a subset of possible applications: The simplest case to use them is the spectroscopy of static-light mesons, i.e., mesons containing one infinitely heavy quark and one light antiquark (up, down, or strange). This also provides a perfect testing ground to get an impression of how good the improvement is. Static-light baryons, i.e., baryons containing one infinitely heavy quark and two light quarks, are a straightforward extension. A possible third application, which will be subject of a future project, are hadron three point functions, which can be used for the calculation of heavy quark effective theory parameters and form factors.

Then, after briefly summarizing the details of our numerical simulations, we present results for the static-light hadron sector, which is for the moment the main testing ground of our improvement scheme. We obtain excellent results and are able to extract a large number of states both for quenched simulations as well as for calculations performed on configurations with two flavors of dynamical Chirally Improved fermions. For the quenched results we can even perform a continuum extrapolation. At the end of this chapter we summarize our results and compare them to experiment, where possible.

Our improvement scheme has first been presented in [96] together with results from first tests. Preliminary results for static-light mesons have been published in [97].

4.1 Domain decomposition improvement

Before we come to the derivation of our improvement scheme, we would like to briefly discuss some of its main ingredients. To distinguish ordinary propagators, i.e., propagators which are evaluated by inversion upon a source, from the ones which are the subject of estimation, we use P in the following when we refer to the latter and denote the Dirac operator with M, since our method can be used for arbitrary matrices.

Stochastic estimation techniques use a set of random vectors χ_j^n, $n = 1, \ldots, N$ with the property

$$\frac{1}{N}\sum_{n=1}^{N} \chi_i^n \chi_j^{n\dagger} = \delta_{ij} + O(1/\sqrt{N}). \tag{4.1}$$

Such random vectors can for instance be created by inserting into each component of the χ's a number $e^{i\varphi}$ with phases φ which are selected randomly[1]. These vectors are then used as sources in Equation (2.107) to determine a corresponding set of solution vectors

$$\eta_i^n = M_{ij}^{-1}\, \chi_j^n \quad (n = 1, \ldots, N)\,. \tag{4.2}$$

The solutions and the sources can then be combined to construct an estimate of the full propagator:

$$M_{ij}^{-1} \approx \frac{1}{N}\sum_{n=1}^{N} \eta_i^n \chi_j^{n\dagger}\,. \tag{4.3}$$

For the domain decomposition we can think of the lattice as a disjoint union of two regions, which we denote with "1" and "2". The full Dirac matrix can then be written in terms of submatrices

$$M = \begin{pmatrix} M_{11} & M_{12} \\ M_{21} & M_{22} \end{pmatrix}, \tag{4.4}$$

where M_{11} and M_{22} connect sites within a region and M_{12} and M_{21} connect sites from the different regions. Regardless of the shape or nature[2] of the regions, a similarity transformation is all that is needed to reach this form. We can also write the propagator in this form:

$$M^{-1} = P = \begin{pmatrix} P_{11} & P_{12} \\ P_{21} & P_{22} \end{pmatrix}. \tag{4.5}$$

[1] Usually one uses $\mathbb{Z}_N$ noise. The entries are given by $\exp(i\frac{2\pi k}{N})$ with k being a equally distributed random integers between 0 and $N-1$.

[2] For example, different regions in color or Dirac space.

4.1.1 Derivation for open contributions

In the following we derive the formulas for our DDI based upon the properties of random vectors described above. An alternative derivation where the results follow from the path integral is presented in Appendix D.

We start with reconstructing the sources in one region, χ_1^n, from the solution vectors everywhere, η^n, and to separate the contributions from the different regions:

$$\chi_1^n = M\eta^n = M_{11}\eta_1^n + M_{12}\eta_2^n \,. \tag{4.6}$$

If we now apply the inverse of the matrix within one region, we have

$$M_{11}^{-1}\chi_1^n = \eta_1^n + M_{11}^{-1}M_{12}\eta_2^n \,. \tag{4.7}$$

This can be solved for η_1^n and substituted into the original expression for the noisy estimator of the propagator between the two regions:

$$\begin{aligned}
\left(M^{-1}\right)_{12} = P_{12} &\approx \frac{1}{N}\sum_{n=1}^{N} \eta_1^n \chi_2^{n\dagger} \\
&\approx \frac{1}{N}\sum_{n=1}^{N} \left[M_{11}^{-1}\left(\chi_1^n - M_{12}\eta_2^n\right)\right] \chi_2^{n\dagger} \\
&\approx -\frac{1}{N}\sum_{n=1}^{N} \left(M_{11}^{-1}M_{12}\eta_2^n\right) \chi_2^{n\dagger} \,,
\end{aligned} \tag{4.8}$$

where in the last line we eliminate the first term due to the fact that we expect $\lim_{N\to\infty}\sum_{n=1}^{N}\chi_1^n\chi_2^{n\dagger} = 0$. This is a crucial step, for here we cut out of the calculation what amounts to being only noise. It does not come for free, however, since we must perform the additional inversion within the subvolume 1. Writing out the full expression for η_2^n and again using $\lim_{N\to\infty}\sum_{n=1}^{N}\chi_1^n\chi_2^{n\dagger} = 0$, we obtain

$$\begin{aligned}
P_{12} &\approx -\frac{1}{N}\sum_{n=1}^{N} M_{11}^{-1}M_{12}P\chi_2^n\chi_2^{n\dagger} \\
&= -M_{11}^{-1}M_{12}P_{22} \,,
\end{aligned} \tag{4.9}$$

where the second line is an exact expression, showing that one can relate elements of different regions of $P = M^{-1}$ via the inverse of a submatrix of M. We do not pretend to have derived something new here; after all, P_{22} is the Schur complement of M_{11}^{-1}. We only wish to emphasize the useful connection with random-source techniques. Again, the lesson learned up to this point is that we need no sources in one of the two regions.

Further improvement can be achieved by looking again at Equation (4.9). Instead of the approximation $P_{22} \approx \frac{1}{N}\sum_{n=1}^{N} P\chi_2^n \chi_2^{n\dagger}$, we can place the approximate Kronecker delta between the M_{12} and P_{22}:

$$\begin{aligned} P_{12} &\approx -\frac{1}{N}\sum_{n=1}^{N} M_{11}^{-1} M_{12} \chi_2^n \chi_2^{n\dagger} P \\ &\approx -\frac{1}{N}\sum_{n=1}^{N} \left(M_{11}^{-1} M_{12} \chi_2^n\right) \left(P^\dagger \chi_2^n\right)^\dagger \\ &\approx -\frac{1}{N}\sum_{n=1}^{N} \left(M_{11}^{-1} M_{12} \chi_2^n\right) \left(\gamma_5 P \gamma_5 \chi_2^n\right)^\dagger \\ &\approx -\frac{1}{N}\sum_{n=1}^{N} \psi_1^n \phi_2^{n\dagger} \,, \end{aligned} \tag{4.10}$$

where we have used the γ_5-hermiticity of the propagator. This is done only for convenience since we could just as well work with $P^\dagger \chi_2^n$ in the ϕ_2^n. The reason is that most lattice QCD codes contain a highly optimized routine which multiplies the Dirac operator with a vector. The last step in this derivation is used to implicitly define the vectors ψ_1^n and ϕ_2^n. One can see from the form of the vector ψ_1^n in the next to last line that we only need sources in region 2 which "reach" region 1 via one application of M. In comparison to Equation (4.3), this significantly reduced the amount of noise in the estimate for P_{12}.

Unlike the naive estimator, Equation (4.3), where there is only one term giving a signal-to-noise of $\sim 1/V^{1/2}$, here there are many: for V_χ source points, the signal-to-noise is $\sim V_\chi/(V_\chi^2 - V_\chi)^{1/2} \sim 1$. Terms where the components of the sources are not the same can still be eliminated by "dilution" of the original source vectors, χ^n, that go into the ψ_1^n, the ϕ_2^n. Probably more important than these considerations, however, is the fact that, for most of the propagators between the regions, the random sources are kept far from the end points. This should, for similar reasons like for hopping parameter acceleration, improve the estimate even more. Also, one can use all points in one region for the starting location and all points in the other region as end point of the propagator, which is the reason why we call them half-to-half propagators.

Probably, the ideal domain decomposition for quark propagators which contribute to connected diagrams is then to use two unequal volumes, one containing a few more timeslices (those of the sources χ) than the other. Ideally, the centers of the two sets of source timeslices should be separated by $T/2$. The number of source timeslices is dictated by the lattice Dirac operator since the χ's should be placed on all timeslices which communicate with the other region via one application of M. For Wilson and Fixed-Point (FP) quarks, this is just two timeslices, one adjacent to each boundary. For Chirally Improved (CI) quarks, which we use

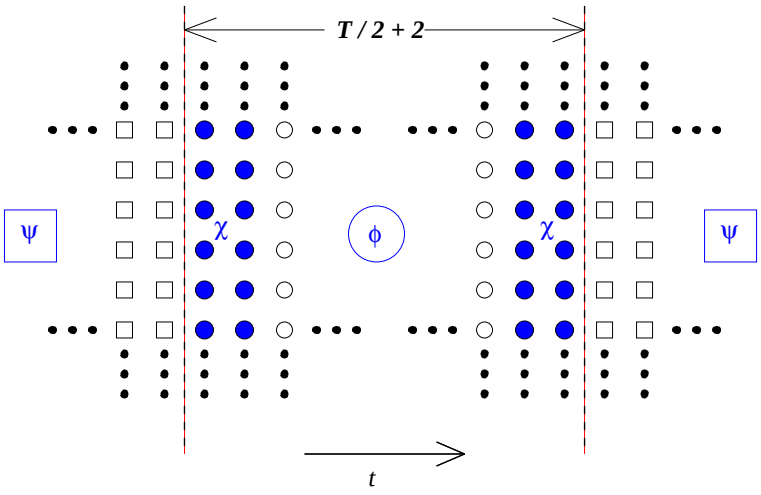

Figure 4.1: Depiction of the ideal decomposition and the sources (χ) which are needed to construct the estimate of the CI quark propagator between regions.

for our studies here, four are necessary (see Fig. 4.1). For the Asqtad action, six are needed due to the presence of the Naik term. While for Overlap fermions, it might be best to use equal volumes for the two regions since the sources will have to cover one region entirely. But we stress that for all of the above, one is free to dilute the random vectors: e.g., by inverting the sources on the different timeslices separately or performing spin or color dilution.

For our first attempt of using this method, we do not choose the ideal decomposition. We use equal volumes for the two regions and place sources next to the boundaries in both regions (see Fig. 4.2). Although this choice may not be ideal, it enables us to obtain two independent estimates of the quark propagator between the two regions:

$$-\frac{1}{N}\sum_{n=1}^{N}\psi_1^n\phi_2^{n\dagger} \approx P_{12} \approx -\frac{1}{N}\sum_{n=1}^{N}\gamma_5\phi_1^n\psi_2^{n\dagger}\gamma_5\,. \tag{4.11}$$

We conclude our discussion of the improvement of connected contributions by pointing out its advantages in comparison to the very similar Maximal Variance Reduction: First, we can work directly with M, instead of $M^\dagger M$ and it is less problematic to invert M since it has a better condition number than $M^\dagger M$ [93]. Second, implementing the method is straightforward. One needs only to limit the range of application of M when performing inversions in the subvolumes and when multiplying by the matrix between regions. Otherwise, existing routines remain unchanged. Third, the sources need only occupy enough timeslices to connect them with the other region via M, rather than $M^\dagger M$. These are the same number of sources for Wilson-like operators, where $M^\dagger M$, like M, only

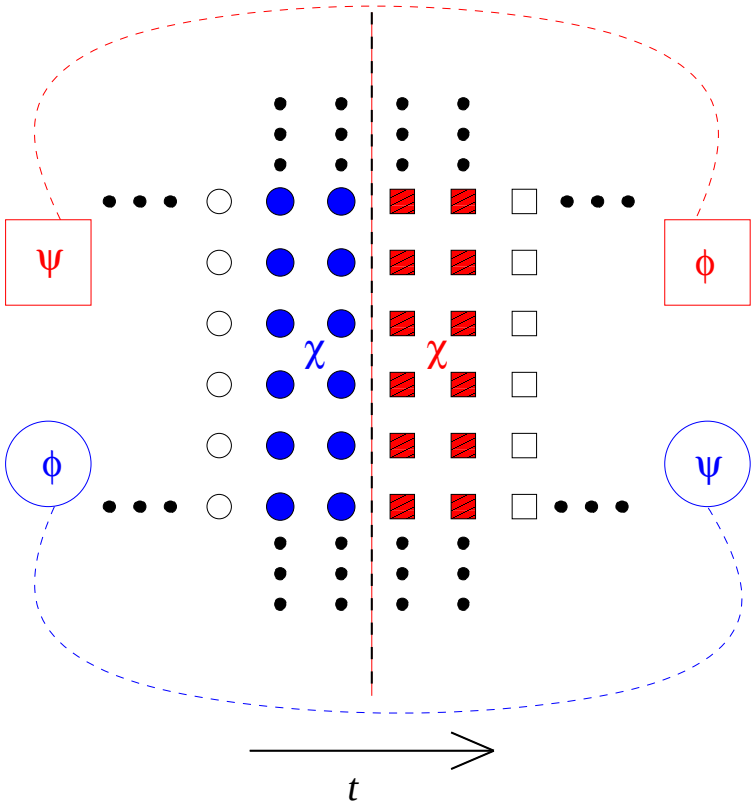

Figure 4.2: Depiction of one of the boundaries and the surrounding sources (χ) which we use to construct the two estimates of the CI quark propagator between regions of equal volume. Colors and shapes indicate which source region contributes to the signal in the resultant vectors. The ψ's are calculated using only one of the source regions, while the ϕ's use both.

extends one over timeslice. However, for many other improved operators, like CI and FP, this can reduce the number of timeslices occupied with random sources by a factor of two and thus the amount of noise.

4.1.2 Derivation for closed contributions

The derivation of the closed propagators, i.e., of propagators which start in one of the regions and return to it, is very similar to the one for the open contributions. When we consider for instance the propagator within region 1 we can write:

$$\begin{aligned} P_{11} &\approx \frac{1}{N}\sum_{n=1}^{N} M_{11}^{-1}\left(\chi^n\chi_1^{n\dagger} - M_{12}P\chi^n\chi_1^{n\dagger}\right) \\ &= M_{11}^{-1} - M_{11}^{-1}M_{12}P_{21}\,. \end{aligned} \tag{4.12}$$

So once again, through the consideration of random sources, we arrive at an exact expression. Now, combining the expressions for P_{11} and P_{21} $(= \gamma_5 P_{12}^\dagger \gamma_5)$, we arrive at the relation:

$$P_{11} = M_{11}^{-1} + M_{11}^{-1}M_{12}\gamma_5\left(M_{11}^{-1}M_{12}P_{22}\right)^\dagger\gamma_5\,. \tag{4.13}$$

Inserting our random sources into this expression gives

$$\begin{aligned} P_{11} &\approx M_{11}^{-1} + \frac{1}{N}\sum_{n=1}^{N}\left(M_{11}^{-1}M_{12}\gamma_5\chi_2^n\right)\left(\gamma_5 M_{11}^{-1}M_{12}P\chi^n\right)^\dagger \\ &\approx M_{11}^{-1} + \frac{1}{N}\sum_{n=1}^{N}\zeta_1^n\theta_1^{n\dagger}\,. \end{aligned} \tag{4.14}$$

Note that we put no region index on the second χ, indicating that for this resultant vector (θ_1) we wish to use sources initially placed everywhere on the lattice. The advantage of expression (4.14) may not be immediately clear since it still contains the explicit appearance of M_{11}^{-1}.

This seeming hindrance can be remedied by considering a very small volume for region 1. Performing this "highly reduced" inversion exactly, we hope to find a significant gain in the signal-to-noise ratio: The first term in the above expressions will be exact and the second term, as compared to its naive estimate, may be improved by a factor of as much as $\sim V_\chi^{1/2}$, where V_χ is now the volume of sources in region 2 which connect to region 1 via M. So if the volume of region 1 is kept small enough and the lattice Dirac operator connects each site to many others, there may be an advantage to calculating the M_{11}^{-1}'s exactly, as opposed to simply inverting more sources.

For our first tests, we use full-volume sources for χ, so that we can, in the end, use all sites as start and end point of the propagator P_{xx} with only N original

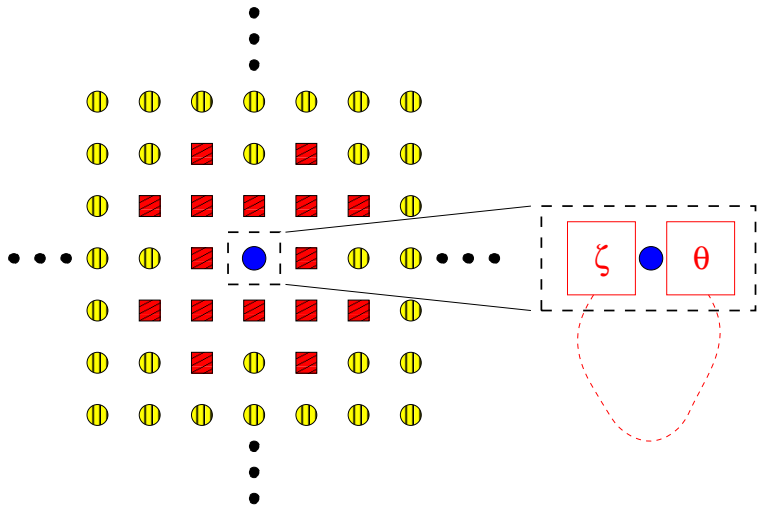

Figure 4.3: Depiction of the boundary and the surrounding region of sources which are needed to construct the estimated CI quark propagator to and from the central point. In this figure, region 1 is just one site (we also consider a larger region which includes nearest neighbors). The red squares indicate which region of sources contributes to the signal in the resultant vectors (ζ_1, θ_1) of Equation (4.14).

full-volume inversions: the $P\chi^n$ in θ_1^n. We can consider the smallest, symmetrical volume for region 1, the point itself ($V_1 = 1$; see Fig. 4.3), in order to reduce the amount of work needed to calculate M_{11}^{-1}, which we need for each point in the lattice. With this choice, at most one needs to invert V 12×12 matrices. Since $V_\chi = 128$ for the CI operator in this scenario, we hope that this small amount of extra work may be worth the effort. In the end, however, we actually use a larger region 1, including nearest neighbors ($V_1 = 9$).

As a preliminary test for our closed propagators, we take a look at some first results for the disconnected contributions to pseudoscalar ($J^P = 0^-$) meson correlators:

$$C(t) = \sum_{t_0,\vec{x},\vec{y}} \mathrm{Tr}(\gamma_5 P_{\vec{x},t_0;\vec{x},t_0}) \mathrm{Tr}(\gamma_5 P_{\vec{y},t_0+t;\vec{y},t_0+t}) \,. \tag{4.15}$$

We use 12 random spin-color sources, that are initially placed everywhere on the lattice, spin-dilute them in order to improve the method even more, and perform inversions ($P\chi^n$) at a quark mass of $am_q = 0.02$ on quenched configurations. We then condition these "naive" estimates via Equation (4.14) using the central point and its nearest neighbors as region 1. The exact calculation of all the M_{11}^{-1}'s for this sized region on a single configuration is numerically very cheap and takes less than a day on a single PC.

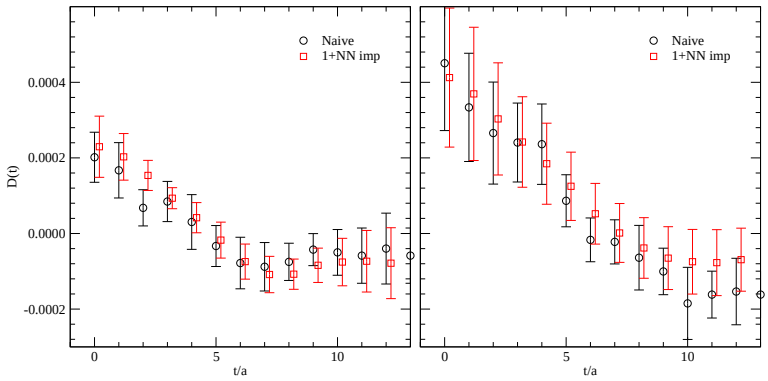

Figure 4.4: Naive and improved disconnected pseudoscalar correlators (with $am_q = 0.02$) on two different quenched configurations. Errors result from a single-elimination jackknife procedure over the 12 random spin-color sources.

In Figure 4.4 we compare results obtained via the naive and improved estimators on two different quenched configurations. The errors are estimated via the single-elimination jackknife subsets of the 12 random sources. Looking at the result for the configuration on the left, we can see significant reduction of the errors over many time separations. This is not the case for all configurations, however, as one can see on the right, where the errors are comparable, if not slightly larger for the improved version. For both cases shown here, and in fact for all configurations, the central values for the improved method follow a smoother curve. This should be no great surprise since the improved estimator uses sources on neighboring timeslices (see Figure 4.3), whereas the naive one does not. So the improved version should smoothen out some of the remaining fluctuations over different t values.

An important thing to note here is that, despite any of the improvement which we may gain from the smaller errors on some configurations and the smoothening of the curves, the error for the ensemble average of $C(t)$ will be dominated by the limited number of gauge configurations (i.e., this is what we call "gauge-limited" quantity). One can see from Figure 4.4 that the fluctuation which comes from switching configurations is as big as, or bigger than, the jackknife errors from the sources. For some other configurations, the jump in the corresponding $C(t)$ values is much larger. These are perhaps configurations with large values of topological charge, Q; after all, the integrated disconnected pseudoscalar correlator is related to the square of this quantity [98]:

$$\sum_t C(t) \propto \frac{Q^2}{m_q^2}\,, \tag{4.16}$$

where the relation is only approximate here since we use only Chirally Improved quarks.

Altogether we see no great overall improvement for these light, disconnected pseudoscalars. However, this is a tough testing ground. It remains to be seen how well these improved closed propagators will perform for other quantities where only averages of single loops over single timeslices are needed: e.g., $s\bar{s}$ loops within hadron correlators to measure the strangeness content, an application which we plan to look into in the future. We also point the interested reader to other improvement schemes for closed contributions: see, e.g., [99, 100].

In the following, however, we do not pursue any further applications of the closed propagators, but concentrate on the half-to-half propagators.

4.2 Applications for half-to-half propagators

Half-to-half propagators can be used for many different applications in lattice QCD. In the following, we discuss only a small subset of them: Static-light hadron spectroscopy and hadron three-point functions for the example of mesons.

4.2.1 Static-light spectroscopy

As a main test application for our half-to-half propagators we consider spectroscopic calculations for B-mesons in lowest order heavy quark effective theory (HQET) [101], the so-called static-light approximation. This approach treats the bottom quark as infinitely heavy and thus ignores its spin degrees of freedom. It is legitimized by the fact that the Compton wavelength of the heavy quark m_b^{-1} is much smaller than the typical hadronic length scale, which is given by Λ_{QCD}^{-1}.

The propagator for the static quark can be derived from HQET. On the lattice it reads

$$G_{x;y}^{(static)} = \frac{\mathbb{1} + \gamma_4}{2} \Theta(x_4 - y_4)\, \delta_{\vec{x};\vec{y}} \prod_{i=0}^{t-1} U_4^{\dagger}(x + ia\hat{4}) \tag{4.17}$$

It is a product of temporal link variables and thus describes a lattice discretized Schwinger line. The only spin structure which has remained is the parity projector $\frac{\mathbb{1}+\gamma_4}{2}$. This means that it is numerically cheap to compute. We also see that the static quark only moves forward in the temporal direction. When we construct hadrons which contain such propagators they also move only forward in time.

A simple Euclidean two-point correlation function is given by

$$\begin{aligned} C(\vec{x}_0, t_0; \Delta t) &= \sum_{\vec{x}} \left\langle B(\vec{x}, t_0 + \Delta t)\, \bar{B}(\vec{x}_0, t_0) \right\rangle \\ &= \sum_{\vec{x}} \left\langle \bar{q}(\vec{x}, t_0 + \Delta t) \mathcal{O} b(\vec{x}, t_0 + \Delta t)\, \bar{b}(\vec{x}_0, t_0) \mathcal{O}^\dagger q(\vec{x}_0, t_0) \right\rangle \\ &= \sum_{\vec{x}} \mathrm{Tr} \left[\mathcal{O} G^{(static)}_{\vec{x}, t_0+\Delta t; \vec{x}_0, t_0} \mathcal{O}^\dagger P_{\vec{x}_0, t_0; \vec{x}, t_0+\Delta t} \right] \\ &= \sum_{\vec{x}} \mathrm{Tr} \left[\mathcal{O} \frac{\mathbb{1} + \gamma_4}{2} \Theta(\Delta t) \delta_{\vec{x}; \vec{x}_0} (\prod U_4^\dagger) \mathcal{O}^\dagger P_{\vec{x}_0, t_0; \vec{x}, t_0+\Delta t} \right] \\ &= \Theta(\Delta t) \mathrm{Tr} \left[\mathcal{O} \frac{\mathbb{1} + \gamma_4}{2} (\prod U_4^\dagger) \mathcal{O}^\dagger P_{\vec{x}_0, t_0; \vec{x}_0, t_0+\Delta t} \right], \end{aligned} \tag{4.18}$$

where $\mathcal{O}, \mathcal{O}^\dagger$ contain combinations of Dirac matrices and covariant derivatives, which determine the quantum numbers of the state.

In the last line, we see that only a single term contributes to the correlator leading to a very poor signal. To increase the statistics on a single configuration one would like to average over all starting points $(\vec{x}_0, t_0)$. However, with standard techniques for the calculation of light propagators, this is prohibitively expensive, since it would require one inversion for each $(\vec{x}_0, t_0)$. Thus, using all-to-all or in our case half-to-half propagators for P is a much cheaper alternative. In a first step we average over all spatial sites of a given starting timeslice t_0. The correlator then reads

$$C(t_0; \Delta t) = \frac{1}{L^3} \sum_{\vec{x}_0} C(\vec{x}_0, t_0; \Delta t). \tag{4.19}$$

With all-to-all propagators we would be able to average over all starting timeslices t_0, too. With our technique we at least can average over all the timeslices within one of the regions, when the correlation function ends in the other domain. We denote this average with $\sum'_{t_0}$. After inserting our estimates for the light propagator the correlator reads

$$C(\Delta t) = -\frac{1}{L^3} \sum_{\vec{x}_0} \sum_{t_0}{}' \frac{1}{N} \sum_{n=1}^{N} \Theta(\Delta t) \mathrm{Tr} \left[\mathcal{O} \frac{\mathbb{1} + \gamma_4}{2} (\prod U_4^\dagger) \mathcal{O}^\dagger \psi^n_{\vec{x}_0, t_0} \phi^{n\dagger}_{\vec{x}_0, t_0+\Delta t} \right] \tag{4.20}$$

For our particular implementation a second, independent estimate can be obtained by using γ_5-hermiticity as described in Equation (4.11). Since only the light propagator needs to be estimated the errors from the random sources are of order $O(\frac{1}{\sqrt{N}})$.

The increase in statistics is not the only thing we gain by using our half-to-half propagators. Another improvement comes from the fact that we can use

interpolators with different wave functions without the necessity of additional inversions. Thus, we can easily construct a number of interpolators for a number of B-meson channels, which allows us to extract also excited states.

There is one small drawback when calculating hadron spectra in the static-light approximation. All masses which we extract from the Euclidean two-point correlation functions are shifted by an a-priori unknown amount due to the static quark. This quantity has no well-defined continuum limit since it contains a power term in the inverse lattice spacing a^{-1}. We can remove this effect by restricting ourselves to mass splittings.

4.2.2 Static-light-light spectroscopy

A straightforward extension to static-light mesons is to consider baryons containing one infinitely heavy quark. The resulting correlators should then allow us to extract mass splittings between a reference particle, e.g., the lowest lying B-meson state, and the baryons Λ_b and Σ_b.

In comparison to static-light mesons the situation is complicated by the fact that static-light baryons contain two light quarks. For each of them an estimate has to be introduced, which of course increases the noise in the correlators. Since the estimates must be independent of each other we in principle have to create separate random vectors and resulting solutions for each of the propagators. However, we can overcome this problem by so-called noise recycling. The idea behind this is to use the same set of random source and solution vectors for both light propagators, but to avoid the situation of cross-terms, i.e., the case where exactly the same vectors are used to estimate both propagators. This means, that instead of performing a single sum over n like in Equation (4.20), we have to sum over two indices n, n' with $n \neq n'$, which can be reduced to $n < n'$, since the correlators are symmetric in these indices.

As the static-light-light interpolator for the Λ_b, we consider

$$\Lambda_Q = \epsilon_{abc} b_a (u_b^T \Gamma d_c), \tag{4.21}$$

where Γ is $C\gamma_5$ or $C\gamma_4\gamma_5$. When we change the light quark content from ud to us, also Ξ_b can be accessed. In addition, we can consider

$$\Sigma_Q^{(*)} = \epsilon_{abc} b_a (u_b^T \Gamma d_c), \tag{4.22}$$

where Γ is $C\gamma_i$ and $C\gamma_4\gamma_i$. Here, we can average over the three spatial components i. This interpolator couples to Σ_b which is degenerate with the Σ_b^*, since in the static approximation the heavy quark spin is ignored. By changing the light quark content, also in this case other states can be accessed. These are Ξ_b', Ξ_b^* and Ω_b, Ω_b^* for us and ss, respectively.

4.2.3 Three-point functions

In this section, we briefly describe how to use all-to-all propagators for hadron three-point functions. This is a particularly interesting application which we would like to explore with our domain decomposition improvement in the future. Three-point functions allow one to extract matrix elements, which can, for example, be related to moments of structure functions and form factors.

Here, we consider as a simple example a pion, which is probed by a vector current $\mathcal{O}_\mu(\tau) = \sum_{\vec{y}} \bar{d}(\vec{y},\tau)\gamma_\mu d(\vec{y},\tau)$. The generalization to other hadrons and currents is straightforward. For a very detailed discussion of the meson case, the interested reader is referred to [102], while in [55, 103] the nucleon case is described.

A pion three-point function with the current insertion, mentioned above, is given by the expression

$$\begin{aligned}
C(t,\tau,\vec{p}) &= \Big\langle \pi(\vec{p},t)|\mathcal{O}_\mu(\tau)|\bar{\pi}(\vec{x}=\vec{0},t=0)\Big\rangle \\
&= \sum_{\vec{x},\vec{y}} e^{-i\vec{p}\vec{x}} \Big\langle \bar{u}(\vec{x},t)\gamma_5 d(\vec{x},t)\ \bar{d}(\vec{y},\tau)\gamma_\mu d(\vec{y},\tau)\ \bar{d}(\vec{0},0)\gamma_5 u(\vec{0},0)\Big\rangle \\
&= \sum_{\vec{x},\vec{y}} e^{-i\vec{p}\vec{x}} \Big\{ \mathrm{Tr}_{\mathrm{SC}}\left(\gamma_5 D_u^{-1}(\vec{0},0;\vec{x},t)\gamma_5 D_d^{-1}(\vec{x},t;\vec{y},\tau)\gamma_\mu D_d^{-1}(\vec{y},\tau;\vec{0},0)\right) \\
&\quad - \mathrm{Tr}_{\mathrm{SC}}\left(\gamma_5 D_u^{-1}(\vec{0},0;\vec{x},t)\gamma_5 D_d^{-1}(\vec{x},t;\vec{0},0)\right)\mathrm{Tr}_{\mathrm{SC}}\left(\gamma_\mu D_d^{-1}(\vec{y},\tau;\vec{y},\tau)\right)\Big\} \\
&= \sum_{\vec{x},\vec{y}} e^{-i\vec{p}\vec{x}} \Big\{ \mathrm{Tr}_{\mathrm{SC}}\left(D_u^{-1\dagger}(\vec{x},t;\vec{0},0) D_d^{-1}(\vec{x},t;\vec{y},\tau)\gamma_\mu D_d^{-1}(\vec{y},\tau;\vec{0},0)\right) \\
&\quad - \mathrm{Tr}_{\mathrm{SC}}\left(D_u^{-1\dagger}(\vec{x},t;\vec{0},0) D_d^{-1}(\vec{x},t;\vec{0},0)\right)\mathrm{Tr}_{\mathrm{SC}}\left(\gamma_\mu D_d^{-1}(\vec{y},\tau;\vec{y},\tau)\right)\Big\}
\end{aligned} \tag{4.23}$$

In the last step, we have used the γ_5-hermiticity of the Dirac operator. We find that the three-point function consists of two terms, the second term being an ordinary pion two-point function multiplied by a disconnected diagram. For this term our technique for disconnected contributions is potentially interesting.

However, we focus on the first term. For its evaluation we need two propagators which connect the origin to all points on the lattice. For those we can use the standard technique, i.e., the inversion on a source, which is placed at $(\vec{x}=\vec{0},t=0)$. The problematic propagator is the one, which connects the current insertion at $(\vec{y},\tau)$ to the sink at $(\vec{x},t)$. Usually one uses the sequential source technique in such a case. This means the term $\sum_{\vec{x}} e^{-i\vec{p}\vec{x}} D_u^{-1\dagger}(\vec{x},t;\vec{0},0) D_d^{-1}(\vec{x},t;\vec{y},\tau)$ is determined by performing additional inversions on suitably chosen, so-called sequential sources (, i.e., sink operators constructed in a special way). The problem hereby is that for each sink timeslice t and momentum $\vec{p}$ the computation of one additional propagator is necessary. Since one is often interested in the momentum

dependence of the matrix elements and also wants to understand the systematic effects coming from a change in t, this becomes numerically expensive. As an alternative one can use all-to-all techniques to estimate that propagator.

Especially interesting is the case where the timeslices τ and t are well separated. Thus, it is a perfect application for our domain decomposition improved half-to-half propagators, if the boundary timeslices in our technique are placed in such a way that the timeslice τ is in one region, while timeslice t lies in the other domain.

4.3 Simulation details

Like for the excited light mesons in Chapter 3, we are not only interested in the ground states of static-light mesons. Therefore, we use a number of different smearings for our meson operators which allow us to construct a cross-correlation matrix for each of the spin channels in which we are interested. For the extraction of excited states we again utilize the variational method, which we have already described in Section 3.2. For the normalization timeslice we choose $t_0 = 3$, except stated otherwise. The reason for this is that the Chirally Improved Dirac operator extends over two timeslices. It has been pointed out that there might be an issue with unitarity because of this. Although we do not find any evidence for this in our results, we use $t_0 = 3$ to ensure that possible effects coming from that problem are reduced.

Also for the static-light baryons, various interpolators are constructed. On the one hand side, we consider the different Dirac structures, which we have shown above. In addition we also use different smearings for the light quarks. However, for the results presented in this thesis, we have only considered the case where both light quarks in the static-light baryons have the same masses.

Our calculations are performed on a number of ensembles. We have three sets of quenched lattices and two ensembles of configurations with $N_f = 2$ dynamical Chirally Improved fermions, all of them with Lüscher-Weisz gauge action. In each case, we use Chirally Improved fermions as valence quarks. More details about the configurations can be found in Appendix H. To reduce the discretization errors of the static quark propagator, we use HYP smeared links [104] in the quenched and stout smeared ones [105] in the dynamical case for its construction.

Our half-to-half propagators and the static-light correlators on the larger lattices have been calculated on the cluster of the LRZ in Munich. For the correlators on the smaller lattices we have used the cluster of the physics department in Regensburg.

operator	J^P	states	$O(\Gamma, \vec{\nabla})$
S	$(0,1)^-$	$B^{(*)}$	γ_5
P_-	$(0,1)^+$	$B^{(*)}_{0,1}$	$\sum_i \gamma_i \nabla_i$
P_+	$(1,2)^+$	$B^{(*)}_{1(2)}$	$\gamma_1\nabla_1 - \gamma_2\nabla_2$
$D_\pm$	$(1,2,3)^-$	$B^{(*',*)}_{2(3)}$	$\gamma_5(\nabla_1^2 - \nabla_2^2)$

Table 4.1: Static-light meson operators. ∇_i is the covariant lattice derivative, which has been defined in Equation (3.22).

4.4 Results for static-light hadrons

As static-light meson interpolators we consider quark bilinears of the form

$$\bar{b}\,\mathcal{O}_j q = \bar{b}\,O(\Gamma, \vec{\nabla})\left(\Delta^{(3)}\right)^{l_j} S_J(\kappa, N_{sm,j})\, q, \tag{4.24}$$

where $\Delta^{(3)}$ and S_J are the three-dimensional gauge covariant lattice Laplacian and the Jacobi smearing operator, which we have defined in Section 3.3. The quantum numbers of the interpolating fields are determined by $O(\Gamma, \vec{\nabla})$ which are listed in Table 4.1, together with their corresponding spin-averaged heavy-light states[3]. The details of the smearings, we apply, can be found in Appendix H.

For the static-light baryons, we use the interpolators, which we have presented in Section 4.2.2. Both light quarks are smeared in the same way. As smearing parameters, we use $\kappa = 0.20$ in combination with $N_{sm,1}$ and $N_{sm,2}$, except for the finest quenched lattice, where up to now only simulations with $N_{sm,2}$ were run.

Since the static quark propagates only forward in time direction, also the resulting meson or baryon travels only forward in time. Thus, we cannot symmetrize anymore with respect to $\frac{T}{2}$, like it has been possible for the light mesons in the previous chapter. However, this has also an advantage. We can calculate two different correlators, one where the static-light hadron propagates from region 1 to region 2 forward in time and another one where the propagation goes from region 2 to region 1 again forward in time. Both these contributions are then averaged. As for the light mesons, we calculate the effective mass according to

$$m_{eff}(t + \frac{1}{2}) = \ln\left(\frac{\lambda^{(k)}(t, t_0)}{\lambda^{(k)}(t+1, t_0)}\right). \tag{4.25}$$

[3]We use a parenthetical notation to denote spin averages. For example, by $B^{(*)}$ we mean the spin average of the pseudoscalar B and vector B^* states: $M_{B^{(*)}} = (M_B + 3M_{B^*})/4$. We use $B^{(*)}_{s1(2)}$ for the average of B_{s1} and B^*_{s2}: $M_{B^{(*)}_{s1(2)}} = (3M_{B_{s1}} + 5M_{B^*_{s2}})/8$. A similar notation is used for the baryons.

For the determination of the fit ranges we do not only rely on the effective masses but also take the components of the eigenvectors into account. Only if both of these observables show decent plateaus, we can be sure that only a single state contributes. Following the procedures in the previous chapter, we again prune our basis of operators in order to remove certain interpolators, which have only poor overlap with the considered states.

4.4.1 Effective masses

In this section we present a subset of the effective masses for the static-light mesons. We have chosen the quenched and dynamical results obtained on the two $16^3 \times 32$ lattices. The reason is that for both ensembles the lattice spacing and thus the spatial volume are approximately the same. Thus, we expect that both of them are affected by similar finite volume effects. But this does not imply that they are also affected by similar discretization errors. After all, one of them is quenched and the other one is dynamical and different smearings for the gauge fields were used. Also the statistics are different.

In Figure 4.5, we show the effective masses for the different spin channels obtained on the quenched configurations. The light quark has a mass which corresponds approximately to the mass of the strange quark on that lattice. In each of the plots we also display the results of the correlated fits to the eigenvalues. They are denoted by the horizontal lines and represent the obtained mass plus and minus the one sigma error.

In the upper left plot, the results for the ground and two excited states in the S-wave channel are presented. The ground state shows a long and steady plateau with negligible statistical errors, therefore we do not show the result of our fits for this channel. Also the plateau for the first excited state is well pronounced. The second excited state is much noisier. Nevertheless, we include it in our analysis.

The signal for the $D_\pm$ state (upper right plot of Figure 4.5) is noisier than for the other three channels. We are able to extract a ground state, which shows a reasonable plateau, while the signal in the higher eigenvalue channels is just too poor.

The P-wave channels, which are shown in the two lower plots, are also of good quality. We obtain reliable results for the ground states, which show clean plateaus. The first excited states are noisier.

Figure 4.6 shows our results for the $16^3 \times 32$ dynamical configurations. In all the channels the signal is noisier than in the quenched case. There are two reasons for this. On the one hand side the sea quarks create additional fluctuations and also possible autocorrelations between the configurations are increased.

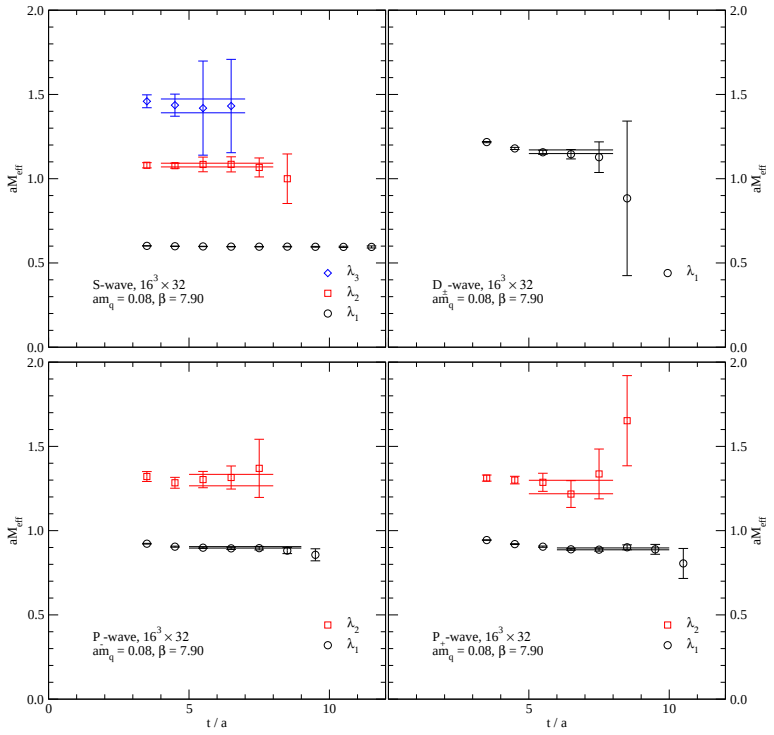

Figure 4.5: Effective masses for the static-light mesons on the quenched $16^3 \times 32$ lattice at $am_q = 0.08$, which approximately corresponds to the strange quark mass for that lattice. The horizontal lines represent $M \pm \sigma_M$, which have been obtained from correlated fits of the eigenvalues in the corresponding time intervals.

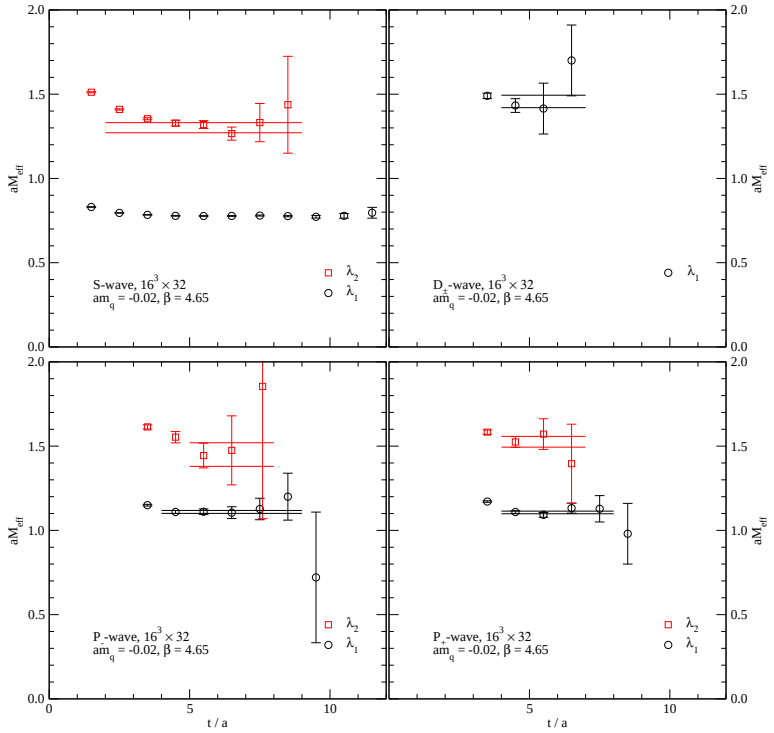

Figure 4.6: Same as in previous figure but for the dynamical $16^3 \times 32$ lattice just below the strange quark mass. Like in Figure 4.5, the horizontal lines represent $M \pm \sigma_M$, which have been obtained from correlated fits of the eigenvalues in the corresponding time intervals. The first excited S-wave state has been fitted to the sum of two exponentials in the displayed time interval.

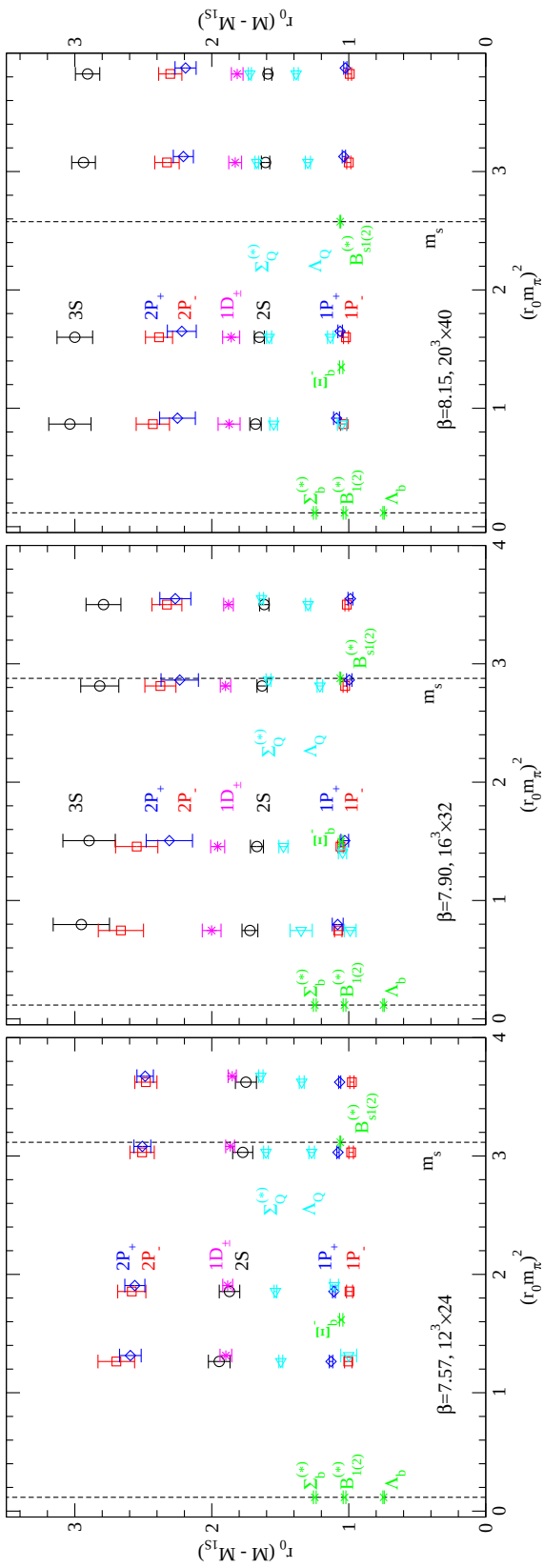

Figure 4.7: Physical mass splittings $(M - M_{1S})$ as a function of m_π^2 for the $12^3 \times 24$, $16^3 \times 32$, and $20^3 \times 40$ quenched lattices (left to right). All quantities are in units of the Sommer parameter r_0. The vertical lines denote the chiral limit and the pion mass which corresponds to the strange quark mass on the lattices. The green $\times$'s are the latest experimental mass splittings after appropriate spin averaging, taken from [87, 106, 107, 108, 109, 110, 111]. All errors are only statistical from the chosen fit ranges.

For the S-wave channel, we again find a clear and long plateau for the ground state. A plateau in the excited state is reached only very slowly. This is due to contributions from higher order corrections, which contaminate the eigenvalue at small times. In order to improve the extraction of the first excited state we perform a fit of λ_2 to the sum of two exponentials. The fit range is given by the horizontal lines, which also in this case show the mass plus and minus the standard deviation of the $2S$ state. To make this fit possible we have changed the normalization timeslice for the variational method from $t_0 = 3$ to $t_0 = 1$ in this case.

The upper right plot in Figure 4.6, shows the effective mass for the $D_\pm$ ground state. For this channel the results are very noisy and the outcome of the fit should be taken with care. It is absolutely necessary to increase the statistics of our calculations for this state. This is a non-trivial task since very expensive simulations are necessary to generate more dynamical configurations.

For the P-wave channels, shown in the lower two plots, our results are only slightly noisier than the effective masses obtained on the quenched lattice. For both of these channels we are able to extract not only the ground state but also a first excited state, for this quark mass. Unfortunately, the signal for the excited P_+ becomes worse for smaller quark masses, which makes it impossible to reliably fit the eigenvalue.

4.4.2 Static-light meson spectrum

In the following we present our results for the mass splittings of the different B-meson states. Previous results which have been obtained from first tests of our domain decomposition improvement are published in [96]. Here we concentrate on newer results obtained on a number of quenched configurations and two sets of lattices with two flavors of dynamical Chirally Improved fermions. Preliminary results are published in [97].

To allow for a comparison with the experimental values of the mass splittings we have to take into account that we work in the static approximation for the heavy quark. As we have already mentioned, this approximation ignores the spin of the heavy quark. Thus, we cannot directly compare our results with experimental values but only with spin averaged quantities.

Figure 4.7 shows the mass splittings ($M - M_{1S}$) as a function of pseudoscalar mass-squared ($m_\pi^2 \propto m_q$) for the $12^3 \times 24$, $16^3 \times 32$, and $20^3 \times 40$ quenched lattices from left to right, all in units of the Sommer parameter r_0. The vertical lines mark the chiral limit and the pion mass which corresponds to the strange quark mass on the lattices. The green crosses on those lines are the experimental values for $B^{(*)}_{1(2)}$ and $B^{(*)}_{s1(2)}$ taken from [106, 107, 108]. Also results for the static-light baryons are shown, but they are subject of the next section.

A general observation which we make on all our lattices, both quenched and dynamical, is the fact that the mass splittings for the static-light mesons seem to increase as the light quark mass becomes smaller. At most, they stay approximately constant as the chiral limit is approached. This is not unexpected. After all, we are looking at mass splittings and these usually become larger when one goes to lighter quark masses. Nevertheless, it is problematic for the P_+, since according to experiment the splitting for this state should become smaller as the light quark mass is reduced. Maybe it is an effect of the static approximation and this discrepancy vanishes when kinetic corrections are included.

For the coarsest lattice (left plot), we find mass splittings for all higher spin channels and are even able to extract first excited states for the S- and both P-wave channels. This is also the only lattice where we find a clear difference between the splittings of P_- and P_+. The P_+ in the chiral limit lies 15% to 20% above the $B^{(*)}_{1(2)}$. On the other hand the $B^{(*)}_{s1(2)}$ seems to be consistent with the P_+ at the strange quark mass. The $2S$ is consistent with the $1D_\pm$ and becomes even larger in the chiral limit. Also the excited P-waves are lying on top of each other.

Next we look at the quenched $16^3 \times 32$ lattice (middle plot). In addition to the states mentioned above, we can also extract a $3S$ state. On this finer lattice the difference between $2S$ and $1D_\pm$ is resolved, the latter being heavier in mass. This is expected since the $D_\pm$ represents an average of higher spins than the S and the heavy quark spin interactions which would mix the purely orbitally excited D-waves with the ground state S-wave are absent in the static limit. However, the two P-wave ground states are now lying on top of each other. For the excited P-waves we also obtain results which are consistent with each other, except for the smallest light quark mass where we have not obtained a reliable result for the $2P_+$. It is interesting to note that in the chiral limit the $2P_-$ extrapolates to a higher value than the $2P_+$. However, this is mainly due to the fact that the $2P_+$ is approximately constant as a function of the quark mass, while the $2P_-$ rises linearly.

The results for the mesons on our finest lattice (right plot) are very similar to the ones on the $16^3 \times 32$. The one noticeable difference is the smaller linear rise of the $2P_-$ state.

All the results obtained on the three quenched ensembles are refined by a continuum extrapolation (see Section 4.4.4).

Finally, we come to the static-light meson results which have been obtained on configurations with two flavors of dynamical Chirally Improved fermions. They are displayed in Figure 4.8. Overall, the results for the dynamical configurations are poorer than in the quenched case (Again, this is due to additional fluctuations and increased autocorrelations).

The left plot shows the small but fine lattice, which has already been investigated

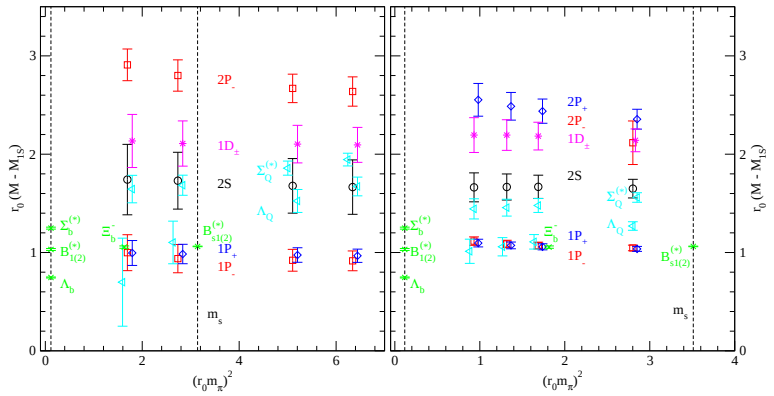

Figure 4.8: Same as in Figure 4.7 but for the configurations with two flavors of dynamical Chirally Improved fermions. The left plot shows the results for the small but fine $12^3 \times 24$ lattice, while the right plot is for the coarser $16^3 \times 32$ lattice with larger physical spatial extent.

in the course of the first tests of our domain decomposition improvement scheme [96]. Here we present newer results, which include also the correlators obtained by the estimate of the light quark propagator over the second boundary and use $t_0 = 3$ instead of $t_0 = 1$ as normalization timeslice for the variational method. It turns out that the effective mass plateau for the previously reported $3S$ state vanishes. On the other hand, the plateau for the $1D_\pm$ is significantly improved such that, after a careful reanalysis, we are able to extract this state for all quark masses. Also the results for the other channels change, especially the statistical errors for the $2S$ have become larger. The reason for this is that we have considered a different fit interval of the eigenvalues. Nevertheless, we are still able to extract mass splittings for a number of states.

The right plot in Figure 4.8, shows our results obtained from our second set of dynamical configurations, which has a larger physical extent of about 2.5fm, but is coarser. Because of larger statistics, the errors are significantly smaller, allowing us to resolve a splitting between the $2S$ and the $1D_\pm$. The $2P_-$ can only be extracted for the largest quark mass. However, we can obtain a first excited P_+ state.

4.4.3 Static-light baryon spectrum

Now we come to the masses of static-light baryons. As for the mesons also here only mass splittings are well-defined quantities. Therefore, we consider only the mass differences between our baryon results and the mass of the $1S$ state of the B mesons.

We start our discussion with the splittings for Λ_b and $\Sigma_b^{(*)}$ obtained on the quenched lattices. They are displayed as triangles in Figure 4.7. The results on the finest lattice (right plot) are obtained only from a subset of our configurations and using only a 2-by-2 cross-correlation matrix, since the computational demand for the calculation on this lattice is significant[4].

In the chiral limit the linear extrapolated splitting for the Λ_b on the coarsest is slightly above the experimental value [87] and becomes even larger on the finer lattices. This may be due to the fact that the static approximation becomes worse on finer lattices, since the motion of the heavy quark is better "resolved". And, as we have discussed above, we use only a subset of the configurations and baryon interpolators on the finest lattice.

Like for the orbitally excited B mesons, we have to compare our extrapolated values for the $\Sigma_b^{(*)}$ with spin averaged experimental values. For that purpose we use $(4M_{\Sigma_b^{*(+,-)}} + 2M_{\Sigma_b^{(+,-)}})/6$. In this case, there is also a simple electromagnetic average over the experimental values [109] of the positive and negative charged particle performed, since we run the charge neutral $\Sigma_b^{(*)0}$, which has not yet been measured. (The electromagnetic effects should only be of the order of a few MeV.) Also the $\Sigma_b^{(*)}$ extrapolates to a value above the so obtained point, when a linear extrapolation in $r_0^2 m_\pi^2$ is used.

Since we have not run any baryons, where the two light quarks have different masses, we cannot really extract results for Ξ_b^- and $\Xi_b^{(\prime,*)}$. However, to get at least an estimate, we interpolate the results for the static-light baryons to a pion mass which corresponds to a quark mass given by $m_q = (m_{ud} + m_s)/2$. In this approximation our results for Ξ_b^- are compatible with the experimental values [110, 111]. The $\Xi_b^{(\prime,*)}$ has not yet been observed experimentally. To obtain the $\Omega_b^{(*)}$, we interpolate the $\Sigma_Q^{(*)}$ to a pion mass which corresponds to strange mass. Also in this case no experimental values are known, yet.

Next, we discuss the dynamical baryon results, which are shown in Figure 4.8. Like in the quenched case, to get the results for Ξ_b^- and $\Xi_b^{(\prime,*)}$, we interpolate to a pion mass which corresponds to the average of light and strange quark masses.

For the smaller lattice our results show rather large statistical errors. As a result the linearly extrapolated Λ_b is compatible with experiment and also the interpolated Ξ_b^- agrees. In the chiral limit, the $\Sigma_b^{(*)}$ lies also for this lattice above the experimental value. On the larger dynamical lattice, the results have certainly improved because of the higher statistics we have for this set.

[4]The computational costs for the baryon correlators are proportional to L^5. This means a factor of approximately thirteen when going from $12^3 \times 24$ to $20^3 \times 40$. An additional complication is given by the fact that the baryon correlators contain two estimated light quark propagators. This means that instead of the N contributions in the meson case we have to compute $N(N-1)/2$ contributions.

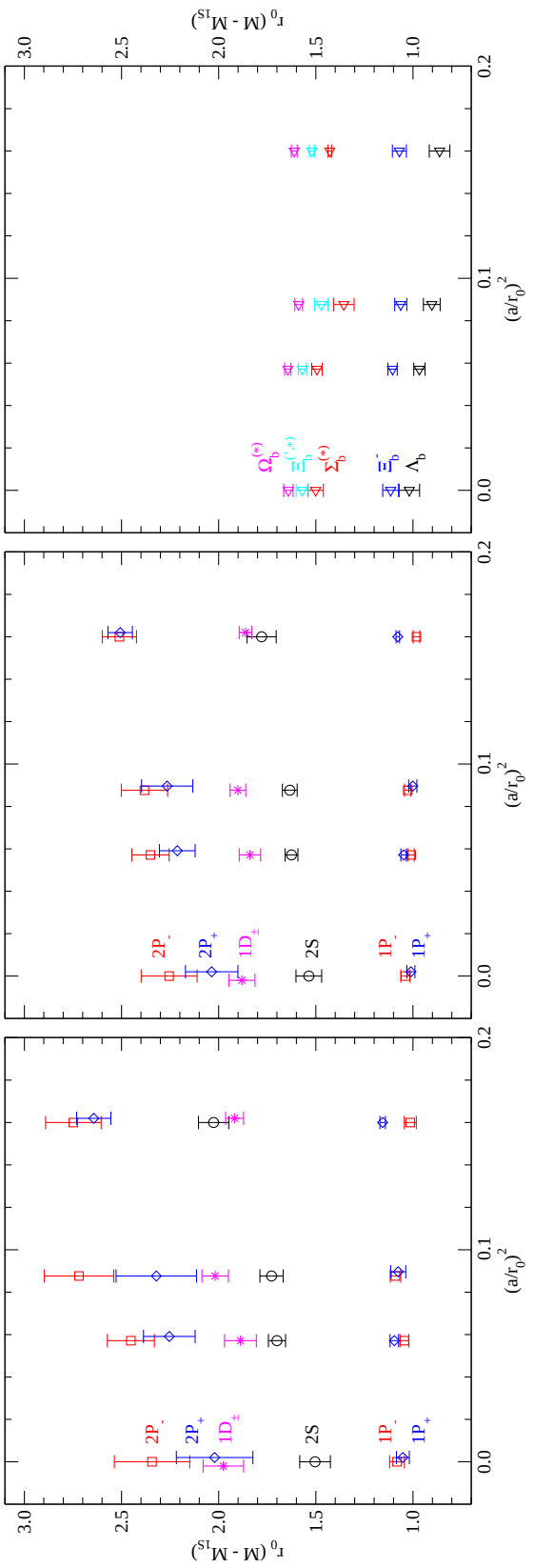

Figure 4.9: Mass splittings for the different lattices as a function of the lattice spacing squared for B_{ud} mesons (left plot), B_s mesons (middle plot) and static-light baryons (right plot). All quantities are in units of the Sommer parameter r_0. The left-most values in each plot are the linearly extrapolated results in the continuum.

4.4.4 Continuum extrapolation

For our quenched results we perform also a continuum extrapolation. For that purpose we plot our chiral extrapolations and interpolations from those lattices as a function of $(a/r_0)^2$ in Figure 4.9. The left-most points in each of the plots are our extrapolation results for which we have performed uncorrelated linear fits. For the mass splittings we assume a^2-scaling since the light quarks are $O(a)$-improved and the static quark propagator is constructed from smeared links. Working with mass differences may improve the situation even more since possible systematic errors might cancel.

The left plot shows our data for the chirally extrapolated static-light mesons. We find nearly perfect scaling for the P-wave ground states and the D-wave. For the excited P-waves and S-wave the continuum is approached with a non-zero slope. This is however mainly due to the results on our coarsest lattice and might hint at discretization errors (see, for example, the $2S$ and $2P_+$ state in Figure 4.9). Even in the continuum limit, we are not able to resolve a splitting for the ground, as well as for the excited, P-wave states. Also the splittings for $2P_+$ and $1D_\pm$ become degenerate.

For the static-strange mesons, which are shown in the middle plot, the scaling of the excited P-waves and the S-wave is better. Again, the largest deviations from a constant behavior are created by the results on the coarsest lattice. Also in this case we perform linear fits for the extrapolation.

In the right plot of Figure 4.9, we present our continuum extrapolations for the static-light baryons. The scaling for these states is not good, especially for the Σ's. This is mainly due to the results on the finest lattice which lie rather high when compared to the results from the two coarser lattices. A possible explanation for this is the fact that for the fine lattice are using only a 2-by-2 cross-correlation matrix.

4.5 Summary

We have presented a new technique for improving estimates of quark propagators. Although the first results for our improved closed contributions are not very promising, it might be that we have chosen a very difficult application (light, disconnected, pseudoscalar correlators) for testing them. Probably they are more useful for other physical quantities.

The improvement we obtain for the estimated half-to-half propagators is significant. As a main test we have done an intensive study of the heavy-light hadron spectrum in the static-light approximation. The boost in statistics from being able to use up to half of the lattice sites as starting locations for our static-light

correlators together with several "tricks" (using two independent estimates and the estimates over the second boundary), that increase the statistics even more, allow us to extract masses for a large number of states. Our results are summarized in Table 4.2 and Table 4.3. In the former one, we present our findings for the static quark combined with u and d quarks, while the latter shows our findings for static-light hadrons which also contain strange quarks.

One observation which we make is the fact that many of the B-mesons splittings seem to be larger than those for the B_s-mesons. This does not agree with experimental results for the P_+ ground state. The difference between the static-strange result and experiment is about 2.5σ, except for the small dynamical lattice which has large statistical errors. A possible explanation is the fact that we are using the static approximation, i.e., the lowest order in HQET, for the heavy quark. Relaxing this approximation by including higher order corrections would probably improve the situation. However, this is numerically much more demanding.

Large deviations are also found between experiment and our quenched results for $(\Lambda_b - B^{(*)})$ and $(\Sigma_b^{(*)} - B^{(*)})$. There the differences are $4 - 4.5$ standard deviations. Using dynamical fermions seem to cure this problem to a certain extent. Especially our results for the larger lattice are just in agreement with the experimental values. It would be interesting if dynamical configurations with lighter sea quarks improved this situation even more. However, it can also be due to larger kinetic corrections for the baryons.

Otherwise, we find rather good agreement with spin-averaged experimental results where known. Any discrepancies are usually on the level of a few percent.

When comparing our findings for the B_s-mesons to the results of other groups [112, 113], we come to the following conclusions: The splittings in [113] are usually smaller than ours for the $2S$, $1P_-$, and $1D_\pm$, except for the $1P_+$, which is consistent with ours. The results with HYP-smearing in [112] for the P-wave ground states are in agreement with our values. For the other mesons our splittings are 10-20% smaller.

Comparing our results for the baryons with the results from other groups [114, 115, 116] is more difficult since these groups relax the static approximation by using non-relativistic and relativistic fermion formulations for the heavy quark. Thus, their results include relativistic effects, which are completely missed in our simulations. These effects may be more important for the baryons since they contain two light quarks and are thus more affected by kinetic corrections.

state	$M - M_{1S}$ [MeV]			
	quenched continuum	$\beta = 5.20$ $La = 1.4$ fm	$\beta = 4.65$ $La = 2.5$ fm	Exp.
$2S$	605(32)	712(139)	674(66)	—
$1P_-$	435(15)	398(78)	454(19)	—
$2P_-$	942(78)	1195(67)	—	—
$1P_+$	423(13)	402(54)	446(17)	423(4)
$2P_+$	812(79)	—	1047(72)	—
$1D_\pm$	794(42)	858(115)	896(78)	—
Λ_b	410(21)	260(142)	358(55)	306(2)
$\Sigma_b^{(*)}$	603(16)	611(58)	554(47)	512(5)

Table 4.2: Mass splittings for the static-light hadrons containing u and d quarks. The number in parentheses is the statistical error. In the last column spin averaged results from experiment [87, 106, 107, 108, 109, 110, 111] are shown.

state	$M - M_{1S}$ [MeV]			
	quenched continuum	$\beta = 5.20$ $La = 1.4$ fm	$\beta = 4.65$ $La = 2.5$ fm	Exp.
$2S$	617(27)	691(125)	661(30)	—
$1P_-$	418(10)	383(59)	410(9)	—
$2P_-$	907(58)	1126(63)	—	—
$1P_+$	406(8)	396(40)	408(8)	436(1)
$2P_+$	818(54)	—	918(31)	—
$1D_\pm$	756(27)	850(93)	852(37)	—
Ξ_b^-	448(16)	362(113)	454(29)	433(5)
$\Xi_b^{(\prime,*)}$	631(12)	651(49)	600(28)	—
$\Omega_b^{(*)}$	660(10)	693(42)	646(12)	—

Table 4.3: Mass splittings the static-light hadrons containing strange quarks. The number in parentheses is the statistical error. In the last column spin averaged results from experiment [87, 106, 107, 108, 109, 110, 111] are shown. The spin averaged splitting for the Ξ_b^- is given by the difference to averaged masses of B and B_s.

Chapter 5

Spectral sums of lattice operators

The phenomenology of QCD is governed by two prominent features, confinement and spontaneous breaking of chiral symmetry. As one increases the temperature T above some critical value T_c, the theory becomes deconfined and chiral symmetry is restored. This suggests that there could be a relation between the two phenomena. Establishing or ruling out such a relation would be a major insight into key mechanisms of QCD.

We begin our discussion with recalling the definition of the chiral condensate Σ. The starting point is the scalar expectation value $\Sigma(m, V)$ of the fermion bilinear $\overline{\psi}\psi$ evaluated at finite volume V and mass m,

$$\Sigma(m,V) = -\int \frac{d^4x}{V} \Big\langle \overline{\psi}(x)\psi(x) \Big\rangle = \frac{1}{V} \Big\langle \mathrm{Tr}\big[(m+D)^{-1}\big] \Big\rangle_G. \tag{5.1}$$

In the second step the fermions are integrated out and the remaining expectation value $\langle ... \rangle_G$ is the path integral over the gauge fields with gauge action and fermion determinant included in the weight factor. D denotes the Dirac operator at vanishing quark mass. We refer to (5.1) as the "quark condensate". The chiral condensate, i.e., the proper order parameter for chiral symmetry breaking is obtained through a double limit, where first the 4-volume V is sent to infinity and then the quark mass m to zero: $\Sigma = \lim_{m\to 0} \lim_{V\to\infty} \Sigma(m, V)$.

The chiral condensate is related to the spectral density of the Dirac operator by the Banks-Casher formula [117]. It relates the chiral condensate to the density $\rho(0)$ of eigenvalues at the origin: $\Sigma = \pi\rho(0)$. Below the critical temperature T_c, where chiral symmetry is broken, the eigenvalue density $\rho(0)$ at the origin is non-vanishing, while above T_c the Dirac spectrum develops a gap, $\rho(0)$ vanishes and with it the chiral condensate (see Fig. 5.1). Chiral symmetry breaking is a feature of full QCD, i.e., massless fermions are taken into account. However, the above discussed mechanism of a non-vanishing spectral density $\rho(0)$ below T_c and a spectral gap above T_c is known to hold also for the quenched case, i.e., pure gauge theory (see, e.g., [118] for a lattice study of this property).

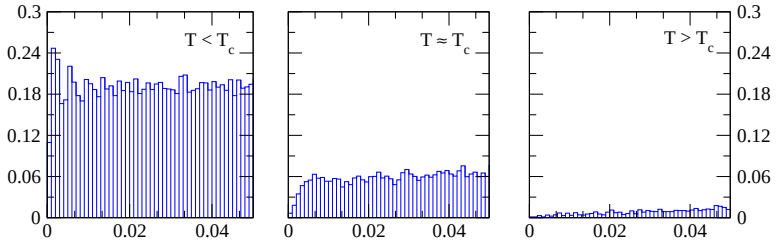

Figure 5.1: Histograms of the spectral density of the staggered lattice Dirac operator as a function of the modulus of the eigenvalues for an ensemble of quenched $SU(3)$ configurations. Below the critical temperature the spectral density at the origin is non-zero. Near T_c the density at the origin decreases and vanishes above the critical temperature.

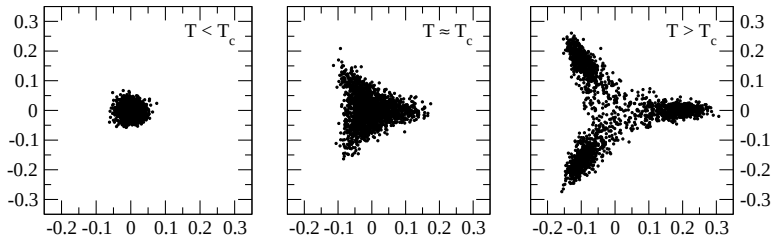

Figure 5.2: Scatter plot for the thin Polyakov loop in the complex plane for an ensemble of quenched $SU(3)$ configurations. As the temperature increases (left to right) the Polyakov loop acquires a non-vanishing expectation value.

On the other hand, the finite temperature transition of pure gauge theory, where the system changes from the confined ($T < T_c$) into the deconfined phase ($T > T_c$), can be understood as spontaneous breaking of the center symmetry [119]. An order parameter for this transition is given by the Polyakov loop

$$P \;=\; \frac{1}{V_3}\sum_{\vec{x}} L(\vec{x}) \quad \text{with} \quad L(\vec{x}) = \mathrm{Tr}_c \left[\prod_{x_4=1}^{N_t} U_4(\vec{x}, x_4) \right] , \tag{5.2}$$

where $L(\vec{x})$ is a straight line of links in the temporal direction closed around the periodic boundary and including a color trace Tr_c. In the following we refer to P as the thin Polyakov loop in order to distinguish it from the dressed Polyakov loop which we define later. Below the critical temperature the expectation value of P vanishes, while above the T_c the thin Polyakov loop clusters at the three values of the center of the group $SU(3)$ (see Fig. 5.2).

In [120], it has been shown that the thin Polyakov loop can be related to spectral sums of differential operators on the lattice, in particular the Dirac and the covariant Laplace operators. In this way also confinement is related to spectral

quantities, as is chiral symmetry breaking through the Banks-Casher formula. Since eigenvalues can be divided into IR and UV regions in a natural way, the spectral representations allow one to analyze whether confinement is dominated by IR or UV modes.

First numerical studies [121, 122] in the quenched approximation have shown that the biggest contributions to the spectral sums for thin Polyakov loops are coming from the UV modes of the Dirac spectrum. Similar findings have been reported for dynamical fermions [123]. In Section 5.1, we present the derivation of the spectral sums for thin Polyakov loops and the results of our numerical studies.

In [124] also other quantities (propagators and heat kernels) serving as order parameter for phase transition have been investigated. We build on those results and the ones we have obtained for the thin Polyakov loop and define a new order parameter, the dressed Polyakov loop, which intimately connects with the quark condensate through a Fourier transform with respect to a U(1)-valued temporal boundary condition. In Section 5.2, we present first results for this interesting connection, published in [125].

Recently, also first results for correlators of spectral sums have been published [126, 127].

5.1 Spectral sums for thin Polyakov loops

5.1.1 Derivation of the spectral sums

In order to connect the thin Polyakov loop to spectral sums we follow the derivation in [120]. We consider powers of the staggered Dirac operator (2.40). Although not used here, we like to stress that our method can be easily generalized to the lattice Laplace operator and presumably also other (more chiral) lattice Dirac operators.

The n-th power of the Dirac operator then contains paths up to length n, dressed with a product of n links. For the special case where we consider the operator to the power N_t, where N_t is the time extent of our lattice, we obtain

$$\begin{aligned} \mathrm{Tr}_c D^{N_t}(x,x) &= \frac{1}{2^{N_t}} \mathrm{Tr}_c \prod_{s=1}^{N_t} U_4(\vec{x},s) - \frac{1}{2^{N_t}} \mathrm{Tr}_c \prod_{s=0}^{N_t-1} U_4(\vec{x},N_t-s)^\dagger \\ &+ \text{ other loops, trivially closed} \qquad (5.3) \\ &= \frac{1}{2^{N_t}} \big[L(\vec{x}) - L^*(\vec{x}) \big] + \text{ other loops, trivially closed.} \qquad (5.4) \end{aligned}$$

From the set of all loops that contribute we have singled out the thin Polyakov loop and its complex conjugate. These two straight loops are the only ones that can close around compactified time. All others are 'trivially closed', i.e., they do not wrap around the lattice in temporal direction and in the continuum can be shrinked to zero size.

The key observation is that a change of the temporal boundary conditions for the fermions

$$\psi(\vec{x}, T) = z\,\psi(\vec{x}, 0), \tag{5.5}$$

where $z = e^{i\varphi}$ is a complex phase, can be absorbed in the temporal links as

$$U_4(\vec{x}, N_t) \;\rightarrow\; z\,U_4(\vec{x}, N_t)\;, \quad |z| = 1\;, \tag{5.6}$$

and that this only affects the Polyakov loops

$$L \;\longrightarrow\; z\,L\;, \quad L^* \;\longrightarrow\; z^*\,L^*\;, \tag{5.7}$$

while the trivially closed loops remain unchanged. After such a change the expression (5.4) reads

$$\mathrm{Tr}_c D_z^{N_t}(x,x) \;=\; \frac{1}{2^{N_t}}\big[\, zL(\vec{x}) \;-\; z^*L^*(\vec{x})\,\big] \;+\; \text{other loops}, \tag{5.8}$$

where D_z is the Dirac operator on a configuration where the temporal boundary conditions are changed by a factor z. Averaging this expression over space and time we obtain

$$\mathrm{Tr}\; D_z^{N_t} \;=\; \frac{V_4}{2^{N_t}}(zP - z^*P^* + X)\;, \tag{5.9}$$

where X is the sum of all trivially closed paths and Tr denotes the trace over all indices. We make use of this behavior to cancel the unwanted trivial contributions X and project onto the thin Polyakov loop by taking linear combinations (coefficients a_i) of this expression for three different boundary conditions z_1, z_2 and z_3

$$\begin{aligned} P \;&\stackrel{!}{=}\; 2^{N_t}\sum_{i=1}^{3} a_i \mathrm{Tr}\,(D_{z_i}^{N_t}) \\ &=\; P\,\underbrace{(z_1a_1 + z_2a_2 + z_3a_3)}_{\stackrel{!}{=}1} - P^*\,\underbrace{(z_1^*a_1 + z_2^*a_2 + z_3^*a_3)}_{\stackrel{!}{=}0} + X\,\underbrace{(a_1 + a_2 + a_3)}_{\stackrel{!}{=}0}\;. \end{aligned} \tag{5.10}$$

This leads to a set of linear equations for the coefficients a_1, a_2 and a_3

$$\begin{pmatrix} z_1 & z_2 & z_3 \\ z_1^* & z_2^* & z_3^* \\ 1 & 1 & 1 \end{pmatrix} \begin{pmatrix} a_1 \\ a_2 \\ a_3 \end{pmatrix} \;=\; \begin{pmatrix} 1 \\ 0 \\ 0 \end{pmatrix}. \tag{5.11}$$

One can show that this equation has a unique solution as long as the boundary conditions z_1, z_2 and z_3 are different. For the particular choice $z_1 = 1$ and $z_2 = z_3^* = e^{i\frac{2\pi}{3}} \equiv z$ the thin Polyakov loop is then given by

$$P \;=\; \frac{2^{N_t}}{V_4}\left[\sum_i \left(\lambda^{(i)}\right)^{N_t} + z^* \sum_i \left(\lambda_z^{(i)}\right)^{N_t} + z \sum_i \left(\lambda_{z^*}^{(i)}\right)^{N_t}\right] , \tag{5.12}$$

where the $\lambda_z^{(i)}$ are the eigenvalues of the staggered Dirac operator for a given boundary condition z. Similar expressions can be obtained for other differential operators on the lattice, e.g., the lattice Laplace operator.

We stress that the results (5.12) is an exact formula for the thin Polyakov loop of an arbitrary configuration. Below we study numerically the expectation value $\langle P \rangle$ of the thin Polyakov loop on a number of quenched ensembles. Then the above formula relates the vacuum expectation value of the thin Polyakov loop to the expectation values of the N_t-th moments of the Dirac eigenvalues computed with three different boundary conditions.

5.1.2 Numerical results

In our numerical study of Eq. (5.12), we use quenched gauge configurations generated using the Lüscher-Weisz gauge action on lattice with different sizes ranging from $6^3 \times 4$ up to $12^3 \times 6$ at temperatures below and above the critical value $T_c \approx 300$ MeV. We also adjust the values of the inverse coupling in such a way that for the different temporal extents the temperature are approximately the same. The lattice spacing is set [128] using the Sommer parameter $r_0 = 0.5$ fm. More information about the lattices can be found in Appendix H.

On each of the configurations, we use LAPACK to compute the complete spectrum of the staggered Dirac operator (2.40) for the different boundary conditions $z_1 = 1$, $z_2 = z_3^* = e^{i\frac{2\pi}{3}} \equiv z$ which are used to derive the spectral sum (5.12). For the smallest lattice we use 2000 configuration but since the computational costs for calculating the eigenvalues grows strongly with the number of sites, we are limited to only 20 configurations for our larger lattices. After computing all eigenvalues of the staggered Dirac operators we order them with respect to their absolute value and organize them in bins. For each bin we calculate a number of observables. All error bars we show are statistical errors determined with single elimination jackknife.

The first observable is the distribution of the eigenvalues, which we show in Figure 5.3 for different spatial and temporal extents of the lattice and for three different temperatures above, below and approximately at the critical value T_c. The left hand side set of those plots shows the distribution as a function of the size of the eigenvalues in lattice units, while the plots on the right hand side are

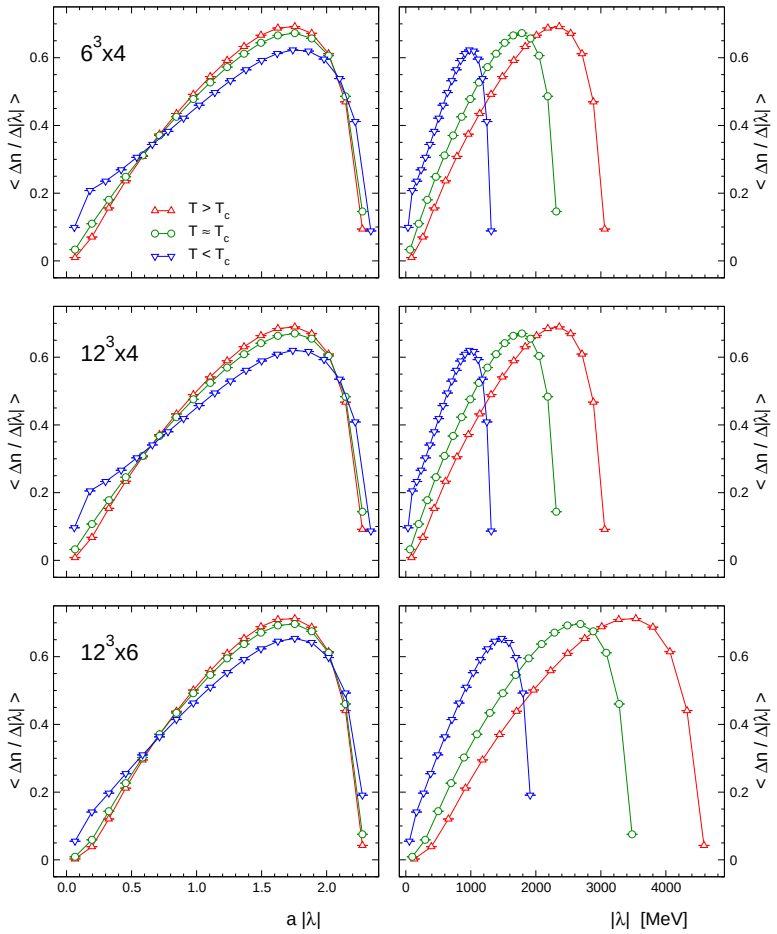

Figure 5.3: Distribution of the eigenvalues of the staggered Dirac operator for different lattices and different temperatures. The l.h.s. plots are in lattice units, while on the r.h.s. we use MeV. The values of the temperatures are 140 MeV, 254 MeV, and 337 MeV.

in MeV. When we use physical units on the horizontal scale, the densities are stretched with different factors due to different lattice spacings for the couplings we use.

One can clearly see that at small $|\lambda|$ the spectral density at the origin vanishes and chiral symmetry is restored as one increases the temperature above the critical value. The density of eigenvalues reaches a maximum after about three quarters of the eigenvalues and then quickly drops towards the UV cutoff.

We observe a light enhancement of the density near the maximum for $T > T_c$. The reason for this is that the area under the curves has to be equal for the three temperatures since it represents the total number of eigenvalues. When the temperature is increased the density is depleted at the origin but enhanced at

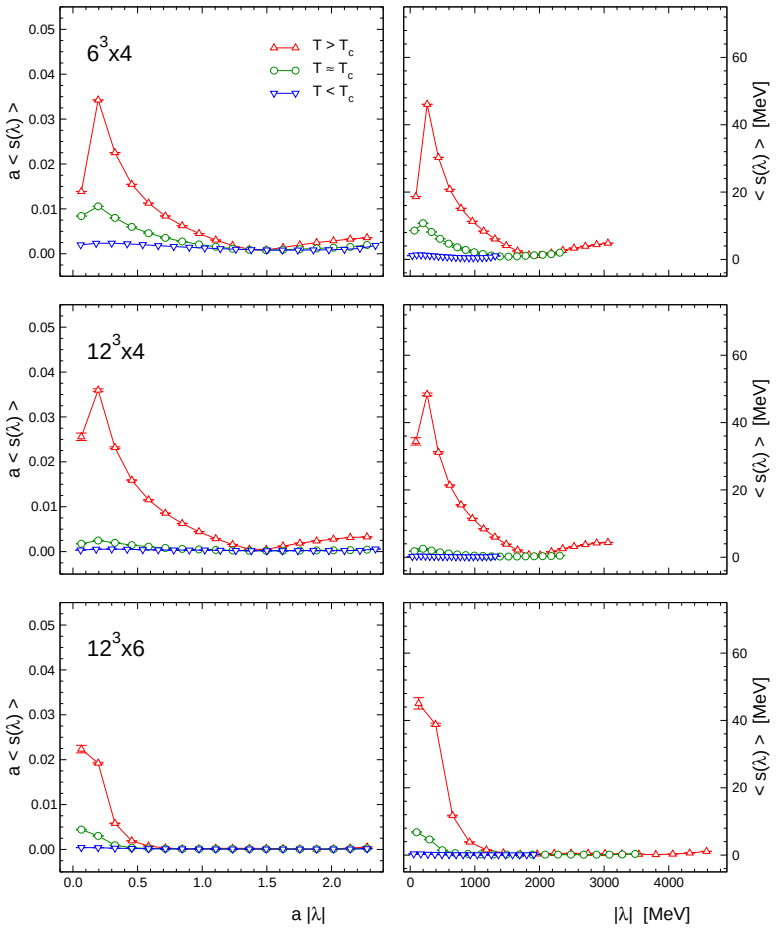

Figure 5.4: Average shift of the eigenvalues calculated as defined in Equation (5.13) as a function of λ. Again we use lattice units in the l.h.s. set of plots and MeV on the r.h.s. The individual data points are obtained by averaging over all eigenvalues in a bin and then over all configurations in the ensemble.

larger values of $|\lambda|$.

Figure 5.3 is particularly important when one analyzes which part of the spectrum contributes to the spectral sum (5.12) for the thin Polyakov loop. Energy ranges where the density of eigenvalues is large will in general be more important than those parts of the spectrum with a low density.

In the spectral sum (5.12) the thin Polyakov loop emerges through a relocation of the eigenvalues as the boundary condition is changed. It is interesting to analyze how strongly different eigenvalues of the spectrum respond when the boundary condition is changed. We quantify this question by studying the averaged shift

$s(\lambda^{(i)})$ of the eigenvalues given by

$$s(\lambda^{(i)}) \;=\; \left(|\lambda^{(i)} - \lambda_z^{(i)}| \,+\, |\lambda^{(i)} - \lambda_{z^*}^{(i)}| \,+\, |\lambda_z^{(i)} - \lambda_{z^*}^{(i)}|\right)/3\,, \tag{5.13}$$

where we compare an eigenvalue $\lambda^{(i)}$ for periodic boundary conditions to its partners $\lambda_z^{(i)}$ and $\lambda_{z^*}^{(i)}$, computed with z- and z^*-boundary conditions. Since above the phase transition the thin Polyakov loop obtains a finite value while in the confined phase it is approximately zero, the shift of the eigenvalues should change as one increases the temperature. This is exactly what we find in our results for the average shift $s(\lambda)$ presented in Figure 5.4.

The most obvious feature of the plots is the fact that the shift of the eigenvalues is considerably larger for $T > T_c$, especially at the IR end of the spectrum. This confirms an observation made in [118, 129], where it was shown, that above the critical temperature the size of the spectral gap strongly depends on the fermionic boundary condition. In the Section 5.2 we find that this property plays also an important role for dressed Polyakov loops. The plots furthermore show, that below the critical temperature the shifts of the eigenvalues are almost zero over the whole spectrum basically leading to complete cancellations in the spectral sum (5.12) and thus to a vanishing thin Polyakov loop.

After understanding the global distribution of the eigenvalues and their shift under a change of the boundary conditions, we can start to analyze the individual contributions to the spectral sum (5.12). This individual contribution is given by

$$c(\lambda^{(i)}) \;=\; \frac{2^{N_t}}{V_4}\left[\left(\lambda^{(i)}\right)^{N_t} \,+\, z^*\left(\lambda_z^{(i)}\right)^{N_t} \,+\, z\left(\lambda_{z^*}^{(i)}\right)^{N_t}\right]\,, \tag{5.14}$$

and averaged in each bin.

Our results are shown in Figure 5.5, where we plot the absolute value of the individual contributions after normalizing them with P, i.e., we divide by the value of the thin Polyakov loop. From that figure, we find that mainly the UV modes contribute to the thin Polyakov loop. Our observation is essentially independent of the temperature and the size of the lattice. This finding is not a-priori expected, given the fact that it is the IR modes that show the largest shifts in Figure 5.4. On the other hand, the large power N_t in the spectral sum (5.12) drastically enhances the contributions of the UV eigenvalues.

Interesting are also the dips which form with increasing temperature at about $1.5a$ for $N_t = 4$ and at $0.8a$ and $1.9a$ for $N_t = 6$. It can be shown that these dips are correlated to the relocation of the eigenvalues as the temporal boundary condition is changed. While the eigenvalues below a dips are shifted in one direction, the ones above are moved into the other direction. When N_t is increased, the number of points where this change happened is also increased, and the spectrum starts to exhibit an "accordion"-like structure.

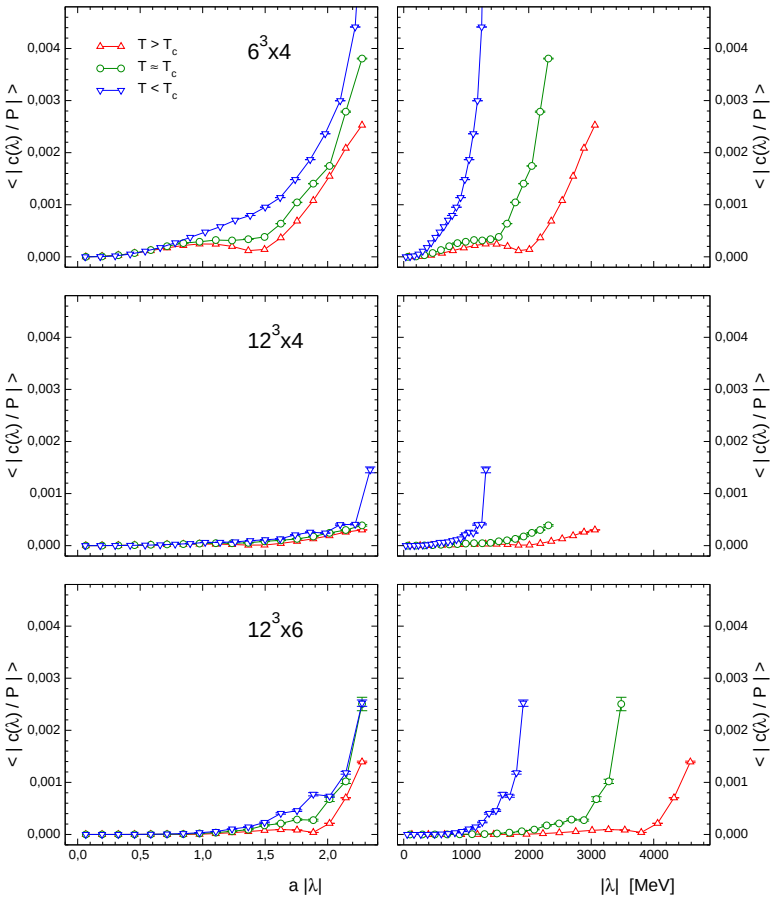

Figure 5.5: Contribution (5.14) of individual eigenvalues to the spectral sum for the thin Polyakov loop given by Equation (5.12). As before we use lattice units in the l.h.s. set of plots and MeV on the r.h.s.

The plot in Figure 5.5 shows that the individual contributions are biggest at the UV end of the spectrum. On the other hand, from Figure 5.3 we have found that for the largest eigenvalues the density drastically drops. It is an interesting question which effect, size of contribution versus density, wins out. This question can be addressed by considering partial sums of (5.12).

In Figure 5.6, we present such partial sums as a function of the cutoff, i.e., as a function of the largest eigenvalue included in (5.12). Again we divide by the Polyakov loop P, such that when all eigenvalues are summed, i.e., at the largest value of λ in Figure 5.6, the curve approaches 1.0 to machine precision. This is a good check that the exact formulas are implemented correctly.

For the $6^3 \times 4$ and $12^3 \times 4$ lattices, we find that the contributions from the largest eigenvalues are needed to recover the complete thin Polyakov loop. This is consistent with the observations we make for the individual contributions in

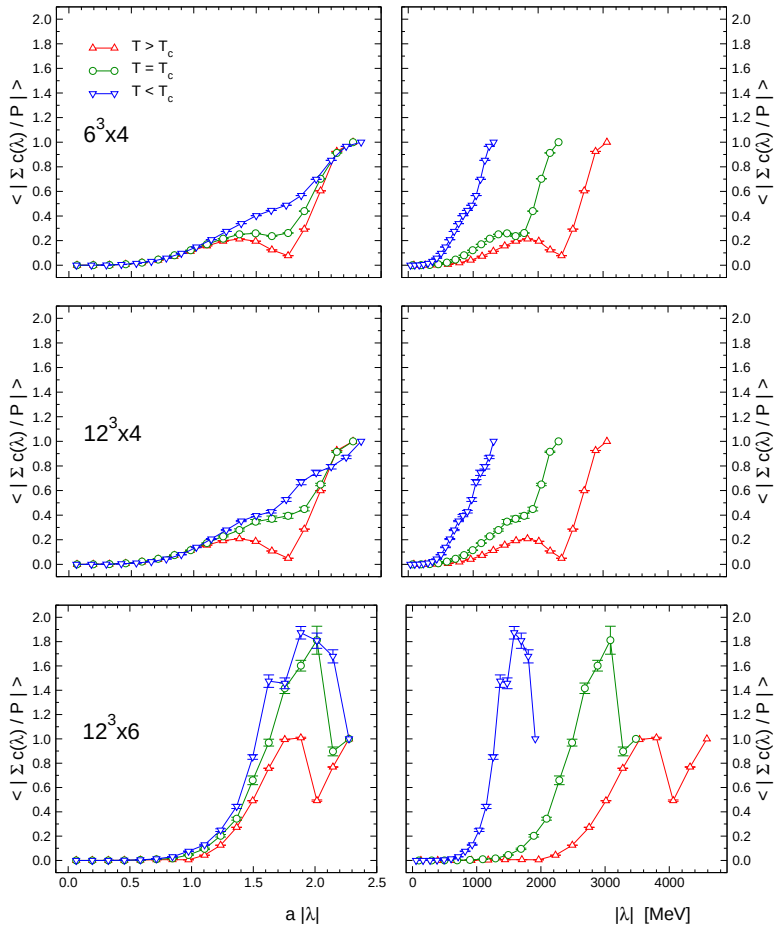

Figure 5.6: Partial sums of the spectral formula (5.12), plotted as a function of the cutoff.

Figure 5.5.

For the $12^3 \times 6$ lattice, we find that for medium temperatures the partial sums overshoot by nearly a factor of two before they reach the correct value at the largest values of λ. Thus the behavior of the partial sums is non-monotonic (the overshooting is not problematic, the thin Polyakov loop should vanish and indeed the accumulated contributions stay approximately zero over the whole range of the spectrum). We also find that the thin Polyakov loop is recovered only after all UV modes are included in the spectral sum. Another very interesting feature is that for $T > T_c$ the accumulated contributions in Figure 5.6 exhibit local maxima approximately at the points where we have found dips in Figure 5.5.

So far we have only considered absolute values of quantities. However, the Polyakov loop and also the spectral sums are complex numbers and we can analyze their relative phase, too. In Figure 5.7, we plot partially reconstructed thin

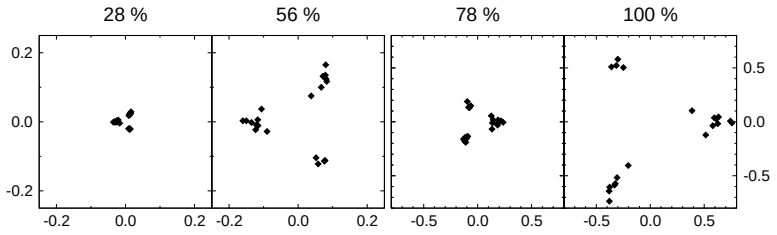

Figure 5.7: The Polyakov loop in the complex plane for 20 configurations above T_c for the $6^3 \times 4$ lattice as reconstructed from the spectral sums with 28%, 56%, 78% and 100% of the eigenvalues (left to right). Note that the two plots on the l.h.s. have a different scale.

Polyakov loops for the $6^3 \times 4$ lattice above the critical temperature. When using less than approximately 75% of the eigenvalues, we find a relative phase of 180 degrees between the truncated sums and the thin Polyakov loop. To quantify this observation we plot the angle $\Delta\phi$ between the truncated sums and the resulting thin Polyakov loop as a function of the cutoff used in the truncated sum in Figure 5.8. We show data for a $12^3 \times 4$ and a $12^3 \times 6$ lattice, both at $T > T_c$. We find that on the former lattice the accumulated contributions start with the wrong sign and recover the correct sign at the end. On the other lattice, although starting and ending with the correct sign, there is an intermediate region in which the truncated sum has the wrong sign. A comparison with lattices of different spatial size but same temporal extent reveals that this behavior depends only on the temporal extent.

An explanation for this phenomenon is the fact that the eigenvalues λ of the staggered Dirac operator are purely imaginary. Thus λ^{4n} is a real positive number, while λ^{4n+2} is real but negative, for $n \in \mathbb{N}$. As we are looking at the relative phases, we restrict ourselves to approximately real Polyakov loops for the moment. If we consider only the lowest term in the truncated sum we find:

$$\begin{aligned} c(\lambda^{(1)}) &= \frac{2^{N_t}}{V_4}\left[\left(\lambda^{(1)}\right)^{N_t} + z^*\left(\lambda_z^{(1)}\right)^{N_t} + z\left(\lambda_{z^*}^{(1)}\right)^{N_t}\right] \\ &= \frac{2^{N_t}}{V_4}\left[\alpha + z^*\tilde{\alpha}_z + z\tilde{\alpha}_{z^*}\right] \overset{\tilde{\alpha}_{z^*}\approx\tilde{\alpha}_z\equiv\tilde{\alpha}}{=} \frac{2^{N_t}}{V_4}\left[\alpha + (z^*+z)\tilde{\alpha}\right] \\ &= \frac{2^{N_t}}{V_4}\left[\alpha - \tilde{\alpha}\right]\begin{cases} < 0 & N_t = 4n \\ > 0 & N_t = 4n+2 \end{cases} \begin{array}{l} \text{as } \alpha, \tilde{\alpha} > 0 \\ \text{as } \alpha, \tilde{\alpha} < 0 \end{array}, \; |\tilde{\alpha}| > |\alpha|\,, \end{aligned} \tag{5.15}$$

where we assume that the boundary conditions with phases z and z^* lead to approximately the same lowest eigenvalue $\tilde{\alpha}$, which is larger in size than the eigenvalue α at periodic boundary conditions [124]. The boundaries "twist" the eigenvalues. Interestingly, this last relation between the relative sizes of the eigenvalues for non-trivial and periodic boundary conditions seems to change

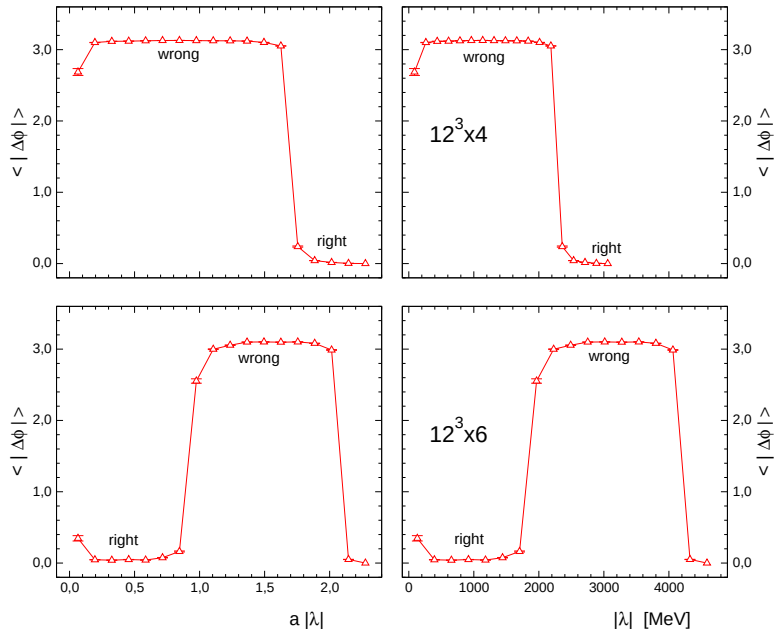

Figure 5.8: Phase shift of the truncated sums relative to the thin Polyakov loop for $T > T_c$. The upper plots are for a $12^3 \times 4$ lattice, while the lower plots are for $12^3 \times 6$.

in certain regions in the spectrum of the staggered Dirac operator, leading to the accordion-like structure, and thus creating the observed sign change in the truncated sums. The points where these sign changes occur depend only on the time extent of the lattice.

In a similar way, one can also explain why the thin Polyakov loop vanishes at low temperatures:

$$\begin{aligned} P &= \frac{2^{N_t}}{V_4}\left[\sum_i \left(\lambda^{(i)}\right)^{N_t} + z^* \sum_i \left(\lambda_z^{(i)}\right)^{N_t} + z \sum_i \left(\lambda_{z^*}^{(i)}\right)^{N_t}\right] \\ &\approx \frac{2^{N_t}}{V_4}\left[\sum_i \left(\lambda^{(i)}\right)^{N_t}\right](1 + z^* + z) = 0, \end{aligned} \tag{5.16}$$

where we have used that the shift is nearly zero below the critical temperature and thus $\lambda^{(i)} \approx \lambda_{z^*}^{(i)} \approx \lambda_z^{(i)}$.

5.1.3 Summary

We have given a representation of the thin Polyakov loop as a spectral sum of (staggered) Dirac eigenvalues with different boundary conditions. For our

numerical studies of this relation we have computed complete spectra of the staggered Dirac operator for different fermionic boundary conditions. We have used quenched ensembles below, above and approximately at the confinement-deconfinement phase transition. To study systematic effects, we have considered different spatial volumes and also different extents of the lattice in time direction. We have considered different aspects of the spectra, in particular the distribution of the eigenvalues and their shift under a change of the fermionic boundary conditions. Concerning this shift, we established that above that critical temperature the IR modes are shifted most while below T_c the shift is approximately zero for all eigenvalues.

However, when inspecting how the eigenvalues reconstruct the thin Polyakov loop we find relative phase shifts of 180 degrees between the thin Polyakov loop and the partials sums. Where and how many of these shifts occur depends only on the temporal extent of the lattice. The very fact that the partially reconstructed Polyakov loop already obtains a non-vanishing expectation value might be viewed as a signal for the breaking of center symmetry. Thus, the lowest-lying eigenvalues know about the deconfinement phase transition.

Our study shows that working with the thin Polyakov loop also has some drawbacks. Actually it is a very local object and thus has bad renormalization properties. We find that one needs a large number of eigenvalues, more than 75%, to restore a significant amount of the thin Polyakov loop. Especially the UV modes enter with sizable contributions. Another problem comes from the phase shifts between the truncated sums and the completely restored Polyakov loop. Since these shifts are depending on the temporal extent of the lattice, one might consider that they are pure lattice artifacts.

These properties make the thin loop less attractive for finding a connection between the spontaneous breaking of chiral symmetry and confinement. In the next section we therefore propose a new order parameter for the confinement-deconfinement transition: the dressed Polyakov loop.

5.2 Spectral sums for dressed Polyakov loops

5.2.1 Dual quark condensate and dressed Polyakov loops

We start our discussion of dressed Polyakov loops with defining the *dual quark condensate* which we later identify as an order parameter for center symmetry. We work in a finite Euclidean volume with temporal extent $N_t a = 1/k_B T$. For the fermion fields ψ we use the same generalized boundary conditions (5.5) as in the previous section.

The quark condensate (5.1) is considered for an arbitrary boundary angle φ indicated by a subscript for the Dirac operator. The "dual quark condensate" $\widetilde{\Sigma}_n$ is defined as the Fourier transform with respect to φ,

$$\widetilde{\Sigma}_n(m,V) \;=\; \int_0^{2\pi} \frac{d\varphi}{2\pi}\, \frac{e^{-i\varphi n}}{V} \left\langle \mathrm{Tr}\left[(m+D_\varphi)^{-1}\right] \right\rangle_G, \tag{5.17}$$

where the index n is an integer and D_φ is a massless Dirac operator evaluated for a temporal boundary condition $e^{i\varphi}$. For this gauge invariant quantity the case $n = 1$ is especially interesting because it can be related to an observable which we call dressed Polyakov loop. To derive this relation we again consider the staggered lattice Dirac operator (2.40). However, we stress that the following argumentation can easily be modified to hold also for other lattice derivative operators.

As discussed in the previous section, the $U(1)$-valued temporal fermionic boundary conditions are most conveniently introduced by attaching the boundary phase to the temporal link on the last timeslice, $U_4(\vec{x}, N_4) \to e^{i\varphi}\, U_4(\vec{x}, N_4)$. Inserting this into the Dirac operator, we evaluate the propagator in (5.17) for sufficiently large m as a geometric series

$$\mathrm{Tr}\left[(m+D_\varphi)^{-1}\right] \;=\; \frac{1}{m}\sum_{k=0}^{\infty} \frac{(-1)^k}{m^k} \mathrm{Tr}\left[(D_\varphi)^k\right] \;. \tag{5.18}$$

As the staggered Dirac operator contains only terms that connect nearest neighbors, the power $(D_\varphi)^k$ on the r.h.s. corresponds to a chain of k hops. The trace in (5.18) is over color- and space-time indices. The latter trace implies that the chains of hops have to form closed loops l (thus on a lattice with even numbers of sites in all directions k must be even). Consequently, the sum in (5.18) can be reexpressed as a sum over the set $\mathcal{L}$ of all possible closed loops on the lattice,

$$\mathrm{Tr}\left[(m+D_\varphi)^{-1}\right] = \frac{1}{m}\sum_{l\in\mathcal{L}} \frac{s(l)e^{i\varphi q(l)}}{(2am)^{|l|}}\, \mathrm{Tr}_c \prod_{(x,\mu)\in l} U_\mu(x). \tag{5.19}$$

The remaining trace Tr_c is over the color indices of the ordered product of all link variables $U_\mu(x)$ in a loop l, and we use $U_{-\mu}(x) = U_\mu(x-a\hat{\mu})^\dagger$. By $s(l)$ we denote the sign of a particular loop l which is obtained as a product of the staggered sign factors. Each step in the loop comes with a factor of $1/2am$ from the discretization in (2.40) and the normalization in (5.18). The number of steps, i.e., the length of the loop is denoted by $|l|$.

The loops may close around the boundaries. When they close around the temporal boundary, they pick up a factor of $\exp(i\varphi)$ if they run forward in time, and a factor of $\exp(-i\varphi)$ for backward running. Denoting the number of times a loop l winds around the compact time direction by its winding number $q(l) \in \mathbb{Z}$, we

obtain the factor $\exp(i\varphi q(l))$ in (5.19). This is how the boundary angle φ distinguishes between closed loops of different winding number in the representation of the propagator.

When expression (5.19) is inserted into the formula (5.17) for the dual condensate, the φ-integration with the additional Fourier factor $\exp(-i\varphi n)$ projects to loops of a particular winding number n. We finally obtain

$$\widetilde{\Sigma}_n(m,V) = \frac{1}{Vm} \sum_{l\in\mathcal{L}(n)} \frac{s(l)}{(2am)^{|l|}} \left\langle \mathrm{Tr}_c \prod_{(x,\mu)\in l} U_\mu(x) \right\rangle_G , \tag{5.20}$$

where the sum now runs over the set $\mathcal{L}(n)$ of loops that wind n times around the compact time direction. The case of $n = 1$, i.e., the dual condensate $\widetilde{\Sigma}_1(m,V)$ which corresponds to loops that wind exactly once, is what we refer to as the "dressed Polyakov loop". From (5.20) it is obvious that in the large-m limit the dominant contribution is the conventional thin Polyakov loop because it is the shortest loop winding once around the lattice in temporal direction.

Before we present the results of our numerical investigation of the dressed Polyakov loop, we discuss the behavior of the dual condensates under a center transformation, $U_4(\vec{x},t_0) \to z\,U_4(\vec{x},t_0)$, where all temporal links on a timeslice, i.e., at some fixed t_0, are multiplied with an element z of the center of the gauge group. The gauge action and the measure are invariant under this transformation, but the center symmetry is broken spontaneously at the critical temperature T_c, signaling the transition to the deconfined phase. The conventional thin Polyakov loop is an order parameter for the center symmetry and the same is true for the dressed Polyakov loop. More generally a loop that winds n times around the compact time direction picks up a net factor of z^n and thus our dual condensates transform under a center transformation as $\widetilde{\Sigma}_n \to z^n\widetilde{\Sigma}_n$. In particular the dressed Polyakov loop, i.e., the dual condensate for $n = 1$, transforms as $\widetilde{\Sigma}_1 \to z\widetilde{\Sigma}_1$, which is the same transformation law as for the thin Polyakov loop.

5.2.2 Numerical results

For our numerical investigation of the dressed Polyakov loops, we express the dual condensate (5.17) is as a spectral sum over all Dirac eigenvalues $\lambda_\varphi^{(i)}$ (again evaluated for boundary angle φ),

$$\widetilde{\Sigma}_n(m,V) = \int_0^{2\pi} \frac{d\varphi}{2\pi}\, \frac{e^{-i\varphi n}}{V} \sum_i \left\langle \left(m + \lambda_\varphi^{(i)}\right)^{-1} \right\rangle_G . \tag{5.21}$$

First of all this spectral representation consists of a finite sum over the eigenvalues (due to the regularization on a finite lattice), whereas the representation (5.20) contains an infinite sum over loops (even on a finite lattice).

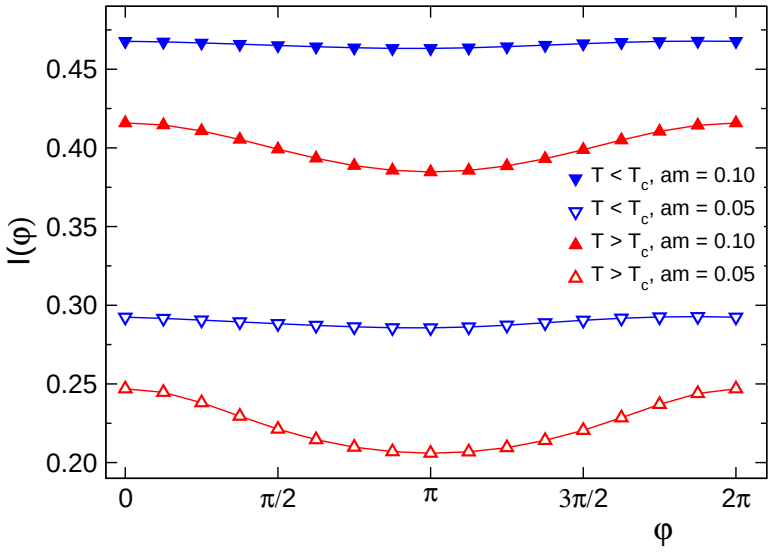

Figure 5.9: The integrand $I(\varphi) = V^{-1} \sum_i \left\langle (m + \lambda_\varphi^{(i)})^{-1} \right\rangle_G$ of (5.21) in lattice units for two values of am. The data are from 20 gauge configurations on $12^3 \times 6$ lattices below ($T = 255$ MeV, $a = 0.129$ fm) and above T_c ($T = 337$ MeV, $a = 0.098$ fm).

Secondly, the sum on the r.h.s. of (5.21) can easily be computed numerically and then allows to study the role of individual parts of the spectrum as for the thin Polyakov loop. Since the (purely imaginary) eigenvalues appear in the denominator, we expect the dual condensate to be dominated by IR modes (at least for small mass m) and thus to have a well-defined continuum limit, both in contrast to traces over the N_t-th power of D used in the previous section.

For our numerical analysis of the spectral representation (5.21) we again compute complete spectra of the staggered Dirac operator (2.40) at different boundary angles φ with parallel LAPACK routines. Like for the thin Polyakov loops we use quenched $SU(3)$ gauge configurations generated from the Lüscher-Weisz gauge action and determine the scale with the Sommer parameter, setting $r_0 = 0.5$ fm. We use $L^3 \times N_4$ lattices with L ranging from 8 to 14 and N_4 from 4 to 8, and adjust the couplings such that we have ensembles below and above the critical temperature $T_c \sim 300$ MeV. For the gauge configurations above T_c we check that the thin Polyakov loop has a non-vanishing expectation value and for our numerical study we limit ourselves to configurations where the thin Polyakov loop is real. Later we discuss how the spectral sum for the dressed Polyakov loop may generate also the two possible complex phases. Again, all errors shown are statistical errors from the single elimination Jackknife method.

We begin with analyzing the φ-dependence of the integrand in (5.21). In Figure 5.9 we plot this integrand as a function of φ for two values of am comparing an

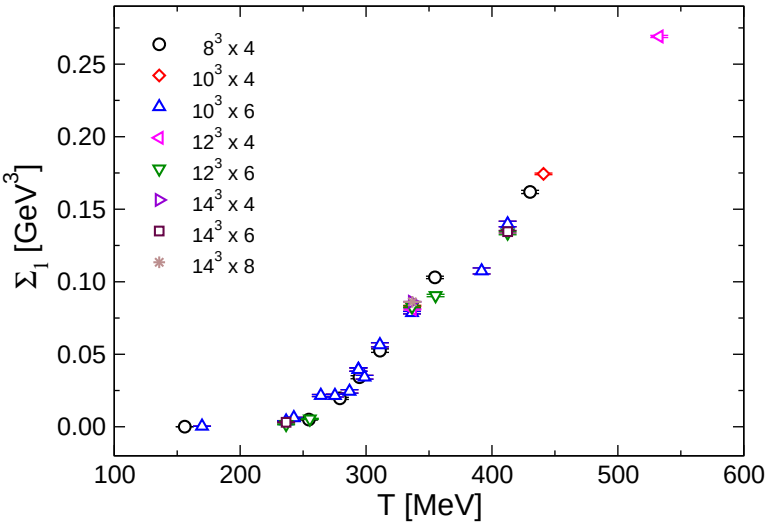

Figure 5.10: The dressed Polyakov loop at $m = 100$ MeV in units of GeV^3 as a function of the temperature T in MeV.

ensemble below T_c to one above T_c. It is obvious that below T_c the integrand is essentially constant, while above T_c it shows a pronounced cosine type of behavior. Integrating over φ with the weight $\exp(-i\varphi)$, we find that the dressed Polyakov vanishes below T_c, while above T_c a non-vanishing value is observed. We conclude that the transition from confinement to deconfinement leads to a different response of the spectral sums to the changing temporal fermion boundary conditions. Below we will demonstrate that the IR modes play the dominant role in this process.

Above T_c, instead of an ensemble with real thin Polyakov loops, one can also use configurations where the thin Polyakov loop has one of the two complex phases. Then the integrand is shifted by $\pm 2\pi/3$, but otherwise has the same form as depicted in Figure 5.9. Integrating this shifted integrand shows that the dressed Polyakov loop produces the same $\mathbb{Z}_3$ phase pattern as the thin one.

Now we demonstrate that the dressed Polyakov loop does indeed signal the phase transition. In Figure 5.10, we show the results for the dressed Polyakov loop at $m = 100$ MeV as a function of T. The necessary φ-integration was implemented with the extended Simpson rule using typically 8 or 16 values of φ. It is obvious that below T_c the dressed Polyakov loop vanishes, while above T_c it assumes a non-vanishing value, signaling that the center symmetry is broken in the deconfined phase.

Let us now consider the individual contributions $C(\lambda) = (2\pi V)^{-1} \int d\varphi \exp(-i\varphi) \left\langle (m + \lambda_\varphi)^{-1} \right\rangle_G$ to the spectral sum (5.21). The upper plots of Figure 5.11 show $|C(\lambda)/\widetilde{\Sigma}_1|$ as a function of $|\lambda|$. Since the case of vanishing quark mass m can be

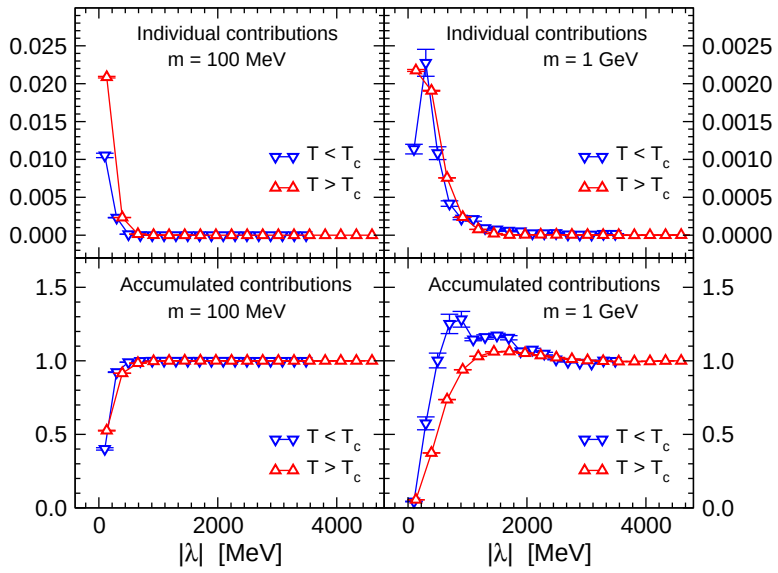

Figure 5.11: The upper plots show the (normalized) individual contributions $|C(|\lambda|)/\widetilde{\Sigma}_1|$ to (5.21) versus $|\lambda|$ for two values of m, while the lower plots are the normalized accumulated contributions $|A(|\lambda|)/\widetilde{\Sigma}_1|$ as a function of $|\lambda|$. The data are from the same ensembles already used in Figure 5.9.

obtained only through a limiting procedure, we compare two different values of m. In both cases the largest contributions come from the IR end of the spectrum. However, for the smaller mass the contributions beyond the deep IR have died out completely.

When considering the relative role of IR and UV contributions, one must take into account that the density of eigenvalues increases strongly with increasing $|\lambda|$. Thus in the lower plots of Figure 5.11 we show the accumulated contribution $A(|\lambda|) = \sum_{|\lambda'|\leq|\lambda|} C(\lambda')$. In particular we plot the normalized function $|A(|\lambda|)/\widetilde{\Sigma}_1|$ which approaches 1 in the UV limit. Here the difference between the large and the small mass is rather pronounced: For the large mass, where the dressed loop is closer to the thin Polyakov loop, the accumulated IR modes overshoot the value of 1 and the UV contributions are necessary to get the correct value. This is similar to the observations we have made in the previous section for the thin Polyakov loops. Towards the chiral limit, however, the approach to the final value of 1 becomes monotonic, and only the IR modes give sizeable contributions to the spectral sum for the dressed Polyakov loop. The scale up to which eigenvalues are relevant grows with T which is understandable since above the critical temperature the number of low lying eigenvalues decrease dramatically.

5.2.3 Summary

We have shown that a duality transformation of the quark condensate with respect to the fermionic temporal boundary condition gives rise to an order parameter for center symmetry. This order parameter can be viewed as a set of closed loops with the same winding number around compact time. For the case of single winding, which we refer to as the dressed Polyakov loop, our observable interpolates between the quark condensate (via a Fourier transform) and the thin Polyakov loop, in the limits of vanishing and infinite mass, respectively.

We studied the corresponding spectral sums of Dirac operator eigenvalues numerically for quenched gauge configurations. It was shown that the transition from the confined to the deconfined phase is seen as a different dependence of the spectral sums on the fermionic boundary condition. Decomposing the spectral sum shows that the main signal comes from the IR part of the spectrum.

At the moment the relations between chiral condensate and dressed Polyakov loops are mainly of mathematical nature. Their interpretation in terms of physics has just started. As a first step in this direction we would like to briefly mention an interesting connection between quark condensate and dressed Polyakov loop, which is obtained by using the Banks-Casher type of representation already addressed in the beginning of this chapter. After performing the consecutive limits of infinite volume and vanishing mass, the chiral condensate can be written as the density of eigenvalues at the origin also for arbitrary boundary angle φ. The dual condensate is then obtained by integrating the φ-dependent spectral density $\rho(0)_\varphi$, and for the case of $n = 1$ we find

$$\widetilde{\Sigma}_1 \;=\; \int_0^{2\pi} \frac{d\varphi}{2\pi}\, e^{-i\varphi} \rho(0)_\varphi \,. \tag{5.22}$$

Below T_c the spectral density at the origin is constant as a function of φ and a vanishing dressed Polyakov loop emerges. More interesting is the situation above T_c, where a non-trivial φ dependence is necessary for a non-vanishing dressed Polyakov loop. Naively one would think that above T_c the spectral density at the origin must be zero, such that the chiral condensate may vanish. However, in [129] (for a different phase convention) it was shown that the spectral gap depends on the relative phase between the boundary angle φ and the phase θ of the Polyakov loop. If φ equals the negative Polyakov loop phase the gap closes completely, giving rise to a non-zero spectral density. Inserting $\rho(0)_\varphi \propto \delta(\varphi + \theta)$ in (5.22) one obtains a non-vanishing dressed Polyakov loop above T_c with the correct phase θ.

As an outlook we stress that our theoretical considerations also hold for other gauge groups (where, e.g., for $SU(2)$ the phase transition can be of different order), for fermions with better chiral properties and for the case of dynamical quarks, the consequences of which would be interesting to study numerically.

Chapter 6

Conclusion

Summary

In this thesis, we addressed several non-perturbative topics in QCD which we have studied using the lattice formulation.

In Chapter 2, after a short recapitulation of continuum QCD, we turned to the discretization of fermions. In the next step the gauge fields were introduced by requiring local gauge invariance of lattice fermion actions. Both for fermions and gauge fields the discretization was not unique. This could be exploited to construct different actions, some of them being less sensitive to the lattice spacing. Then, we addressed certain issues connected to chiral symmetry on the lattice and pointed out how they can be solved. The resulting chiral Dirac operator, however, is numerically extremely expensive. A cheaper alternative, the Chirally Improved fermions, which are only approximately chiral, were used in many of our simulations. At the end of the chapter, we explained the techniques which are used in lattice QCD simulations.

Next, the ground and excited state masses of light mesons were investigated. We showed that the Euclidean two-point correlation functions, which we calculate within lattice QCD, can be interpreted in Hilbert space using the transfer matrix formalism. For the extraction of excited states we utilized the variational method (see Section 3.2). To construct a rich basis of interpolating operators for this method we used quark sources with different smearings, including ones with p-waves. This should give our operator a non-vanishing overlap with possible orbital excitations. The results of our calculation are of mixed quality. While the mass of first excited pseudoscalar state agrees very well with the experimental values, the excited state of the vector meson lies much too high. For the scalar and axialvector mesons, we obtained reliable results for the ground states only. Also here, the computed masses are above the experimental values. In previous quenched calculations, these discrepancies were remedied to a certain extent by

going to a finer lattice. On the other hand, when comparing to similar studies with dynamical Chirally Improved fermions, which give much better results, a natural explanation suggesting itself is that chiral sea quarks play a crucial role for the scalar meson.

In Chapter 4, we devised an new scheme to improve estimates of all-to-all propagators. The method relies on domain decomposition of the lattice in combination with the Schur complement. We derived the necessary formulas for half-to-half and closed propagators and discussed their practical implementation for Chirally Improved fermions. As a first test for the closed propagators, we considered the disconnected contribution of the pseudoscalar correlator. For this application we found only small improvement, mainly resulting in a smoothening of the correlation functions. Therefore, we decided to concentrate on the half-to-half propagators. For these a subset of possible applications was described. As the main testing ground of our domain decomposition improvement, we chose static-light hadron spectroscopy, which we investigated in detail using Chirally Improved fermions for the light quarks.

In the last chapter, we tried to connect two important non-perturbative phenomena in QCD: The spontaneous breaking of chiral symmetry and confinement. We started with deriving spectral sums for thin Polyakov loops, which were then investigated numerically. We found that these sums are dominated by the largest eigenvalues of the lattice Dirac operator. Also an unphysical dependence on the temporal extent of the lattice was established. Therefore, in a second step we defined a new order parameter for center symmetry. This order parameter, which we call the dressed Polyakov loop, is a quantity which extrapolates between the ordinary Polyakov loop in the limit $m \to \infty$ and a quantity, which we call the dual quark condensate, for vanishing quark mass. The latter was identified with the quark condensate Fourier transformed with respect to a $U(1)$-valued temporal boundary condition, which was used to distinguish between loops of different winding numbers. We found that the dressed Polyakov loop is dominated by the lowest lying eigenvalues of the lattice Dirac operator and showed that it is indeed an order parameter for center symmetry.

Outlook

For the computation of the excited meson spectrum, it would be interesting to perform calculations on an even finer lattice, in order to see whether the discrepancies between our results and the experimental number can be explained by effects coming from discretization errors. There exists such a lattice with the dimensions $24^3 \times 48$. Unfortunately, this currently exceeds our computational possibilities, at least in the case where we keep all the different operator combinations.

Our domain decomposition improvement scheme can be used for a large variety of projects. As next steps we consider the calculation of the mass splitting between R-hadron and glueballinos. Within lattice QCD, this is only possible in the static-light approximation since it ignores the spin of the heavy particle and thus does not take into account the supersymmetric nature of the gluino. This splitting has been studied before [130], using Maximal Variance Reduction. With the upcoming LHC, where it might be possible for the first time to observe SUSY particles, this is a very interesting application. On the other hand, also 3-point functions are on our agenda. In the light sector, we want to explore for example the wavefunctions of light hadrons. In the heavy quark sector, non-perturbative parameters can be calculated by considering four-quark operators. Also further parameters of HQET can be obtained by considering kinetic corrections as current insertions in our correlators. Both of them are used as input in perturbative calculations to find physics beyond the standard model.

The spectral sums for thin and dressed Polyakov loops, which we have derived and investigated, are also valid for configurations with dynamical fermions. In that case, however, the interpretation is complicated by the fact that the fermion determinant explicitly breaks the center symmetry. Thus, it is not possible anymore to interpret a finite expectation value of Polyakov loops as a signal of deconfinement. Nevertheless, the QCD phase transition is still reflected in the correlation function of local Polyakov loops, which can be obtained from our formulas by omitting the average over space.

Appendix A

Notations and conventions

Notations

In this thesis we always use natural units, i.e., we set $\hbar = c = 1$.
All our calculations are performed in Euclidean space-time, therefore the metric tensor is just $\delta_{\mu\nu}$ and we need not distinguish between covariant (lower) and contravariant (upper) indices, as it would be necessary in Minkowski space.

Conventions for γ-matrices

The Euclidean γ-matrices have the following properties:

$$\gamma_\mu^\dagger = \gamma_\mu, \qquad \mu = 1, \ldots, 5 \tag{A.1}$$

$$\{\gamma_\mu, \gamma_\nu\} = 2\delta_{\mu\nu}\mathbb{1}, \qquad \mu,\, \nu = 1, \ldots, 4 \tag{A.2}$$

Then, in the Euclidean version of the chiral representation they read:

$$\gamma_1 = \begin{pmatrix} 0 & 0 & 0 & \mathrm{i} \\ 0 & 0 & \mathrm{i} & 0 \\ 0 & -\mathrm{i} & 0 & 0 \\ -\mathrm{i} & 0 & 0 & 0 \end{pmatrix} \qquad \gamma_2 = \begin{pmatrix} 0 & 0 & 0 & 1 \\ 0 & 0 & -1 & 0 \\ 0 & -1 & 0 & 0 \\ 1 & 0 & 0 & 0 \end{pmatrix}$$

$$\gamma_3 = \begin{pmatrix} 0 & 0 & \mathrm{i} & 0 \\ 0 & 0 & 0 & -\mathrm{i} \\ -\mathrm{i} & 0 & 0 & 0 \\ 0 & \mathrm{i} & 0 & 0 \end{pmatrix} \qquad \gamma_4 = \begin{pmatrix} 0 & 0 & 1 & 0 \\ 0 & 0 & 0 & 1 \\ 1 & 0 & 0 & 0 \\ 0 & 1 & 0 & 0 \end{pmatrix} \tag{A.3}$$

In addition to that we define

$$\gamma_5 \quad = \quad \gamma_1\gamma_2\gamma_3\gamma_4 \quad = \quad \begin{pmatrix} 1 & 0 & 0 & 0 \\ 0 & 1 & 0 & 0 \\ 0 & 0 & -1 & 0 \\ 0 & 0 & 0 & -1 \end{pmatrix}. \tag{A.4}$$

Parity transformation for lattice fields

$$\psi(\vec{x},t) \xrightarrow{\mathcal{P}} \psi(\vec{x},t)^{\mathcal{P}} = \gamma_4\psi(-\vec{x},t), \tag{A.5}$$
$$\bar{\psi}(\vec{x},t) \xrightarrow{\mathcal{P}} \bar{\psi}(\vec{x},t)^{\mathcal{P}} = \bar{\psi}(-\vec{x},t)\gamma_4, \tag{A.6}$$
$$U_i(\vec{x},t) \xrightarrow{\mathcal{P}} U_i(\vec{x},t)^{\mathcal{P}} = U_i(-\vec{x}-\hat{i},t)^\dagger, \quad i=1,2,3, \tag{A.7}$$
$$U_4(\vec{x},t) \xrightarrow{\mathcal{P}} U_4(\vec{x},t)^{\mathcal{P}} = U_4(-\vec{x},t). \tag{A.8}$$

Properties of the charge-conjugation matrix C

$$C\gamma_\mu C^{-1} \quad = \quad -\gamma_\mu^T \tag{A.9}$$

For

$$\begin{aligned} \gamma_1^T &= -\gamma_1 \\ \gamma_2^T &= +\gamma_2 \\ \gamma_3^T &= -\gamma_3 \\ \gamma_4^T &= +\gamma_4 \\ \Rightarrow C &= i\gamma_2\gamma_4 \end{aligned} \tag{A.10}$$

$$C \quad = \quad C^{-1} \quad = \quad C^\dagger \quad = \quad -C^T \tag{A.11}$$

Transformation of lattice fields under charge-conjugation

$$\psi(x) \xrightarrow{\mathcal{C}} \psi(x)^{\mathcal{C}} = C^{-1}\bar{\psi}(x)^T, \tag{A.12}$$
$$\bar{\psi}(x) \xrightarrow{\mathcal{C}} \bar{\psi}(x)^{\mathcal{C}} = -\psi(x)^T C, \tag{A.13}$$
$$U_\mu(x) \xrightarrow{\mathcal{C}} U_\mu(x)^{\mathcal{C}} = U_\mu(x)^* = \left(U_\mu(x)^\dagger\right)^T. \tag{A.14}$$

Appendix B

Light mesons

In this appendix we list the numerical results for the light meson spectrum, which we have discussed in detail in Chapter 3. The Tables B.1 and B.2 contain our findings from correlated fits to the eigenvalues obtained from the generalized eigenvalue problem. We have fit these eigenvalues in the intervals denoted by $[t_{min}, t_{max}]$. The confidence of these fits is reflected by the $\chi^2/d.o.f.$ which should be close to one for a good and trustworthy fit. In the last column of the tables we list the optimal operator combination for each of the meson channels.

Table B.3 shows the numerical results of our chiral extrapolations for each of the channels for both lattices. Since the ensembles for the different sea quark masses should not be correlated, uncorrelated fits have been used for the chiral extrapolations. We first list the findings for the pseudoscalar meson, which we have used to obtain the κ_c^{-1} and then the fit parameters for the other meson channels. For the scalar meson on the $16^3 \times 32$ we have tried two different fit functions and listed both results. Also here the confidence of the fits is reflected by the $\chi^2/d.o.f.$ value.

$\kappa = \kappa_{sea} = \kappa_{val}$	am	$[t_{min}, t_{max}]$	$\chi^2/d.o.f.$	optimal operators
Pseudoscalar ground state				
0.1409	1.1520(23)	[5,10]	0.16	$P\gamma_5 P$,$n\gamma_5 n$,$\nabla_i\gamma_5\nabla_i$
0.1430	0.9774(28)	[2,10]	1.50	$P\gamma_5 P$,$n\gamma_5 n$,$\nabla_i\gamma_5\nabla_i$
0.1445	0.8201(29)	[2,9]	1.10	$P\gamma_5 P$,$n\gamma_5 n$,$\nabla_i\gamma_5\nabla_i$
0.1464	0.5363(60)	[2,9]	0.99	$P\gamma_5 P$,$n\gamma_5 n$,$\nabla_i\gamma_5\nabla_i$
Vector ground state				
0.1409	1.4469(55)	[4,10]	0.88	$P\gamma_i P$,$L\gamma_i L$
0.1430	1.3070(62)	[3,10]	0.37	$n\gamma_i n$,$\nabla_i n$
0.1445	1.1870(57)	[2,9]	0.35	$P\gamma_i P$,$P\gamma_i\gamma_4 P$,$n\gamma_i n$,$L\gamma_i L$
0.1464	0.973(15)	[3,9]	0.41	$P\gamma_i P$,$n\gamma_i n$
Scalar ground state				
0.1409	2.188(28)	[2,7]	0.17	$\nabla_i\mathbb{1}\nabla_i$
0.1430	1.964(30)	[2,5]	0.44	$\nabla_i\mathbb{1}\nabla_i$
0.1445	1.824(29)	[2,6]	0.84	$\nabla_i\mathbb{1}\nabla_i$
0.1464	1.620(55)	[2,5]	0.24	$\nabla_i\mathbb{1}\nabla_i$
Axialvector ground state				
0.1409	2.291(51)	[3,6]	0.12	$\nabla_i\gamma_k\gamma_5\nabla_i$
0.1430	2.022(23)	[2,6]	0.14	$\nabla_i\gamma_k\gamma_5\nabla_i$
0.1445	1.922(21)	[2,6]	0.94	$\nabla_i\gamma_k\gamma_5\nabla_i$
0.1464	1.651(66)	[3,6]	0.39	$\nabla_i\gamma_k\gamma_5\nabla_i$
Pseudoscalar 1st excited state				
0.1409	2.276(40)	[2,5]	0.24	$P\gamma_5 P$,$n\gamma_5 n$,$\nabla_i\gamma_5\nabla_i$
0.1430	2.003(90)	[2,5]	0.16	$P\gamma_5 P$,$n\gamma_5 n$,$\nabla_i\gamma_5\nabla_i$
0.1445	1.868(62)	[2,4]	0.01	$P\gamma_5 P$,$n\gamma_5 n$,$\nabla_i\gamma_5\nabla_i$
0.1464	1.56(14)	[2,4]	0.71	$P\gamma_5 P$,$n\gamma_5 n$,$\nabla_i\gamma_5\nabla_i$
Vector 1st excited state				
0.1409	2.436(50)	[3,5]	0.01	$P\gamma_i P$,$L\gamma_i L$
0.1430	2.35(13)	[2,4]	0.20	$n\gamma_i n$,$\nabla_i n$
0.1445	2.082(48)	[2,5]	0.53	$P\gamma_i P$,$P\gamma_i\gamma_4 P$,$n\gamma_i n$,$L\gamma_i L$
0.1464	2.128(42)	[2,4]	0.10	$P\gamma_i P$,$n\gamma_i n$

Table B.1: Results of the meson masses from $12^3 \times 24$ lattice. The interval $[t_{min}, t_{max}]$ denotes the time-range where we have fitted the eigenvalues. $\chi^2/d.o.f.$ represents the quality of our fits. In the last column we show our final choice for the optimal operator combination for each meson channel.

$\kappa = \kappa_{sea} = \kappa_{val}$	am	$[t_{min}, t_{max}]$	$\chi^2/d.o.f.$	optimal operators
Pseudoscalar ground state				
0.1375	0.8917(24)	[4,13]	0.58	$P\gamma_5 P$,$n\gamma_5 n$,$\nabla_i\gamma_5\nabla_i$
0.1390	0.7252(23)	[3,13]	0.99	$P\gamma_5 P$,$n\gamma_5 n$,$\nabla_i\gamma_5\nabla_i$
0.1400	0.5958(22)	[5,11]	0.88	$P\gamma_5 P$,$n\gamma_5 n$,$\nabla_i\gamma_5\nabla_i$
0.1410	0.4290(29)	[5,9]	0.81	$P\gamma_5 P$,$n\gamma_5 n$
Vector ground state				
0.1375	1.1066(35)	[4,13]	1.02	$P\gamma_i P$,$n\gamma_i n$
0.1390	0.9648(48)	[4,12]	0.80	$P\gamma_i P$,$n\gamma_i n$
0.1400	0.8611(64)	[5,12]	0.84	$P\gamma_i P$,$n\gamma_i n$
0.1410	0.7332(82)	[5,13]	0.40	$P\gamma_i P$,$n\gamma_i n$
Scalar ground state				
0.1375	1.583(41)	[3,7]	0.43	$L\mathbb{1}n$
0.1390	1.379(24)	[2,8]	0.36	$L\mathbb{1}n$
0.1400	1.263(34)	[4,8]	0.17	$\nabla_i\mathbb{1}\nabla_i$
0.1410	0.948(75)	[4,7]	1.12	$L\mathbb{1}n$
Axialvector ground state				
0.1375	1.621(19)	[2,7]	0.99	$P\gamma_i\gamma_5 P$,$n\gamma_i\gamma_5 L$
0.1390	1.334(74)	[5,8]	0.12	$P\gamma_i\gamma_5 P$,$n\gamma_i\gamma_5 L$
0.1400	1.307(48)	[4,8]	0.24	$P\gamma_i\gamma_5 P$,$n\gamma_i\gamma_5 L$
0.1410	1.199(28)	[3,7]	0.39	$P\gamma_i\gamma_5 P$,$n\gamma_i\gamma_5 L$
Pseudoscalar 1st excited state				
0.1375	1.838(30)	[2,6]	0.34	$P\gamma_5 P$,$n\gamma_5 n$,$\nabla_i\gamma_5\nabla_i$
0.1390	1.605(62)	[3,6]	0.37	$P\gamma_5 P$,$n\gamma_5 n$,$\nabla_i\gamma_5\nabla_i$
0.1400	1.46(12)	[4,6]	0.01	$P\gamma_5 P$,$n\gamma_5 n$,$\nabla_i\gamma_5\nabla_i$
0.1410	1.660(74)	[3,6]	0.03	$P\gamma_5 P$,$n\gamma_5 n$
Vector 1st excited state				
0.1375	2.060(26)	[3,5]	0.08	$P\gamma_i P$,$n\gamma_i n$
0.1390	1.879(55)	[4,7]	0.13	$P\gamma_i P$,$n\gamma_i n$
0.1400	1.724(59)	[4,7]	0.23	$P\gamma_i P$,$n\gamma_i n$
0.1410	1.827(90)	[4,6]	0.47	$P\gamma_i P$,$n\gamma_i n$

Table B.2: The same as in B.1 but for the $16^3 \times 32$ lattice.

$L^3 \times T$	κ_c^{-1}	B	C	$\chi^2/d.o.f.$
$12^3 \times 24$	6.7678(28)	9.44(25)	-8.4(1.4)	0.10
$16^3 \times 32$	7.0366(22)	6.61(24)	1.0(1.6)	0.36

$L^3 \times T$	A	B	C	$\chi^2/d.o.f.$
Vector ground state				
$12^3 \times 24$	0.801(29)	0.656(66)	-0.128(35)	0.78
$16^3 \times 32$	0.586(18)	0.857(74)	-0.255(67)	0.37
Scalar ground state				
$12^3 \times 24$	1.452(48)	0.549(49)	—	0.14
$16^3 \times 32$	0.927(57)	0.85(11)	—	2.28
$16^3 \times 32$	0.73(14)	1.65(55)	-0.75(51)	2.41
Axialvector ground state				
$12^3 \times 24$	1.546(54)	0.528(63)	—	1.91
$16^3 \times 32$	1.064(24)	0.696(53)	—	0.88
Pseudoscalar 1st excited state				
$12^3 \times 24$	1.41(10)	0.652(32)	—	0.14
$16^3 \times 32$	1.15(15)	0.86(20)	—	0.001
Vector 1st excited state				
$12^3 \times 24$	1.988(52)	0.309(63)	—	3.94
$16^3 \times 32$	1.473(94)	0.74(13)	—	0.13

Table B.3: Numerical results of the chiral extrapolations of the different meson channels in Section 3.5.

Appendix C

Anticommuting numbers

Anticommuting numbers are important since they are needed to describe fermion fields. This is due to the fact that fermions have to be completely antisymmetric, and this is a property which cannot be fulfilled with ordinary numbers. This appendix only provides the most important formulas for computing with anticommuting numbers. For a more detailed discussion, see Chapter 1 of [131].

Definition

We define anticommuting numbers, also known as *Grassmann numbers*, in the following way:
The generators $\theta_i, i = 1, \ldots, N$, are defined to obey the anticommutation relation

$$\theta_i \theta_j = -\theta_j \theta_i \qquad \forall\, i, j. \tag{C.1}$$

Directly from that, one obtains, that the θ_i are *nilpotent*,

$$\theta_i^2 = 0. \tag{C.2}$$

This means that the power series expansion of an arbitrary function of the generators terminates after a finite number of terms. So all functions are polynomials of the form

$$A = a + \sum_i a_i \theta_i + \frac{1}{2!} \sum_{i,j} a_{ij} \theta_i \theta_j + \ldots + \frac{1}{N!} \sum_{i_1,\ldots,i_N} a_{i_1 \ldots i_N} \theta_{i_1} \cdots \theta_{i_N} \tag{C.3}$$

with $a_{i_1 \ldots i_N} \in \mathbb{C}$, totally antisymmetric. These polynomials form an algebra, the so-called *Grassmann algebra*.

Differentiation in Grassmann algebras

The differentiation in Grassmann algebras with respect to the generators has following properties:

$$\frac{\partial}{\partial\theta_i}1 = 0, \tag{C.4}$$

$$\frac{\partial}{\partial\theta_i}\theta_j = \delta_{ij}, \tag{C.5}$$

$$\frac{\partial}{\partial\theta_i}\theta_j A = -\theta_j\frac{\partial}{\partial\theta_i}A \qquad i \neq j, \tag{C.6}$$

$$\frac{\partial}{\partial\theta_i}\frac{\partial}{\partial\theta_j}A = -\frac{\partial}{\partial\theta_j}\frac{\partial}{\partial\theta_i}A \qquad \Longrightarrow \frac{\partial^2}{\partial\theta_i^2}A = 0. \tag{C.7}$$

Integration in Grassmann algebras

We define the integration to be an operation identical to differentiation

$$\int d\theta_i A = \frac{\partial}{\partial\theta_i}A, \qquad \forall A. \tag{C.8}$$

From that definition we obtain the following properties, similar to the properties of the derivative:

$$\int d\theta_i 1 = 0, \tag{C.9}$$

$$\int d\theta_i\theta_j = \delta_{ij}, \tag{C.10}$$

$$\int d\theta_i\theta_j A = -\theta_j\int d\theta_i A \qquad i \neq j, \tag{C.11}$$

$$\int d\theta_i d\theta_j A = -\int d\theta_j d\theta_i A. \tag{C.12}$$

Because of our definition, we get the following property for a combination of integration and differentiation:

$$\int d\theta_i\frac{\partial}{\partial\theta_i}A = 0 \tag{C.13}$$

For the N-dimensional integral, in which we are particularly interested, we then obtain the following properties

1. The integral is of course a linear functional

$$\int d^N\theta(\lambda_1 A_1 + \lambda_2 A_2) = \lambda_1\int d^N\theta A_1 + \lambda_2\int d^N\theta A_2, \tag{C.14}$$

where $d^N\theta = d\theta_N d\theta_{N-1}\ldots d\theta_1$.

2. It is normalized

$$\int d^N\theta\theta_1\theta_2\dots\theta_N \;=\; 1. \tag{C.15}$$

3. Only expressions proportional to $\theta_1\theta_2\dots\theta_N$ contribute

$$\int d^N\theta A \;=\; a_{1\,2\,\dots\,N}. \tag{C.16}$$

Change of variables in Grassmann integrals

For a linear transformation of the variables, $\theta_i' = M_{ij}\theta_j$ one obtains

$$d^N\theta' \;=\; \det(M)d^N\theta. \tag{C.17}$$

Gaussian integrals with Grassmann variables

Let M_{ij} be a complex $N \times N$ matrix and $\theta_1,\dots,\theta_N,\bar\theta_1,\dots,\bar\theta_N$ the generators of a 2N-dimensional Grassmann algebra. For the simple Gaussian integral we then obtain

$$\begin{aligned}\int\prod_{k=1}^{N}(d\theta_k d\bar\theta_k)e^{\sum_{i,j}\bar\theta_i M_{ij}\theta_j} &= \det(M)\int\prod_{k=1}^{N}(d\theta_k' d\bar\theta_k)e^{\sum_i\bar\theta_i\theta_i'},\\ &= \det(M)\prod_{k=1}^{N}\int(d\theta_k' d\bar\theta_k)(1+\bar\theta_k\theta_k'),\\ &= \det(M).\end{aligned} \tag{C.18}$$

In the first step, we performed a transformation of variables $\theta_i' = M_{ij}\theta_j$, in the second step we used the property of the exponential function to split the exponential of a sum to a product of exponentials and then we expanded these exponentials. In the last step we used (C.9) and (C.15). Therefore, all these integrals are 1.

The generating functional

$$Z[\eta,\bar\eta] \;=\; \int\prod_{i=1}^{N}(d\theta_i d\bar\theta_i)\exp\left\{\sum_{i,j}\bar\theta_i M_{ij}\theta_j + \sum_i[\bar\theta_i\eta_i + \bar\eta_i\theta_i]\right\}, \tag{C.19}$$

can be evaluated in the same way. We have to rewrite the exponent in the following way (for simplification we use vector notation)

$$\bar\theta^T M\theta + \bar\theta^T\eta + \bar\eta^T\theta \;=\; (\bar\theta^T + \bar\eta^T M^{-1})M(\theta + M^{-1}\eta) - \bar\eta^T M^{-1}\eta \tag{C.20}$$

and then we perform an affine transformation

$$\theta_i' = \theta_i + M_{ij}^{-1}\eta_j, \tag{C.21}$$
$$\bar{\theta}_i' = \bar{\theta}_i + \bar{\eta}_j M_{ji}^{-1}. \tag{C.22}$$

Then we obtain for the integral

$$\begin{aligned} Z[\eta,\bar{\eta}] &= e^{-\sum_{i,j}\bar{\eta}_i M_{ij}^{-1}\eta_j}\int\prod_i (d\theta_i' d\bar{\theta}_i') e^{\sum_{i,j}\bar{\theta}_i M_{ij}\theta_j} \\ &= \det(M) e^{-\sum_{i,j}\bar{\eta}_i M_{ij}^{-1}\eta_j}. \end{aligned} \tag{C.23}$$

For $\bar{\eta} = \eta = 0$, we recover the previous result

$$Z[0,0] = \det(M). \tag{C.24}$$

This result can be used to calculate so-called n-point functions.

$$\begin{aligned} &\int\prod_{k=1}^N (d\bar{\theta}_k d\theta_k)\theta_{i_1}\bar{\theta}_{j_1}\theta_{i_2}\bar{\theta}_{j_2}\ldots\theta_{i_N}\bar{\theta}_{j_N}\exp\left\{\sum_{i,j}\bar{\theta}_i M_{ij}\theta_j\right\} \\ &\quad = \prod_{k=1}^N \left(\frac{\partial}{\partial\bar{\eta}_{i_k}}, \frac{\partial}{\partial\eta_{j_k}}\right) Z[\eta,\bar{\eta}]\Big|_{\substack{\eta=0\\ \bar{\eta}=0}}, \\ &\quad = (-1)^n \det(M)\sum_{\mathcal{P}}\sigma(\mathcal{P})(M^{-1})_{i_{\mathcal{P}1}j_1}(M^{-1})_{i_{\mathcal{P}2}j_2}\ldots(M^{-1})_{i_{\mathcal{P}N}j_N}, \end{aligned} \tag{C.25}$$

where we sum over all permutations $\mathcal{P} \in \{1,2,\ldots,N\}$. $\sigma(\mathcal{P})$ gives the sign for the particular permutation $\mathcal{P}$.

Appendix D

Path integral derivation for all-to-all propagators

In Section 4.1, we derive exact relations (4.9) and (4.14) for the blocks of the quark propagator. In those derivations we relied upon the property of random vectors $\chi_i^{(n)},\ n = 1, \ldots, N$:

$$\lim_{N\to\infty} \left(\frac{1}{N} \sum_{n=1}^{N} \chi_i^{(n)} \chi_j^{(n)\dagger} \right) \quad = \quad \delta_{ij}. \tag{D.1}$$

But there exist also other possibilities to derive the same results. The Dirac operator D can be viewed as a huge two-dimensional matrix[1]. Then the relations (4.9) and (4.12) just represent a quantity known from linear algebra called Schur complement.

As a second alternative, we explicitly show here the derivation using the path integral over the fermionic degrees of freedom. The Dirac propagator can be represented by a path integral in the following way

$$D_{ij}^{-1} \quad = \quad \frac{1}{Z} \int [\prod_k d\psi_k][\prod_l d\bar{\psi}_l] \psi_i \bar{\psi}_j e^{-S_{ferm}}, \tag{D.2}$$

where

$$Z \quad = \quad \int [\prod_k d\psi_k][\prod_l d\bar{\psi}_l] e^{-S_{ferm}}, \tag{D.3}$$

is the partition function and S_{ferm} the fermion action

$$S_{ferm} \quad = \quad \bar{\psi}_i D_{ij} \psi_j. \tag{D.4}$$

[1] One can combine the different indices (x, α, a) to a multiindex.

The first step in our alternative approach is to split the fermion action in a sum of four separate contributions:

$$S_{ferm} = \bar{\psi}_s D_{ss'} \psi_{s'} + \bar{\psi}_r D_{rr'} \psi_{r'} + \bar{\psi}_s D_{sr} \psi_r + \bar{\psi}_r D_{rs} \psi_s. \tag{D.5}$$

The leading two contributions are only connecting the fermion fields within the regions R and S, respectively, while the two other contributions connect between the regions.
In a similar way, one can also divide the integral measures in D.2 and D.3.

When one now considers for example the special case of D.2 when $i = r \in R$ and $j = s \in S$ and uses D.5 one obtains for the propagator

$$D^{-1}_{rs} = \frac{1}{Z} \int [\prod_k d\psi_k][\prod_l d\bar{\psi}_l] \psi_r \bar{\psi}_s \, e^{-S_{ferm}}, \tag{D.6}$$

$$= -\frac{1}{Z} \int [\prod_s d\psi_s][\prod_s d\bar{\psi}_s] \bar{\psi}_s \, e^{\bar{\psi}_s \bar{D}_{ss'} \psi_{s'}} \times \tag{D.7}$$

$$\int [\prod_r d\psi_r][\prod_r d\bar{\psi}_r] \psi_r \, e^{\bar{\psi}_r \bar{D}_{rr'} \psi_{r'} + \bar{\psi}_r \bar{D}_{rs} \psi_s + \bar{\psi}_s \bar{D}_{sr} \psi_r},$$

$$= -\frac{\det(M_{rr'})}{Z} \int [\prod_s d\psi_s][\prod_s d\bar{\psi}_s] \bar{\psi}_s (-\bar{D}^{-1}_{rr'} \tilde{D}_{r's'} \psi_{s'}) \, e^{\bar{\psi}_s M_{ss'} \psi_{s'}}, \tag{D.8}$$

$$= -\frac{\det(M_{rr'}) \det(M_{ss'})}{Z} \bar{D}^{-1}_{rr'} \tilde{D}_{r's'} M^{-1}_{s's}, \tag{D.9}$$

where $M_{rr'}$ and $M_{ss'} := \bar{D}_{ss'} - \tilde{D}_{sr} \bar{D}^{-1}_{rr'} \tilde{D}_{r's'}$ are the diagonal blocks of a decomposed version of D with 0's as off-diagonal blocks. Therefore, $Z = \det(D) = \det(M_{rr'}) \det(M_{ss'})$ and the ratio becomes 1. For the next to last step, we completed the square in the exponent and performed a shift of the integral measure.

Since $M_{ss'}$ is the Schur complement of $D_{rr'}$, one can show that in fact This leads us to our final result

$$D^{-1}_{rs} = -\bar{D}^{-1}_{rr'} \tilde{D}_{r's'} D^{-1}_{s's}, \tag{D.10}$$

where we used the fact that the product of the two determinants are equal to the determinant of the full Dirac operator. In a similar way one can obtain the formula for quark propagator connecting sites within one region.

Appendix E

Fitting techniques

From N measurements of L quantities we obtain N data sets of the form

$$(x_i; y_i^s), \qquad i = 1, \ldots, L, \quad s = 1, \ldots, N. \tag{E.1}$$

In the case of our calculations, for example, we have data sets $(t, C(t)_s)$, where $C(t)$ is the correlator matrix at time t. From that one can build the *sample averages* of the quantities y_i^s

$$\overline{y}_i = \frac{1}{N}\sum_{s=1}^{N} y_i^s, \tag{E.2}$$

and the *variance*

$$s_i^2 = \frac{1}{N-1}\sum_{s=1}^{N}(y_i^s - \overline{y}_i)^2 \tag{E.3}$$

$$= \frac{N}{N-1}(\overline{y^2} - \overline{y}^2), \tag{E.4}$$

where s_i are the standard deviations. The statistical error is $\sigma_i = \frac{s_i}{\sqrt{N}}$. So, in the end, we obtain

$$(x_i, \overline{y}_i \pm \sigma_i) \tag{E.5}$$

for our L quantities.

Least squares fitting

The question arises which function $f(x_i; \mathbf{a})$ with parameters $\mathbf{a} = (a_1, a_2, \ldots, a_n)$ describes our data sets $(x_i, \overline{y}_i \pm \sigma_i)$ best. For our calculations for example, we have to fit a function $f(t; A, m) = Ae^{-mt}$ with parameters A, m to the data sets $t, C(t)$. To answer this question one uses a least squares fit. We have to distinguish the two cases:

1. The data for different x_i are independent of each other.

2. The data are correlated.

What we want to find are the optimal values for the parameters a_i.

For the first case, we introduce the χ^2-functional

$$\chi^2(\mathbf{a}) = \sum_{i=1}^{L} \frac{(\overline{y}_i - f(x_i, \mathbf{a}))^2}{\sigma_i^2}. \tag{E.6}$$

When we minimize this functional with respect to the a_i we obtain the optimal values $\bar{a}_i$ for all n parameters.

In the second case, where our data are correlated, we have to introduce the covariance matrix

$$V_{ij} = \frac{1}{N-1}(\overline{y_i y_j} - \overline{y}_i \overline{y}_j) \tag{E.7}$$

$$= \frac{1}{N(N-1)} \sum_{s=1}^{N} (y_i^s - \overline{y}_i)(y_j^s - \overline{y}_j), \tag{E.8}$$

where y_i^s is sample number s of the i-th data point (see also [2]). This matrix characterizes the correlations between the measured quantities.
For the correlated case, the χ^2-functional is defined as

$$\chi^2(\mathbf{a}) = \sum_{i,j=1}^{L} [\overline{y}_i - f(x_i, \mathbf{a})] V_{ij}^{-1} [\overline{y}_j - f(x_j, \mathbf{a})]. \tag{E.9}$$

If the data are not correlated the $V_{ij} = \delta_{ij} \frac{s_i^2}{N}$ and the χ^2 functional (E.9) reduces to (E.6). This should be minimal with respect to the a_i for the optimal values $\bar{a}_i$:

$$\left.\frac{\partial \chi^2}{\partial a_k}\right|_{\mathbf{a}=\bar{\mathbf{a}}} = 2 \sum_{i,j=1}^{L} \frac{\partial f(x_i, \bar{\mathbf{a}})}{\partial a_k} V_{ij}^{-1} [f(x_j, \bar{\mathbf{a}}) - \overline{y}_j], \tag{E.10}$$

$$\stackrel{!}{=} 0, \tag{E.11}$$

where we used that V is a symmetric matrix. This leads to n equations for the $\bar{a}_i$ which then have to be solved[1]. To estimate the quality of our fit we consider the number of degrees of freedom (d.o.f.) ν of our fit:

$$\nu = L - n \tag{E.12}$$

[1]This is usually done numerically.

For the expectation value of χ^2 one obtains[2]

$$\overline{\chi^2} \quad = \quad \nu, \tag{E.13}$$

and therefore, we consider a fit to be reasonable if

$$\chi^2/d.o.f. \quad = \quad \frac{\chi^2}{\nu} \quad \approx \quad 1. \tag{E.14}$$

The optimal parameters $\bar{a}_i$, we obtain from this procedure, are so-called *secondary quantities*, because they are determined by functions of primary averages, i.e., averages of observables which have been measured directly. In our case the primary averages are the $\overline{y}_i$.

If the measurement sample and the eventual subsamples defining the secondary quantities become infinitely large, or if we use an infinite amount of measurement samples (and if we have chosen the right function $f(x_i, \mathbf{a})$), then the ensemble average of the $\mathbf{a}$ gives the ensemble average of y_i by

$$\overline{\overline{y}}_i \quad = \quad f(x_i, \overline{\overline{\mathbf{a}}}). \tag{E.15}$$

We are also interested in the errors of the parameters $\mathbf{a}$. Unfortunately, in most cases one does not have a large number of samples. Then one has to calculate the error of secondary quantities using methods like *Jackknife* (see Appendix F) or *Bootstrap*.

[2]We assume, that the y_i^s are Gaussian distributed around $\overline{y}_i$ with a variance of σ_i^2

$$P(y_i) \quad = \quad \frac{1}{\sqrt{2\pi}\sigma_i} e^{-\frac{(y_i-\overline{y}_i)^2}{2\sigma_i^2}}.$$

Appendix F

Jackknife method

If one has samples which are not very large, one can estimate the error of secondary variables, such as fit parameters, by using the *Jackknife method*. When one has a not too large number of data points $y^s,\ s = 1, \ldots, N$, one can calculate the sample average

$$\overline{y} \;=\; \frac{1}{N}\sum_{s=1}^{N} y_s. \tag{F.1}$$

From that one obtains the best estimator for a secondary quantity $\mathbf{a}$ by

$$\overline{\mathbf{a}} \;=\; \mathbf{a}(\overline{y}). \tag{F.2}$$

To estimate the error of this quantity $\overline{\mathbf{a}}$ using the Jackknife method one does the following:

First one calculates N so-called *Jackknife subsamples*

$$y_{(J)s} \;=\; \frac{1}{N-1}\sum_{\substack{i=1\\ i\neq s}}^{N} y_i. \tag{F.3}$$

From these one determines the *jackknife estimators* of the secondary quantities

$$\mathbf{a}_{(J)s} \;=\; \mathbf{a}(y_{(J)s}). \tag{F.4}$$

They have the average

$$\overline{\mathbf{a}_{(J)}} \;=\; \frac{1}{N}\sum_{s=1}^{N} \mathbf{a}_{(J)s} \tag{F.5}$$

The variance of the jackknife estimators is

$$\sigma^2_{(J)} \;=\; \frac{N-1}{N}\sum_{s=1}^{N}\left(\mathbf{a}_{(J)s} - \overline{\mathbf{a}_{(J)}}\right)^2 . \tag{F.6}$$

And finally one obtains for the ensemble average

$$\overline{\overline{\mathbf{a}}} \;=\; \overline{\mathbf{a}} \pm \sigma_{(J)}. \tag{F.7}$$

Appendix G

Coefficients for CI-fermions

In this appendix we list the coefficients for the various paths, which are necessary to construct the Chirally Improved Dirac operator. We show the coefficients for the free case and for different gauge ensembles used in our simulations.

coefficient	value
s_1	$+0.1409870061 \cdot 10^{+1}$
s_2	$-0.4063348276 \cdot 10^{-1}$
s_3	$-0.1328179378 \cdot 10^{-1}$
s_5	$-0.1707793316 \cdot 10^{-2}$
s_6	$+0.1707277975 \cdot 10^{-2}$
s_8	$-0.2995931667 \cdot 10^{-2}$
s_{10}	$-0.4097715677 \cdot 10^{-3}$
s_{11}	$-0.7711930549 \cdot 10^{-3}$
s_{13}	$+0.6542013926 \cdot 10^{-2}$
v_1	$+0.2526693368 \cdot 10^{+0}$
v_2	$+0.4483311559 \cdot 10^{-2}$
v_4	$+0.3493344361 \cdot 10^{-2}$
v_5	$+0.1077099799 \cdot 10^{-2}$

Table G.1: Numerical values for the coefficients of the Chirally Improved Dirac operator for the case of free fermions. In the non-interacting case the axialvector, tensor, and pseudoscalar coefficients vanish identically.

	$\beta = 7.57, N_f = 0$	$\beta = 7.90, N_f = 0$	$\beta = 8.15, N_f = 0$	$\beta = 4.65\,\&\,5.20, N_f = 2$
s_1	$+0.1449633287 \cdot 10^{+1}$	$+0.1437291946 \cdot 10^{+1}$	$+0.1429617950 \cdot 10^{+1}$	$+0.1481599252 \cdot 10^{+1}$
s_2	$-0.4649489101 \cdot 10^{-1}$	$-0.4455101096 \cdot 10^{-1}$	$-0.4340196840 \cdot 10^{-1}$	$-0.5218251439 \cdot 10^{-1}$
s_3	$-0.1419472993 \cdot 10^{-1}$	$-0.1393395364 \cdot 10^{-1}$	$-0.1376070195 \cdot 10^{-1}$	$-0.1473643847 \cdot 10^{-1}$
s_5	$-0.1951438365 \cdot 10^{-2}$	$-0.1870862476 \cdot 10^{-2}$	$-0.1823130090 \cdot 10^{-2}$	$-0.2186103421 \cdot 10^{-2}$
s_6	$+0.1929002274 \cdot 10^{-2}$	$+0.1856411730 \cdot 10^{-2}$	$+0.1813031470 \cdot 10^{-2}$	$+0.2133989696 \cdot 10^{-2}$
s_8	$-0.3490247215 \cdot 10^{-2}$	$-0.3323708468 \cdot 10^{-2}$	$-0.3226554504 \cdot 10^{-2}$	$-0.3997001821 \cdot 10^{-2}$
s_{10}	$-0.4549399493 \cdot 10^{-3}$	$-0.4404207698 \cdot 10^{-3}$	$-0.4316329921 \cdot 10^{-3}$	$-0.4951673735 \cdot 10^{-3}$
s_{11}	$-0.8801452373 \cdot 10^{-3}$	$-0.8443085525 \cdot 10^{-3}$	$-0.8229969177 \cdot 10^{-3}$	$-0.9836500799 \cdot 10^{-3}$
s_{13}	$+0.7112369095 \cdot 10^{-2}$	$+0.6939488217 \cdot 10^{-2}$	$+0.6829848555 \cdot 10^{-2}$	$+0.7529838581 \cdot 10^{-2}$
v_1	$+0.2252551313 \cdot 10^{+0}$	$+0.2344881450 \cdot 10^{+0}$	$+0.2398768495 \cdot 10^{+0}$	$+0.1972229309 \cdot 10^{+0}$
v_2	$+0.6173688885 \cdot 10^{-2}$	$+0.5570579593 \cdot 10^{-2}$	$+0.5235045741 \cdot 10^{-2}$	$+0.8252157565 \cdot 10^{-2}$
v_4	$+0.4346164444 \cdot 10^{-2}$	$+0.4069210212 \cdot 10^{-2}$	$+0.3902570093 \cdot 10^{-2}$	$+0.5113056314 \cdot 10^{-2}$
v_5	$+0.1406757995 \cdot 10^{-2}$	$+0.1295130178 \cdot 10^{-2}$	$+0.1230111843 \cdot 10^{-2}$	$+0.1736609425 \cdot 10^{-2}$
t_1	$-0.8197887537 \cdot 10^{-1}$	$-0.7969367736 \cdot 10^{-1}$	$-0.7827609400 \cdot 10^{-1}$	$-0.8792744664 \cdot 10^{-1}$
t_2	$-0.2249893049 \cdot 10^{-2}$	$-0.2148500209 \cdot 10^{-2}$	$-0.2089077853 \cdot 10^{-2}$	$-0.2553055577 \cdot 10^{-2}$
t_3	$+0.1910104032 \cdot 10^{-2}$	$+0.1843129015 \cdot 10^{-2}$	$+0.1802631320 \cdot 10^{-2}$	$+0.2093792069 \cdot 10^{-2}$
t_5	$-0.4923429496 \cdot 10^{-2}$	$-0.4706372948 \cdot 10^{-2}$	$-0.4578817715 \cdot 10^{-2}$	$-0.5567377075 \cdot 10^{-2}$
t_{15}	$-0.3205140224 \cdot 10^{-2}$	$-0.3118109153 \cdot 10^{-2}$	$-0.3063890989 \cdot 10^{-2}$	$-0.3427310798 \cdot 10^{-2}$
p_1	$-0.7618499047 \cdot 10^{-2}$	$-0.7402427261 \cdot 10^{-2}$	$-0.7268745124 \cdot 10^{-2}$	$-0.8184103136 \cdot 10^{-2}$

Table G.2: Numerical values for the coefficients of the Chirally Improved Dirac operator for different gauge ensembles of the Lüscher-Weisz gauge action. In the quenched case, $N_f = 0$, the gauge fields are modified by HYP blocking [104]. For the case of dynamical fermions, $N_f = 2$, stout smearing [105] is applied and the same coefficients are used for both beta values. Although this is not optimal it allows for a better comparison. Not listed coefficients are zero.

Appendix H

Lattices

In this appendix we summarize the details of the ensembles used in our various lattice QCD simulations.

Meson spectroscopy

β	$L^3 \times T$	a [fm]	c_{sw}	κ			
				m_{PS}/m_V			
				N_{traj}(thermalized)			
				0.1409	0.1430	0.1445	0.1464
1.80	$12^3 \times 24$	0.2150(22)	1.60	0.807(1)	0.753(1)	0.694(2)	0.547(4)
				6250	5000	7000	5250
				0.1375	0.1390	0.1400	0.1410
1.95	$16^3 \times 32$	0.1555(17)	1.53	0.804(1)	0.752(1)	0.690(2)	0.582(3)
				7000	7000	7000	5000

Table H.1: Parameters of the configurations with $N_f = 2$ dynamical Clover-Wilson fermions as quoted in [83]. For the gauge action the Iwasaki action has been used. In our simulations we use only every 50th thermalized trajectory in order to obtain decorrelated results and at the same time save computational resources.

Domain decomposition improvement

β	$L^3 \times T$	a [fm]	$M_{\pi,sea}$	link smear	N_{conf}	$\left(\begin{smallmatrix} l_1 & l_2 \\ l_3 & l_4 \end{smallmatrix}, \begin{smallmatrix} N_{sm,1} & N_{sm,2} \\ N_{sm,3} & N_{sm,4} \end{smallmatrix}, \kappa\right)$
7.57	$12^3 \times 24$	0.20	∞	HYP	200	$\left(\begin{smallmatrix} 0 & 0 \\ 1 & 2 \end{smallmatrix}, \begin{smallmatrix} 0 & 8 \\ 12 & 16 \end{smallmatrix}, 0.20\right)$
7.90	$16^3 \times 32$	0.15	∞	HYP	100	$\left(\begin{smallmatrix} 0 & 0 \\ 1 & 2 \end{smallmatrix}, \begin{smallmatrix} 0 & 12 \\ 18 & 24 \end{smallmatrix}, 0.20\right)$
8.15	$20^3 \times 40$	0.12	∞	HYP	100	$\left(\begin{smallmatrix} 0 & 0 \\ 1 & 2 \end{smallmatrix}, \begin{smallmatrix} 0 & 16 \\ 24 & 32 \end{smallmatrix}, 0.20\right)$
5.20	$12^3 \times 24$	0.115	500 MeV	Stout	74	$\left(\begin{smallmatrix} 0 & 0 \\ 1 & 2 \end{smallmatrix}, \begin{smallmatrix} 0 & 8 \\ 12 & 16 \end{smallmatrix}, 0.20\right)$
4.65	$16^3 \times 32$	0.16	450 MeV	Stout	100	$\left(\begin{smallmatrix} 0 & 0 \\ 1 & 2 \end{smallmatrix}, \begin{smallmatrix} 0 & 12 \\ 18 & 24 \end{smallmatrix}, 0.20\right)$

Table H.2: Parameters for the configurations and quark sources smearings. In all cases the Lüscher-Weisz gauge action has been used. The dynamical configuration are generated with $N_f = 2$ Chirally Improved fermions.

Spectral sums

for thin loops

β	$L^3 \times T$	a [fm]	T[MeV]	N_{conf}
7.00	$6^3 \times 4$	0.351	140	2000
7.60	$6^3 \times 4$	0.194	254	2000
7.91	$6^3 \times 4$	0.146	337	2000
7.00	$12^3 \times 4$	0.351	140	20
7.60	$12^3 \times 4$	0.194	254	20
7.91	$12^3 \times 4$	0.146	337	20
7.40	$12^3 \times 6$	0.234	140	20
8.06	$12^3 \times 6$	0.129	255	20
8.40	$12^3 \times 6$	0.098	337	20

Table H.3: Parameters and temperatures for the configurations, which we have used for the spectral sums to reconstruct the thin Polyakov loop. In all cases the Lüscher-Weisz gauge action has been used.

for dressed loops

$L^3 \times T$	β	a [fm]	T[MeV]	N_{conf}
$8^3 \times 4$	$7.10 - 8.20$	$0.316 - 0.115$	$156 - 430$	20
$10^3 \times 4$	7.91,8.23	0.146,0.112	337,441	20
$12^3 \times 4$	7.91,8.47	0.146,0.093	337,533	20
$14^3 \times 4$	7.91	0.146	337	20
$10^3 \times 6$	$7.60 - 8.67$	$0.194 - 0.080$	$170 - 413$	20
$12^3 \times 6$	$7.97 - 8.67$	$0.139 - 0.080$	$236 - 413$	20
$14^3 \times 6$	$7.97 - 8.67$	$0.139 - 0.080$	$236 - 413$	20
$14^3 \times 8$	8.67	0.080	1413	20

Table H.4: Parameters and temperatures for the configurations, which we have used for the spectral sums of the dressed Polyakov loop. In all cases the Lüscher-Weisz gauge action has been used.

Bibliography

[1] C. Gottbrath, J. Bailin, C. Meakin, T. Thompson, and J. J. Charfman, "The Effects of Moore's Law and Slacking on Large Computations," `arXiv:astro-ph/9912202`.

[2] I. Montvay and G. Münster, "Quantum fields on a lattice,". Cambridge, UK: Univ. Pr. (1994) 491 p. (Cambridge monographs on mathematical physics).

[3] T. DeGrand and C. E. Detar, "Lattice methods for quantum chromodynamics,". New Jersey, USA: World Scientific (2006) 345 p.

[4] H. J. Rothe, "Lattice gauge theories: An Introduction," *World Sci. Lect. Notes Phys.* **74** (2005) 1–605.

[5] C. Gattringer and C. B. Lang. To be published.

[6] K. G. Wilson, "Quarks and Strings on a Lattice,". New Phenomena In Subnuclear Physics. Part A. Proceedings of the First Half of the 1975 International School of Subnuclear Physics, Erice, Sicily, July 11 - August 1, 1975, ed. A. Zichichi, Plenum Press, New York, 1977, p. 69, CLNS-321.

[7] K. G. Wilson, "Confinement of quarks," *Phys. Rev.* **D10** (1974) 2445–2459.

[8] Y. Iwasaki, "Renormalization Group Analysis of Lattice Theories and Improved Lattice Action: Two-Dimensional Nonlinear O(N) Sigma Model," *Nucl. Phys.* **B258** (1985) 141–156.

[9] M. Lüscher and P. Weisz, "On-Shell Improved Lattice Gauge Theories," *Commun. Math. Phys.* **97** (1985) 59.

[10] H. B. Nielsen and M. Ninomiya, "Absence of Neutrinos on a Lattice. 1. Proof by Homotopy Theory," *Nucl. Phys.* **B185** (1981) 20.

[11] P. H. Ginsparg and K. G. Wilson, "A Remnant of Chiral Symmetry on the Lattice," *Phys. Rev.* **D25** (1982) 2649.

[12] R. Narayanan and H. Neuberger, "Chiral fermions on the lattice," *Phys. Rev. Lett.* **71** (1993) 3251–3254, arXiv:hep-lat/9308011.

[13] R. Narayanan and H. Neuberger, "A Construction of lattice chiral gauge theories," *Nucl. Phys.* **B443** (1995) 305–385, arXiv:hep-th/9411108.

[14] D. B. Kaplan, "A Method for simulating chiral fermions on the lattice," *Phys. Lett.* **B288** (1992) 342–347, arXiv:hep-lat/9206013.

[15] Y. Shamir, "Chiral fermions from lattice boundaries," *Nucl. Phys.* **B406** (1993) 90–106, arXiv:hep-lat/9303005.

[16] P. Hasenfratz, "Prospects for perfect actions," *Nucl. Phys. Proc. Suppl.* **63** (1998) 53–58, arXiv:hep-lat/9709110.

[17] P. Hasenfratz, S. Hauswirth, T. Jorg, F. Niedermayer, and K. Holland, "Testing the fixed-point QCD action and the construction of chiral currents," *Nucl. Phys.* **B643** (2002) 280–320, arXiv:hep-lat/0205010.

[18] C. Gattringer, "A new approach to Ginsparg-Wilson fermions," *Phys. Rev.* **D63** (2001) 114501, arXiv:hep-lat/0003005.

[19] C. Gattringer, I. Hip, and C. B. Lang, "Approximate Ginsparg-Wilson fermions: A first test," *Nucl. Phys.* **B597** (2001) 451–474, arXiv:hep-lat/0007042.

[20] L. H. Ryder, "Quantum field theory,". Cambridge, Uk: Univ. Pr. (1985) 443p.

[21] M. E. Peskin and D. V. Schroeder, "An Introduction to quantum field theory,". Reading, USA: Addison-Wesley (1995) 842 p.

[22] J. Gasser and H. Leutwyler, "Chiral Perturbation Theory to One Loop," *Ann. Phys.* **158** (1984) 142.

[23] J. Gasser and H. Leutwyler, "Chiral Perturbation Theory: Expansions in the Mass of the Strange Quark," *Nucl. Phys.* **B250** (1985) 465.

[24] H. J. Rothe and N. Sadooghi, "A new look at the axial anomaly in lattice QED with Wilson fermions," *Phys. Rev.* **D58** (1998) 074502, arXiv:hep-lat/9803026.

[25] J. B. Kogut and L. Susskind, "Vacuum Polarization and the Absence of Free Quarks in Four-Dimensions," *Phys. Rev.* **D9** (1974) 3501–3512.

[26] J. B. Kogut and L. Susskind, "Hamiltonian Formulation of Wilson's Lattice Gauge Theories," *Phys. Rev.* **D11** (1975) 395.

[27] A. S. Kronfeld, "Lattice gauge theory with staggered fermions: how, where, and why (not)," *PoS* **LATTICE2007** (2006) 016, arXiv:0711.0699 [hep-lat].

[28] M. Creutz, "Why rooting fails," *PoS* **LATTICE2007** (2006) 007, arXiv:0708.1295 [hep-lat].

[29] **MILC** Collaboration, K. Orginos and D. Toussaint, "Testing improved actions for dynamical Kogut-Susskind quarks," *Phys. Rev.* **D59** (1999) 014501, arXiv:hep-lat/9805009.

[30] G. P. Lepage, "Flavor-symmetry restoration and Symanzik improvement for staggered quarks," *Phys. Rev.* **D59** (1999) 074502, arXiv:hep-lat/9809157.

[31] **MILC** Collaboration, K. Orginos, D. Toussaint, and R. L. Sugar, "Variants of fattening and flavor symmetry restoration," *Phys. Rev.* **D60** (1999) 054503, arXiv:hep-lat/9903032.

[32] B. Sheikholeslami and R. Wohlert, "Improved Continuum Limit Lattice Action for QCD with Wilson Fermions," *Nucl. Phys.* **B259** (1985) 572.

[33] M. Bochicchio, L. Maiani, G. Martinelli, G. C. Rossi, and M. Testa, "Chiral Symmetry on the Lattice with Wilson Fermions," *Nucl. Phys.* **B262** (1985) 331.

[34] K. Symanzik, "Schrödinger Representation and Casimir Effect in Renormalizable Quantum Field Theory," *Nucl. Phys.* **B190** (1981) 1.

[35] M. Lüscher, "Schrödinger representation in quantum field theory," *Nucl. Phys.* **B254** (1985) 52–57.

[36] M. Lüscher, R. Sommer, P. Weisz, and U. Wolff, "A Precise determination of the running coupling in the SU(3) Yang-Mills theory," *Nucl. Phys.* **B413** (1994) 481–502, arXiv:hep-lat/9309005.

[37] S. Sint, "On the Schrödinger functional in QCD," *Nucl. Phys.* **B421** (1994) 135–158, arXiv:hep-lat/9312079.

[38] R. Sommer, "Non-perturbative QCD: Renormalization, O(a)-improvement and matching to heavy quark effective theory," arXiv:hep-lat/0611020.

[39] F. J. Wegner, "Duality in Generalized Ising Models and Phase Transitions Without Local Order Parameters," *J. Math. Phys.* **12** (1971) 2259–2272.

[40] K. Symanzik, "Continuum Limit and Improved Action in Lattice Theories. 1. Principles and ϕ^4 Theory," *Nucl. Phys.* **B226** (1983) 187.

[41] K. Symanzik, "Continuum Limit and Improved Action in Lattice Theories. 2. O(N) Nonlinear Sigma Model in Perturbation Theory," *Nucl. Phys.* **B226** (1983) 205.

[42] G. Curci, P. Menotti, and G. Paffuti, "Symanzik's improved lagrangian for lattice gauge theory," *Phys. Lett.* **B130** (1983) 205.

[43] G. P. Lepage and P. B. Mackenzie, "On the viability of lattice perturbation theory," *Phys. Rev.* **D48** (1993) 2250–2264, arXiv:hep-lat/9209022.

[44] M. G. Alford, W. Dimm, G. P. Lepage, G. Hockney, and P. B. Mackenzie, "Lattice QCD on small computers," *Phys. Lett.* **B361** (1995) 87–94, arXiv:hep-lat/9507010.

[45] M. Lüscher, "Exact chiral symmetry on the lattice and the Ginsparg-Wilson relation," *Phys. Lett.* **B428** (1998) 342–345, arXiv:hep-lat/9802011.

[46] H. Neuberger, "Exactly massless quarks on the lattice," *Phys. Lett.* **B417** (1998) 141–144, arXiv:hep-lat/9707022.

[47] H. Neuberger, "More about exactly massless quarks on the lattice," *Phys. Lett.* **B427** (1998) 353–355, arXiv:hep-lat/9801031.

[48] J. Bloch, A. Frommer, B. Lang, and T. Wettig, "An iterative method to compute the sign function of a non- Hermitian matrix and its application to the overlap Dirac operator at nonzero chemical potential," *Comput. Phys. Commun.* **177** (2007) 933–943, arXiv:0704.3486 [hep-lat].

[49] R. G. Edwards, B. Joo, A. D. Kennedy, K. Orginos, and U. Wenger, "Comparison of chiral fermion methods," *PoS* **LAT2005** (2006) 146, arXiv:hep-lat/0510086.

[50] J. van den Eshof, A. Frommer, T. Lippert, K. Schilling, and H. A. van der Vorst, "Numerical methods for the QCD overlap operator. I: Sign-function and error bounds," *Comput. Phys. Commun.* **146** (2002) 203–224, arXiv:hep-lat/0202025.

[51] G. Arnold *et al.*, "Numerical methods for the QCD overlap operator. II: Optimal Krylov subspace methods," arXiv:hep-lat/0311025.

[52] N. Cundy *et al.*, "Numerical methods for the QCD overlap operator. III: Nested iterations," *Comput. Phys. Commun.* **165** (2005) 221–242, arXiv:hep-lat/0405003.

[53] N. Cundy *et al.*, "Numerical methods for the QCD overlap operator. IV: Hybrid Monte Carlo," arXiv:hep-lat/0502007.

[54] F. Belletti *et al.*, "QCD on the Cell Broadband Engine," *PoS* **LATTICE2007** (2006) 039, arXiv:0710.2442 [hep-lat].

[55] T. Maurer, "Moments of unpolarized nucleon structure functions in chirally improved lattice quantum chromodynamics," Master's thesis, 2007.

[56] S. Duane, A. D. Kennedy, B. J. Pendleton, and D. Roweth, "Hybrid Monte Carlo," *Phys. Lett.* **B195** (1987) 216–222.

[57] A. D. Kennedy, "Algorithms for dynamical fermions," arXiv:hep-lat/0607038.

[58] A. D. Kennedy and M. A. Clark, "Speeding up HMC with better integrators," *PoS* **LAT2007** (2007) 038, arXiv:0710.3611 [hep-lat].

[59] M. Hasenbusch and K. Jansen, "Speeding up lattice QCD simulations with clover-improved Wilson fermions," *Nucl. Phys.* **B659** (2003) 299–320, arXiv:hep-lat/0211042.

[60] J. C. Sexton and D. H. Weingarten, "Hamiltonian evolution for the hybrid Monte Carlo algorithm," *Nucl. Phys.* **B380** (1992) 665–678.

[61] R. C. Brower, T. Ivanenko, A. R. Levi, and K. N. Orginos, "Chronological inversion method for the Dirac matrix in hybrid Monte Carlo," *Nucl. Phys.* **B484** (1997) 353–374, arXiv:hep-lat/9509012.

[62] R. Gupta, T. Bhattacharya, and G. Kilcup, "Comparison of inversion algorithms for Wilson fermions on the CM5," arXiv:hep-lat/9605029.

[63] B. Jegerlehner, "Krylov space solvers for shifted linear systems," arXiv:hep-lat/9612014.

[64] M. Asakawa, T. Hatsuda, and Y. Nakahara, "Maximum entropy analysis of the spectral functions in lattice QCD," *Prog. Part. Nucl. Phys.* **46** (2001) 459–508, arXiv:hep-lat/0011040.

[65] G. P. Lepage *et al.*, "Constrained curve fitting," *Nucl. Phys. Proc. Suppl.* **106** (2002) 12–20, arXiv:hep-lat/0110175.

[66] Y. Chen *et al.*, "The Sequential Empirical Bayes Method: An adaptive constrained-curve fitting algorithm for lattice QCD," arXiv:hep-lat/0405001.

[67] G. T. Fleming, "What can lattice QCD theorists learn from NMR spectroscopists?," arXiv:hep-lat/0403023.

[68] G. M. von Hippel, R. Lewis, and R. G. Petry, "Using evolutionary algorithms to extract field theory mass spectra," *PoS* **LAT2007** (2007) 043, arXiv:0710.0014 [hep-lat].

[69] H.-W. Lin and S. D. Cohen, "Lattice QCD Beyond Ground States," arXiv:0709.1902 [hep-lat].

[70] C. Michael, "Adjoint Sources in Lattice Gauge Theory," *Nucl. Phys.* **B259** (1985) 58.

[71] M. Lüscher and U. Wolff, "How to calculate the elastic scattering matrix in two- dimensional quantum field theories by numerical simulation," *Nucl. Phys.* **B339** (1990) 222–252.

[72] T. Burch, C. Gattringer, L. Y. Glozman, C. Hagen, and C. B. Lang, "Variational method for lattice spectroscopy with ghosts," *Phys. Rev.* **D73** (2006) 017502, arXiv:hep-lat/0511054.

[73] T. Burch, C. Hagen, M. Hetzenegger, and A. Schäfer. To be published.

[74] C. Gattringer, L. Y. Glozman, C. B. Lang, D. Mohler, and S. Prelovsek, "Derivative sources in lattice spectroscopy of excited mesons," arXiv:0802.2020 [hep-lat].

[75] S. Sasaki, T. Blum, and S. Ohta, "A lattice study of the nucleon excited states with domain wall fermions," *Phys. Rev.* **D65** (2002) 074503, arXiv:hep-lat/0102010.

[76] **Bern-Graz-Regensburg** Collaboration, D. Brommel *et al.*, "Excited nucleons with chirally improved fermions," *Phys. Rev.* **D69** (2004) 094513, arXiv:hep-ph/0307073.

[77] **Bern-Graz-Regensburg** Collaboration, T. Burch *et al.*, "Excited hadrons on the lattice: Mesons," *Phys. Rev.* **D73** (2006) 094505, arXiv:hep-lat/0601026.

[78] **Bern-Graz-Regensburg** Collaboration, T. Burch *et al.*, "Excited hadrons on the lattice: Baryons," *Phys. Rev.* **D74** (2006) 014504, arXiv:hep-lat/0604019.

[79] S. Gusken *et al.*, "Nonsinglet axial vector couplings of the baryon octet in lattice QCD," *Phys. Lett.* **B227** (1989) 266.

[80] C. Best *et al.*, "Pion and rho structure functions from lattice QCD," *Phys. Rev.* **D56** (1997) 2743–2754, arXiv:hep-lat/9703014.

[81] X. Liao and T. Manke, "Excited charmonium spectrum from anisotropic lattices," arXiv:hep-lat/0210030.

[82] **CP-PACS** Collaboration, S. Aoki *et al.*, "Comparative study of full QCD hadron spectrum and static quark potential with improved actions," *Phys. Rev.* **D60** (1999) 114508, arXiv:hep-lat/9902018.

[83] **CP-PACS** Collaboration, A. Ali Khan *et al.*, "Light hadron spectroscopy with two flavors of dynamical quarks on the lattice," *Phys. Rev.* **D65** (2002) 054505, arXiv:hep-lat/0105015.

[84] **SciDAC** Collaboration, R. G. Edwards and B. Joo, "The Chroma software system for lattice QCD," *Nucl. Phys. Proc. Suppl.* **140** (2005) 832, arXiv:hep-lat/0409003.

[85] **QCDOC** Collaboration, P. A. Boyle, C. Jung, and T. Wettig, "The QCDOC supercomputer: Hardware, software, and performance," *ECONF* **C0303241** (2003) THIT003, arXiv:hep-lat/0306023.

[86] **UKQCD** Collaboration, C. R. Allton *et al.*, "Gauge invariant smearing and matrix correlators using Wilson fermions at Beta = 6.2," *Phys. Rev.* **D47** (1993) 5128–5137, arXiv:hep-lat/9303009.

[87] **Particle Data Group** Collaboration, W. M. Yao *et al.*, "Review of particle physics," *J. Phys.* **G33** (2006) 1–1232.

[88] R. Frigori *et al.*, "Dynamical Chirally Improved Quarks: First Results for Hadron Masses," *PoS* **LAT2007** (2007) 114, arXiv:0709.4582 [hep-lat].

[89] A. Duncan and E. Eichten, "Improved pseudofermion approach for all-point propagators," *Phys. Rev.* **D65** (2002) 114502, arXiv:hep-lat/0112028.

[90] H. Neff, N. Eicker, T. Lippert, J. W. Negele, and K. Schilling, "On the low fermionic eigenmode dominance in QCD on the lattice," *Phys. Rev.* **D64** (2001) 114509, arXiv:hep-lat/0106016.

[91] J. Foley *et al.*, "Practical all-to-all propagators for lattice QCD," *Comput. Phys. Commun.* **172** (2005) 145–162, arXiv:hep-lat/0505023.

[92] **SESAM** Collaboration, G. S. Bali, H. Neff, T. Duessel, T. Lippert, and K. Schilling, "Observation of string breaking in QCD," *Phys. Rev.* **D71** (2005) 114513, arXiv:hep-lat/0505012.

[93] **UKQCD** Collaboration, C. Michael and J. Peisa, "Maximal variance reduction for stochastic propagators with applications to the static quark spectrum," *Phys. Rev.* **D58** (1998) 034506, arXiv:hep-lat/9802015.

[94] T. A. DeGrand, "A conditioning technique for matrix inversion for Wilson fermions," *Comput. Phys. Commun.* **52** (1988) 161–164.

[95] M. Lüscher, "Schwarz-preconditioned HMC algorithm for two-flavour lattice QCD," *Comput. Phys. Commun.* **165** (2005) 199–220, arXiv:hep-lat/0409106.

[96] T. Burch and C. Hagen, "Domain decomposition improvement of quark propagator estimation," *Comput. Phys. Commun.* **176** (2007) 137–145, arXiv:hep-lat/0607029.

[97] T. Burch *et al.*, "B meson excitations with chirally improved light quarks," *PoS* **LAT2007** (2007) 091, arXiv:0709.3708 [hep-lat].

[98] R. G. Edwards, U. M. Heller, and R. Narayanan, "A study of chiral symmetry in quenched QCD using the overlap-Dirac operator," *Phys. Rev.* **D59** (1999) 094510, arXiv:hep-lat/9811030.

[99] **UKQCD** Collaboration, C. McNeile and C. Michael, "Mixing of scalar glueballs and flavour-singlet scalar mesons," *Phys. Rev.* **D63** (2001) 114503, arXiv:hep-lat/0010019.

[100] **MILC** Collaboration, T. A. DeGrand and U. M. Heller, "Witten-Veneziano relation, quenched QCD, and overlap fermions," *Phys. Rev.* **D65** (2002) 114501, arXiv:hep-lat/0202001.

[101] A. V. Manohar and M. B. Wise, "Heavy quark physics," *Camb. Monogr. Part. Phys. Nucl. Phys. Cosmol.* **10** (2000) 1–191.

[102] D. Brömmel, "Pion structure from the lattice,". DESY-THESIS-2007-023.

[103] S. Schaefer, *Chiral symmetry and hadronic measurements on the lattice.* PhD thesis, 2003.

[104] A. Hasenfratz and F. Knechtli, "Flavor symmetry and the static potential with hypercubic blocking," *Phys. Rev.* **D64** (2001) 034504, arXiv:hep-lat/0103029.

[105] C. Morningstar and M. J. Peardon, "Analytic smearing of SU(3) link variables in lattice QCD," *Phys. Rev.* **D69** (2004) 054501, arXiv:hep-lat/0311018.

[106] **D0** Collaboration, V. M. Abazov *et al.*, "Observation and Properties of $L = 1 B_1$ and B_2^* Mesons," *Phys. Rev. Lett.* **99** (2007) 172001, arXiv:0705.3229 [hep-ex].

[107] **CDF** Collaboration, T. Aaltonen *et al.*, "Observation of Orbitally Excited B_s Mesons," *Phys. Rev. Lett.* **100** (2008) 082001, arXiv:0710.4199 [hep-ex].

[108] **D0** Collaboration, V. M. Abazov *et al.*, "Observation and properties of the orbitally excited B_{s2}^* Meson," *Phys. Rev. Lett.* **100** (2008) 082002, arXiv:0711.0319 [hep-ex].

[109] **CDF** Collaboration, T. Aaltonen *et al.*, "First observation of heavy baryons Σ_b and Σ_b^*," *Phys. Rev. Lett.* **99** (2007) 202001, arXiv:0706.3868 [hep-ex].

[110] **CDF** Collaboration, T. Aaltonen *et al.*, "Observation and mass measurement of the baryon Xi_b^-," *Phys. Rev. Lett.* **99** (2007) 052002, arXiv:0707.0589 [hep-ex].

[111] **D0** Collaboration, V. M. Abazov *et al.*, "Direct observation of the strange b baryon Xi_b^-," *Phys. Rev. Lett.* **99** (2007) 052001, arXiv:0706.1690 [hep-ex].

[112] J. Koponen, "P- and D-wave spin-orbit splittings in heavy-light mesons," *PoS* **LAT2007** (2007) 112, arXiv:0710.0489 [hep-lat].

[113] J. Foley, A. O'Cais, M. Peardon, and S. M. Ryan, "Radial and orbital excitations of static-light mesons," *Phys. Rev.* **D75** (2007) 094503, arXiv:hep-lat/0702010.

[114] **UKQCD** Collaboration, K. C. Bowler *et al.*, "Heavy Baryon Specroscopy from the Lattice," *Phys. Rev.* **D54** (1996) 3619–3633, arXiv:hep-lat/9601022.

[115] N. Mathur, R. Lewis, and R. M. Woloshyn, "Charmed and bottom baryons from lattice NRQCD," *Phys. Rev.* **D66** (2002) 014502, arXiv:hep-ph/0203253.

[116] H. Na and S. A. Gottlieb, "Charm and bottom heavy baryon mass spectrum from lattice QCD with 2+1," *PoS* **LATTICE** (2007) 124, arXiv:0710.1422 [hep-lat].

[117] T. Banks and A. Casher, "Chiral Symmetry Breaking in Confining Theories," *Nucl. Phys.* **B169** (1980) 103.

[118] C. Gattringer, P. E. L. Rakow, A. Schäfer, and W. Söldner, "Chiral symmetry restoration and the Z(3) sectors of QCD," *Phys. Rev.* **D66** (2002) 054502, arXiv:hep-lat/0202009.

[119] L. D. McLerran and B. Svetitsky, "Quark Liberation at High Temperature: A Monte Carlo Study of SU(2) Gauge Theory," *Phys. Rev.* **D24** (1981) 450.

[120] C. Gattringer, "Linking confinement to spectral properties of the Dirac operator," *Phys. Rev. Lett.* **97** (2006) 032003, arXiv:hep-lat/0605018.

[121] F. Bruckmann, C. Gattringer, and C. Hagen, "Complete spectra of the Dirac operator and their relation to confinement," *Phys. Lett.* **B647** (2007) 56–61, arXiv:hep-lat/0612020.

[122] C. Hagen, F. Bruckmann, E. Bilgici, and C. Gattringer, "Thin and dressed Polyakov loops from spectral sums of lattice differential operators," *PoS* **LATTICE** (2007) 289, arXiv:0710.0294 [hep-lat].

[123] W. Söldner, "The Polyakov Loop and the Eigenvalues of the Dirac Operator," *PoS* **LAT2007** (2007) 222, arXiv:0710.2707 [hep-lat].

[124] F. Synatschke, A. Wipf, and C. Wozar, "Spectral sums of the Dirac-Wilson operator and their relation to the Polyakov loop," *Phys. Rev.* **D75** (2007) 114003, arXiv:hep-lat/0703018.

[125] E. Bilgici, F. Bruckmann, C. Gattringer, and C. Hagen, "Dual quark condensate and dressed Polyakov loops," *Phys. Rev.* **D77** (2008) 094007, arXiv:0801.4051 [hep-lat].

[126] F. Synatschke, A. Wipf, and K. Langfeld, "Relation between chiral symmetry breaking and confinement in YM-theories," arXiv:0803.0271 [hep-lat].

[127] E. Bilgici and C. Gattringer, "Static quark-antiquark potential and Dirac eigenvector correlators," arXiv:0803.1127 [hep-lat].

[128] C. Gattringer, R. Hoffmann, and S. Schäefer, "Setting the scale for the Luescher-Weisz action," *Phys. Rev.* **D65** (2002) 094503, arXiv:hep-lat/0112024.

[129] C. Gattringer and S. Schaefer, "New findings for topological excitations in SU(3) lattice gauge theory," *Nucl. Phys.* **B654** (2003) 30–60, arXiv:hep-lat/0212029.

[130] **UKQCD** Collaboration, M. Foster and C. Michael, "Hadrons with a heavy colour-adjoint particle," *Phys. Rev.* **D59** (1999) 094509, arXiv:hep-lat/9811010.

[131] J. Zinn-Justin, "Quantum field theory and critical phenomena," *Int. Ser. Monogr. Phys.* **113** (2002) 1–1054.

Acknowledgments

It is a great pleasure for me to thank all the people who contributed to the success of this thesis.

First of all my adviser Prof. Dr. Andreas Schäfer, who has provided an enjoyable and stimulating environment, by fostering such a large group, with people working basically in all subjects of lattice QCD. His helpful comments and suggestions have been an indispensable contribution to this thesis.

I would like to thank my collaborators, especially Dr. Falk Bruckmann, Dr. Tommy Burch, and Prof. Dr. Christof Gattringer for patiently answering innumerable questions. I also want to thank all the members of the Bern-Graz-Regensburg collaboration, especially Prof. Dr. Christian B. Lang and Markus Limmer for generating the dynamical gauge configurations.

Further thanks go to my colleagues, especially to Christian Ehmann, Dieter Hierl, Thilo Maurer, Stefan Solbrig, and Nikolaus Warkentin for interesting and helpful discussions.

Additional thanks to the CP-PACS collaboration for making their configurations public available.

Lattice QCD cannot be done without extensive computer resources. Therefore, I'm grateful for the opportunity to use the QCDOC in Regensburg as well as the cluster at the Leibniz Rechenzentrum in Munich. Special thanks go to Stefan Solbrig for keeping the QCDOC running and to the staff of the LRZ for their technical support.

Many thanks also go to the secretaries of our institute, Monika Maschek and Heidi Decock.

I also thank GSI and BMBF for financial support during the last years.

Finally, I want to thank my family, especially my parents, for supporting me all the years.